Chapter 5
KAW Turbulence in Solar Wind

5.1 Solar Wind: Natural Laboratory for Plasma Turbulence

Plasma turbulence is a stochastic state of the plasma and its electromagnetic fluctuations in spatial and temporal structures. Unlike the randomness of thermal fluctuations (or i.e., thermal noise) that is caused by the discrete randomness of microscopic particles (or i.e., the hypothesis of molecular chaos), however, the turbulent stochasticity of the plasma turbulence should be attributed to the chaotic nondeterminacy of plasma collective modes when dynamically evolving into the chaos state via their nonlinear coupling (Ruelle and Takens 1971; Gollub and Swinney 1975). Plasmas, consisting of charged particles, are intrinsically different from neutral fluids, consisting of neutral atoms or molecules, and can have a number of various collective eigenmodes due to the interparticle electromagnetic interaction. The nonlinear coupling between these collective modes not only is the most distinctive and essential characteristic of the plasma dynamics but also can make the plasma more easily develop into a turbulent state. Therefore, plasma turbulence is ubiquitous phenomena and may play important and crucial roles in various plasma processes such as plasma diffusion and transport, plasma acceleration and heating, plasma intermittent structures and energy dissipation.

The solar wind continuously expands from the solar outmost atmosphere (i.e., the solar corona) into the interplanetary space in the form of supersonic and super-Alfvénic plasma flows and directly impacts on the earth's magnetosphere. Observations and theory both show that as its high-Mach expands the solar wind has developed into a strongly turbulent state filled by large-amplitude electromagnetic fluctuations from low frequencies much less than the ion gyrofrequency to high frequencies near the electron Langmuir frequency in the interplanetary space. Therefore, the solar wind not only plays an important linking and transport role in the solar-terrestrial coupling system, but also is a natural laboratory for studying plasma turbulence (Tu and Marsch 1995; Bruno and Carbone 2013).

D.-J. Wu and L. Chen, *Kinetic Alfvén Waves in Laboratory, Space, and Astrophysical Plasmas*, Atmosphere, Earth, Ocean & Space,
https://doi.org/10.1007/978-981-13-7989-5_5

The study of ordinary fluid turbulence can be traced back to the experimental investigation by Osborne (1883) more than one century ago, who observed and investigated experimentally the transition from laminar to turbulent flow inside a pipe and found that this transition depends on a single parameter,

$$R_e = \frac{UL}{\nu}, \tag{5.1}$$

now called the Reynolds number, where U is the characteristic flow velocity, L is the characteristic length scale of the velocity field $\mathbf{u}(\mathbf{r}, t)$, and ν is the viscosity coefficient. The Reynolds number R_e, in fact, represents the relative strength between the non-linear convection term, $(\mathbf{u} \cdot \nabla)\mathbf{u}$, and the viscosity term, $\nu\nabla^2\mathbf{u}$, in the Navier-Stokes equation:

$$\partial_t \mathbf{u} + (\mathbf{u} \cdot \nabla)\,\mathbf{u} = -\rho^{-1}\nabla p + \nu\nabla^2\mathbf{u}, \tag{5.2}$$

where the incompressible condition of $\nabla \cdot \mathbf{u} = 0$ has been used for the sake of simplicity and ρ and p are the mass density and the kinetic pressure of the fluid, respectively. A larger Reynolds number represents stronger nonlinearity and the turbulent flow usually occurs in the case of high Reynolds numbers, in which the non-linear term dominates the dynamical behavior of the flow.

For the incompressible MHD case of a conducting fluid in a magnetic field, the Navier-Stokes equations may be reduced to

$$\begin{aligned} \partial_t \mathbf{u} + (\mathbf{u} \cdot \nabla)\,\mathbf{u} &= \left(\mathbf{b}' \cdot \nabla\right)\mathbf{b}' - \rho^{-1}\nabla p_t + \nu\nabla^2\mathbf{u} \\ \partial_t \mathbf{b}' + (\mathbf{u} \cdot \nabla)\,\mathbf{b}' &= \left(\mathbf{b}' \cdot \nabla\right)\mathbf{u} + \nu_m\nabla^2\mathbf{b}', \end{aligned} \tag{5.3}$$

where $p_t \equiv p + B^2/2\mu_0$ is the total pressure, $\mathbf{b}' \equiv \mathbf{B}/\sqrt{\mu_0\rho} = \mathbf{v}_A + \mathbf{b}$ the total magnetic field in the velocity form, $\mathbf{v}_A = \mathbf{B}_0/\sqrt{\mu_0\rho}$ the Alfvén velocity, $\mathbf{B}_0 = B_0\hat{z}$ the uniform ambient magnetic field, $\mathbf{b} \equiv (\mathbf{B} - \mathbf{B}_0)/\sqrt{\mu_0\rho}$ is the fluctuation magnetic field in the velocity form, $\nu_m \equiv 1/\sigma\mu_0$ the magnetic viscosity coefficient, and σ the conductivity. Similar to the Reynolds number R_e, a magnetic Reynolds number that represents the relative strength of the nonlinear convection of the conducting fluid, R_m, can be defined as follows:

$$R_m = \frac{UL}{\nu_m} \sim \frac{v_A L}{\nu_m}, \tag{5.4}$$

In the solar wind, the magnetic Reynolds number can be very large as $R_m > 10^{10}$, implying that the turbulence can be ubiquitous states of solar wind plasma flows.

From the MHD equation (5.3), the plasma flow $\mathbf{u}$ and the magnetic field $\mathbf{b}$ are coupled together each other through the Lorentz force. Introducing the so-called Elsässer variables:

$$\mathbf{z}^{\pm} \equiv \mathbf{u} \pm \mathbf{b}, \tag{5.5}$$

the MHD equation (5.3) can be rewritten as symmetrized form as follows:

$$\left(\partial_t \mp \mathbf{v}_A \cdot \nabla + \mathbf{z}^{\mp} \cdot \nabla\right) \mathbf{z}^{\pm} = -\rho^{-1} \nabla p_t + \nu^{\pm} \nabla^2 \mathbf{z}^{\pm} + \nu^{\mp} \nabla^2 \mathbf{z}^{\mp}, \tag{5.6}$$

where $2\nu^{\pm} = \nu \pm \nu_m$. The total pressure p_t can be determined by the condition $\nabla \cdot \mathbf{z}^{\pm} = 0$, or given by the solution of the following equation

$$\nabla^2 p_t = -\nabla\nabla \cdot \cdot \mathbf{z}^{+}\mathbf{z}^{-}. \tag{5.7}$$

Neglecting the viscous term, the linearization of Eq. (5.6) leads to

$$\left(\partial_t \mp \mathbf{v}_A \cdot \nabla\right) \mathbf{z}^{\pm} = 0, \tag{5.8}$$

which general solutions with the "traveling wave" form, $\mathbf{z}^{\mp}(\mathbf{r} \mp \mathbf{v}_A t)$, describe Alfvénic fluctuations propagating parallel ("−") and antiparallel ("+") to the uniform ambient magnetic field $\mathbf{B}_0$, respectively.

Although the experimental investigation of turbulence had started more than one century ago, so far the most important achievement is still the legacy of A. N. Kolmogorov based on some phenomenological considerations and simple dimensional analysis, that is, so-called the Kolmogorov inertial spectrum of turbulence driven by the nonlinear energy cascade. According to the scenario proposed by Kolmogorov (1941), the structurized energy at the injection scale L is transferred by nonlinear interactions, throughout a string of intermediate scales λ, to the small dissipation scale $l_D \ll \lambda \ll L$, and eventually is dissipated at this dissipation scale l_D. According to the first similarity hypothesis by Kolmogorov (1941), the whole dynamical process from the energy injection at the large scale L to the energy dissipation at the small dissipation scale l_D is controlled mainly by the two parameters: (1) the energy transferring rate $\varepsilon_{T\lambda} \sim u_\lambda^2/\tau_{T\lambda} \sim u_\lambda^3/\lambda$ and (2) the energy dissipation rate $\varepsilon_{D\lambda} \sim u_\lambda^2/\tau_{D\lambda} \sim u_\lambda^2 \nu/\lambda^2$ (or by their ratio, that is, the local Reynolds number $R_{e\lambda} = \varepsilon_{T\lambda}/\varepsilon_{D\lambda} = u_\lambda \lambda/\nu$), where $\tau_{T\lambda} \sim \lambda/u_\lambda$ and $\tau_{D\lambda} \sim \lambda^2/\nu$ are the characteristic transferring and dissipation times at the scale λ, respectively. The two parameters $\varepsilon_{T\lambda}$ and $\varepsilon_{D\lambda}$ represent the relative strengths of the nonlinear convection and the viscosity, respectively, and in general, both are dependent on the scale λ. In particular, in the large injection scale L one has $\varepsilon_{TL}/\varepsilon_{DL} = UL/\nu = R_e \gg 1$, implying that in the case of large Reynolds numbers, the fluid is unable to dissipate the whole injection energy at the scale L and the excess energy must be transferred to smaller scales $\lambda < L$ until it is dissipated entirely at the dissipation scale $\lambda \sim l_D \ll L$. This is the physical reason for the energy turbulent cascade toward small scales.

For a steady case, the energy injection rate $\varepsilon_{TL} \sim U^3/L$ at the large injection scale L must be balanced by the energy dissipation rate $\varepsilon_{Dl_D} \sim u_{l_D}^2 \nu/l_D^2$ at the small dissipation scale l_D, that is,

$$\varepsilon_{TL} \sim \varepsilon_{Dl_D} \Rightarrow \frac{l_D^2}{L^2} \sim \frac{1}{R_e} \frac{u_{l_D}^2}{U^2}. \tag{5.9}$$

In particular, in order to avoid the energy piled up at some scales λ, it is a plausible hypothesis, that is, that second similarity hypothesis by Kolmogorov (1941), that the energy transferring rate $\varepsilon_{T\lambda}$ is independent from the scale λ in the so-called inertial scale region of $L \gg \lambda \gg l_D$ where the viscosity has a negligible smallness (i.e., the infinite Reynolds number approximation), that is, one has

$$\varepsilon_{T\lambda} = u_\lambda^3/\lambda = \text{constant} \Rightarrow u_\lambda \sim \varepsilon_T^{1/3}\lambda^{1/3}, \tag{5.10}$$

where ε_T is the constant energy transferring rate. Thus, from Eq. (5.9) the effective dissipation scale l_D can be estimated as

$$\frac{l_D}{L} \sim R_e^{-1/2}\frac{u_{l_D}}{U} \sim R_e^{-1/2}\left(\frac{l_D}{L}\right)^{1/3} \Rightarrow l_D \sim R_e^{-3/4}L, \tag{5.11}$$

which depends on the Reynolds number R_e as well as the energy injection scale L and is much less than the injection scale L in the case of high Reynolds numbers.

In the case of high Reynolds numbers $R_e \gg 1$ there can be a very wide inertial region of structurized scales λ (i.e., $L \gg \lambda \gg l_D \sim R_e^{-3/4}L$) in which the flow motions u_λ at almost all scales λ from L to l_D are excited by the nonlinear convection interaction through driving the large-scale structurized energy (U^2) to be fragmented into small-scale structurized energy (u_λ^2) at smaller and smaller scales $\lambda \ll L$ until approaching the effective dissipation scale l_D. In this inertial region, based on the requirement of the constant energy transferring rate ε_T, the energy of fragmented structures at the scale λ, u_λ^2, may be estimated by

$$u_\lambda^2 \sim \varepsilon_T^{2/3}\lambda^{2/3} \Rightarrow u_k^2 \sim \varepsilon_T^{2/3}k^{-2/3}, \tag{5.12}$$

where $k \sim 1/\lambda$ represents the wave number at the fragmented scale λ. Introducing the spectral energy density E_k in the wave number k space, one has

$$\delta u_k^2 = E_k \delta k \Rightarrow E_k \sim \partial_k u_k^2 \sim \varepsilon_T^{2/3}k^{-5/3}. \tag{5.13}$$

This inertial-scale spectrum E_k is the famous Kolmogorov spectrum and the fragmented process of the large-scale structurized energy toward the small-scale structurized energy also is called the nonlinear energy cascade process or the turbulent cascade process, which is driven possibly by nonlinear interactions. However, the physical mechanism of the nonlinear interactions that leads to the energy cascade toward small-scale structures is still unclear.

Based on the theory of classical nonlinear dynamical systems originated by Poincaré at the end of the 19th century, the early studies on the laminar-turbulent transition mechanism were modeled by a sequence of Hopf bifurcations. The first transition scenario was proposed by Landau (1944), in which as the Reynolds number increases the transition is attributed to a infinite series of Hopf bifurcations and each subsequent bifurcation adds a new incommensurate frequency to the flow motions,

in consequence, the quasi-periodic motions involving the infinite number of degree of freedom resemble the state of a turbulent flow (Hopf 1948). However, this Landau scenario is very difficult to be realized because the incommensurate frequencies cannot exist without coupling between them (Smale 1967).

Ruelle and Takens (1971) described another scenario of the birth to turbulence, in which after a few, usually three, Hopf bifurcations the flow becomes suddenly chaotic state characterized by a very intricate attracting subset, called a strange attractor. The flow in the chaotic state appears a highly irregular and very complicated topological structure, and its trajectories in phase space look to be unpredictable because the extremely strong dependence of their behavior on initial conditions leads to the exponential divergence of neighboring trajectories. This chaotic feature also is called the "butterfly effect" and represents the deterministic chaos. A few years later, the experimental measurements by Gollub and Swinney (1975) further confirmed that the transition to turbulence in a flow between co-rotating cylinders does not agree with the scenario proposed by Landau (1944), but is more consistent with that described by Ruelle and Takens (1971).

In the Ruelle-Takens scenario, however, the formation of wide continuous spectra of turbulence is still an open problem. The complexity and difficulty of the turbulence study both are beyond imagination, as implied by its name "turbulence". Up to now there are few basic principles that have been definitely established, exactly confirmed, and convincingly accepted in this community. As pointed out by Lumley and Yaglom (2001), "even after 100 years, turbulence studies are still their infancy".

In the case of plasma turbulence, the situation becomes more intricate because a lot of eigenmodes of plasma and electromagnetic field fluctuations can present simultaneously in the plasma, which have various and different dispersion relations and polarization states. For instance, multiple fields and species, different kinetic processes perpendicular and parallel to the local magnetic field, the coupling between various eigenmodes, and so on, all inevitably increase greatly the complexity of plasma turbulent cascade processes. In particular, the collisionless characteristic of major space and astrophysical plasmas leads to the classical scenario of the turbulence transition from the inertial to dissipative regimes, where the injected turbulent energy is converted eventually into the thermal energy of particles by collisional dissipation, no longer being valid. In collisionless plasma environments plasma turbulence with variously continuous spectra has been extensively observed (e.g., in the solar wind, Bale et al. 2005; Bruno and Carbone 2005; Sahraoui et al. 2009, 2010; He et al. 2012a; Salem et al. 2012; Podesta 2013; Goldstein et al. 2015). While the kinetic theory obviously is necessary to understand the physics of collisionless plasma turbulence.

In this chapter, our concerns focus on the kinetic scales of solar wind turbulent spectra, in particular, on the spectral transition from large MHD scales to small kinetic scales of particles, where KAWs can play an important and crucial role. After briefly introducing the anisotropic cascade of MHD turbulence from the MHD scales to the particle kinetic scales in Sects. 5.2 and 5.3 describes some basic concepts of the gyrokinetics, which is proper model for KAWs. Recent progresses of studies of KAW turbulence in the solar wind in theory and observation will be discussed in Sects. 5.4 and 5.5, respectively.

5.2 Anisotropic Cascade of AW Turbulence Towards Small Scales

5.2.1 Iroshnikov-Kraichnan Theory of AW Turbulence

Iroshnikov (1963) and Kraichnan (1965) earliest realized that the presence of a magnetic field could significantly influence the turbulence of a conducting fluid, in which the fluctuations of flow and magnetic field, $\mathbf{u}_\lambda$ and $\mathbf{b}_\lambda$ at the scale λ can be related each other via the Lorentz force $\mathbf{j} \times \mathbf{b}$ and the related fluctuations propagate in the form of the eigenmode (i.e., AWs) at the Alfvén velocity v_A along the ambient magnetic field $\mathbf{B}_0$. From the reduced MHD equation (5.6), the nonlinear interaction between the fluctuations $\mathbf{z}^\pm$ is included in the term $\mathbf{z}^\mp \cdot \nabla \mathbf{z}^\pm$, which describes the interaction of the head-on "collision" between opposite propagating fluctuations $\mathbf{z}^+$ and $\mathbf{z}^-$. Similar to the case of ordinary fluids, the energy transferring rate can be estimated by $\varepsilon_{T\lambda} \sim u_\lambda^2/\tau_{T\lambda}$. Unlike the case of ordinary fluids, however, the characteristic time of the head-on interaction $\tau_{T\lambda}$ is no longer simple flow turnover time $\sim\lambda/u_\lambda$, rather is lengthened by a factor $\sqrt{N}$ because of the stochastic nature of the collision process in which $N \sim v_A^2/u_\lambda^2$ is the random collision number for a λ-scale wave to lose memory of its initial state (Dobrowolny et al. 1980). In fact, from Eq. (5.6) the amplitude δu_λ during one collision can be estimated by $\delta u_\lambda \sim (\lambda/v_A)\left(u_\lambda^2/\lambda\right) \sim u_\lambda^2/v_A$, and hence the number of random collisions $N \sim \langle u_\lambda^2\rangle/\langle(\delta u_\lambda)^2\rangle \sim v_A^2/u_\lambda^2$, where $\langle * \rangle$ represents the random average. In result, the characteristic time $\tau_{T\lambda} \sim \lambda v_A/u_\lambda^2$ and hence the energy transferring rate $\varepsilon_{T\lambda} \sim u_\lambda^4/v_A\lambda$. For the inertial scale region of λ, adopting the Kolmogorov hypothesis of the constant energy transferring rate, that is, $\varepsilon_{T\lambda} = \varepsilon_T$ independent of the scale λ, one has

$$u_\lambda^2 \sim (\varepsilon_T v_A \lambda)^{1/2} \Rightarrow E_k \sim (\varepsilon_T v_A)^{1/2} k^{-3/2}. \tag{5.14}$$

This is so-called the Iroshnikov-Kraichnan spectrum, an isotropic MHD turbulent spectrum, which was viewed as self-evidently correct for 30 years until the mid-1990s, Sridhar and Goldreich (1994) directly challenged the correctness of the Iroshnikov-Kraichnan theory and proposed the resonant 4-wave coupling scenario for weak turbulence of AWs.

5.2.2 Goldreich-Sridhar Theory of AW Turbulence

The ideal MHD or reduced MHD equations (5.3) or (5.6) with $\nu = \nu_m = 0$ have an important feature that they can have steady and stable nonlinear traveling wave solutions with arbitrary amplitude and form of $\mathbf{u}(x, y, z \pm v_A t) = \pm\mathbf{b}(x, y, z \pm v_A t)$, which propagate along (for the sign $-$) or opposite to (for the sign $+$) the magnetic field $\mathbf{B}_0 = B_0\hat{z}$ at the Alfvén velocity $v_A = B_0/\sqrt{\mu_0\rho_0}$ (see e.g., Parker 1979).

The only possible nonlinear coupling is the "collision" between oppositely propagating waves. The Iroshnikov-Kraichnan scenario of AW turbulence describes the "isotropically" random walking process of an AW in the "sea" of other AWs with random phases. Each collision of a λ-scale AW with other oppositely propagating AW (the characteristic collision time $\tau_A \sim \lambda/v_A$) causes only a small variation of its amplitude (i.e., $\delta u_\lambda \sim u_\lambda^2/v_A \ll u_\lambda$), until these variations build up to be comparable with its amplitude so that it has entirely lost memory of its initial state after undergoing successive-N random collisions, implying the effective energy transfer or cascade from the λ-scale AW to smaller scale AWs is finished. Sridhar and Goldreich (1994) argued that this process is equivalent to the resonant 3-wave interaction but does not work because the 3-wave coupling coefficients vanish in isotropic case.

In a magnetized plasma, the parallel and perpendicular variations are caused mainly by the second and third terms of Eq. (5.6), respectively, the former represents the propagation of AW with the characteristic Alfvén time

$$\tau_A \sim \frac{\lambda_z}{v_A} \sim \frac{1}{k_z v_A} \sim \frac{1}{\omega_k}, \tag{5.15}$$

and the latter does the nonlinear interaction between opposite propagation AWs with the characteristic nonlinear time

$$\tau_N \sim \frac{\lambda_\perp}{u_{\lambda_\perp}} \sim \frac{1}{k_\perp u_{\lambda_\perp}}, \tag{5.16}$$

where λ_z (k_z) and $\lambda_\perp$ ($k_\perp$) are the parallel and perpendicular scales (wave numbers) of AWs, respectively. Based on the weak turbulence approximation of $\tau_A \ll \tau_N$ (or i.e., $u_{\lambda_z} \sim u_{\lambda_\perp} \ll v_A$) and the resonant 4-wave interaction description, Sridhar and Goldreich (1994) derived the three dimensional inertial-region energy spectrum with form as follows:

$$\sum_\lambda u_\lambda^2 = \int E(k_z, k_\perp) \frac{\mathrm{d}^3\mathbf{k}}{(2\pi)^3} \Rightarrow E(k_z, k_\perp) \sim \varepsilon_T^{1/3} v_A k_\perp^{-10/3}, \tag{5.17}$$

where the energy transferring rate $\varepsilon_T \sim u_\lambda^2/\tau_T$ can depend only on the parallel wave number k_z and the characteristic transferring time $\tau_T \sim \sqrt{N}\tau_N \sim N\tau_A$.

The three dimensional energy spectrum $E(k_z, k_\perp) \propto k_\perp^{-10/3}$ leads to $u_\lambda^2 \propto k_\perp^{-4/3}$ and hence $N \sim \tau_T/\tau_A \propto k_\perp^{-4/3}$ because of the $k_\perp$-scale independence of ε_T. This implies that as the cascade proceeds to high $k_\perp$ (i.e., short perpendicular scale $\lambda_\perp$), N decreases for fixed k_z. In particular, when N decreases to approaching to the order of unity the weak turbulence approximation will be invalid. In fact, when $N \sim 1$ the inertial region range of the turbulence cascade by the resonant 4-wave interaction will shrink to zero and the turbulence is called the strong turbulence.

Goldreich and Sridhar (1995) introduced the "critical balance" condition to character the strong turbulence of AWs as follows:

$$N \sim 1 \Rightarrow \tau_T \sim \tau_N \sim \tau_A \Rightarrow k_\perp u_{k_\perp} \sim k_z v_A, \tag{5.18}$$

where $k_\perp = 2\pi/\lambda_\perp$. For the inertial region of the strong turbulence, the second Kolmogorov hypothesis of the scale independence of the energy transferring rate, that is, $\varepsilon_T \sim u_{k_\perp}^2/\tau_T \sim u_{k_\perp}^2/\tau_N \sim$ constant leads to

$$u_{k_\perp}^3 \sim \varepsilon_T k_\perp^{-1} \Rightarrow E_{k_\perp} \sim \varepsilon_T^{2/3} k_\perp^{-5/3}, \tag{5.19}$$

to return back to the Kolmogorov spectrum again, but an anisotropic version.

Simultaneously, from the critical balance condition of Eq. (5.18) one has

$$k_z v_A \sim k_\perp u_{k_\perp} \Rightarrow k_z \sim v_A^{-1} \varepsilon_T^{1/3} k_\perp^{2/3}, \tag{5.20}$$

implying the anisotropic cascade of the strong AW turbulence towards small scales, now known as the Goldreich-Sridhar theory of AW turbulence, an anisotropic model of AW turbulent cascade. This scale dependent anisotropy also is the most important result of the Goldreich-Sridhar theory, which predicts that as the turbulent cascade proceeds towards smaller and smaller scales the anisotropy of the wave becomes stronger and stronger, that is, the anisotropic ratio $k_\perp/k_z = \lambda_z/\lambda_\perp \sim v_A \varepsilon_T^{-1/3} k_\perp^{1/3}$ increases with $k_\perp \sim 1/\lambda_\perp$.

The result of the strong turbulence theory by Goldreich and Sridhar (1995) may be universal although it is established on the base of the strong turbulence condition, that is, the critical balance condition. In fact, for an even initially isotropic excitation of small fluctuation of $u_L \ll v_A$ with $k_z \sim k_\perp \sim L^{-1}$ and hence $N \gg 1$ at the injection scale L, the initially weak turbulence develops towards and eventually into the strong turbulence with $N \sim 1$, in which the colliding waves are strongly anisotropic AWs with $k_\perp \gg k_z$ (i.e., $\lambda_\perp \ll \lambda_z$) and faster split into small scale waves at the direction perpendicular than at the parallel to the magnetic field (Goldreich and Sridhar 1995). For the intermediate case between the weak and strong turbulence, Goldreich and Sridhar (1997) further investigated the spectral transition from the weak to strong turbulence and found that the interactions of all orders, i.e., the 3-wave and 4-wave interactions, can have the same contribution to the energy cascade transferring rate, although the 3-wave interaction dominates over all higher order interactions during individual collisions (Ng and Bhattacharjee 1996).

Subsequently, a series of numerical simulations further confirmed the scale dependence of the anisotropy predicted by Goldreich and Sridhar (1995). For instance, Cho and Vishniac (2000) performed directly three-dimensional numerical simulations for MHD turbulence by use of a pseudospectral code to solve the incompressible MHD equation and found that the anisotropy almost is scale independence when the components of the wave vector $\mathbf{k}$, k_z and $k_\perp$, are calculated straightforwardly at the parallel and perpendicular to the direction of the large-scale magnetic field, respectively.

However, for the wave numbers $\tilde{k}_z$ and $\tilde{k}_\perp$ measured relative to the local magnetic field direction, the results can be consistent with the scaling law of the anisotropy, that is, $\tilde{k}_z \propto \tilde{k}_\perp^{2/3}$, predicted by Goldreich and Sridhar (1995). This indicates that the energy transfer of the AW turbulence towards small scales exactly is a local spectral cascade process whose anisotropy depends on the local magnetic field.

Maron and Goldreich (2001) simulated incompressible MHD turbulence for the strong magnetic field case with $\gamma \equiv v_A^2/u_L^2 \gg 1$. Similar to the result by Cho and Vishniac (2000), the simulation result by Maron and Goldreich (2001) showed also that the anisotropy increases with increasing $k_\perp$ such that excited modes are confined inside a cone bounded by $k_z \propto k_\perp^{2/3}$ as predicted by Goldreich and Sridhar (1995). However, their results also have a notable discrepancy that the one-dimensional energy spectra determined from their simulations display $E_k \propto k_\perp^{-3/2}$ predicted by the Iroshnikov-Kraichnan theory, rather than $E_k \propto k_\perp^{-5/3}$ expected by the Goldreich-Sridhar model. In particular, the results of numerical simulations of decaying and forced MHD turbulence without and with mean magnetic field presented by Müller et al. (2003) showed a gradual transition of the perpendicular energy spectrum from the Goldreich-Sridhar form at the weak field case of $\gamma \ll 1$ to the Iroshnikov-Kraichnan spectrum at the strong field case of $\gamma \gg 1$.

5.2.3 *Boldyrev Theory of AW Turbulence*

Motivated by these intriguing numerical findings, Boldyrev (2005, 2006) proposed a new phenomenological model for MHD turbulence, which can lead to an external field dependent energy spectrum such that in the limiting cases of a weak and strong external field the new model can reproduce the Goldreich-Sridhar and Iroshnikov-Kraichnan spectra, respectively. Boldyrev (2005, 2006) further analyzed the nonlinear interaction term in the reduced MHD equation (5.6), $\mathbf{z}^\mp \cdot \nabla \mathbf{z}^\pm$, and proposed that the nonlinear interaction possibly is reduced by a factor $\left(u_{\lambda_\perp}/v_A\right)^\alpha$ due to the dynamically aligned effect between $\mathbf{u}$ and $\mathbf{b}$, where α is some undetermined exponent with the range $0 \le \alpha \le 1$. Moreover, this dynamic alignment effect can be the scale dependent, that is, increases with the scale decreases, so that turbulent structures in small scales become locally anisotropic in the plane perpendicular to the large-scale ambient magnetic field $\mathbf{B}_0$.

Following Boldyrev (2005, 2006), the nonlinear interaction reduced by the dynamic alignment effect in Eq. (5.6) can be estimated by

$$\mathbf{z}^\mp \cdot \nabla \mathbf{z}^\pm \sim \frac{u_{\lambda_\perp}}{\lambda_\perp}\left(\frac{u_{\lambda_\perp}}{v_A}\right)^\alpha. \tag{5.21}$$

Thus, the characteristic time of the nonlinear interaction τ_N may be given by

$$\tau_{N\lambda_\perp} \sim \frac{\lambda_\perp}{u_{\lambda_\perp}}\left(\frac{v_A}{u_{\lambda_\perp}}\right)^\alpha. \tag{5.22}$$

Assuming the strong turbulence condition in small scales, that is, the energy transferring time $\tau_T \sim \tau_N$, the constant energy transferring rate condition, $\varepsilon_T \sim u_{\lambda_\perp}^2/\tau_T \sim$ constant, leads to the inertial-region turbulent energy spectrum as follows

$$\begin{aligned} &u_{\lambda_\perp}^2 \sim \varepsilon_T v_A^\alpha \lambda_\perp u_{\lambda_\perp}^{-(1+\alpha)} \Rightarrow u_{k_\perp}^2 \propto k_\perp^{-2/(3+\alpha)} \Rightarrow \\ &E_{k_\perp} \propto du_{k_\perp}^2/dk_\perp \propto k_\perp^{-(5+\alpha)/(3+\alpha)}. \end{aligned} \tag{5.23}$$

The anisotropy of the scaling law can be obtained by the critical balance condition or equivalently by the causality principle (Boldyrev 2005), that is,

$$\frac{\lambda_z}{v_A} \sim \tau_{N\lambda_\perp} \Rightarrow k_z \propto k_\perp^{2/(3+\alpha)}. \tag{5.24}$$

The condition $E_{k_\perp} dk_\perp = E_{k_z} dk_z$ gives the parallel energy spectrum

$$E_{k_z} = E_{k_\perp} \frac{dk_\perp}{dk_z} \propto k_z^{-2}, \tag{5.25}$$

independent of α and hence independent of the external field strength.

In comparison with the numerical simulation results (Cho and Vishniac 2000; Maron and Goldreich 2001; Müller et al. 2003), the undetermined exponent α may be associated with the external field strength parameter $\gamma = v_A^2/u_L^2$. In consequence, the Goldreich-Sridhar spectrum is obtained by $\alpha \to 0$ for the weak field limit of $\gamma \ll 1$ and the Iroshnikov-Kraichanan spectrum is given by $\alpha \to 1$ for the strong field limit of $\gamma \gg 1$. It is difficult, however, that the alignment exponent α is determined by the simple dimensional analysis.

In fact, the dynamic alignment effect of $\alpha \neq 0$ leads to the local anisotropy of AW structures in the plane perpendicular the large-scale mean magnetic field $\mathbf{B}_0$ (i.e., the l direction in Fig. 5.1), as shown in Fig. 5.1 (Boldyrev 2006). The perpendicular wave vector $k_\perp \sim 1/\lambda_\perp$ (i.e., the λ direction in Fig. 5.1) is along the maximum gradient direction of AWs in the plane perpendicular to $\mathbf{B}_0$, also which is approximately perpendicular to the AW field $\mathbf{b}$ (i.e., the ξ direction in Fig. 5.1). Meanwhile, the wave field $\mathbf{b}$ causes the distortion of the field line and the corresponding field line displacement along $\mathbf{b}$, $\lambda_\times$, can be estimated by

$$\lambda_\times \sim \frac{b_{\lambda_\perp}}{v_A} \lambda_z \propto \lambda_\perp^{3/(3+\alpha)}, \tag{5.26}$$

where $b_{\lambda_\perp} \sim u_{\lambda_\perp}$ and the scaling relations (5.23) and (5.24) have been used. Usually one has $\lambda_\times \gg \lambda_\perp$, implying that individual small-scale AWs appear anisotropic turbulent "eddy" structures.

In the case of decaying MHD turbulence, magnetic and velocity fluctuations can approach their configuration so that $\mathbf{u} = \mathbf{b}$ or $\mathbf{u} = -\mathbf{b}$ and hence the nonlinear interaction vanish in the reduce MHD equation (5.6), called the dynamic alignment

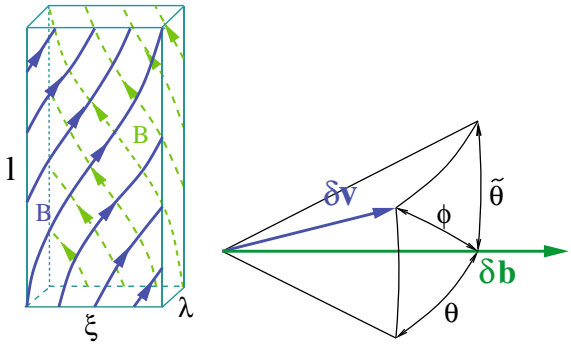

Fig. 5.1 Left: Structures of anisotropic turbulent eddies, in which the large-scale mean magnetic field is in the vertical direction; Right: Sketch of three-dimensional angular alignment relation between velocity and magnetic field fluctuations (reprinted figure with permission from Boldyrev, Phys. Rev. Lett. 96, 115002, 2006, copyright 2006 by the American Physical Society)

effect (Dobrowolny et al. 1980; Grappin et al. 1982; Pouquet et al. 1986). As pointed out by Boldyrev (2006), in the case of driven turbulence the tendency of the dynamic alignment should be preserved although the exact alignment can not be reached because the energy cascade towards mall scales needs to be maintained by non-zero nonlinear interaction. In the steady case, the alignment between the velocity and magnetic field fluctuations should be consistent with maintaining a constant energy transferring rate. This leads to the scaling relation

$$\theta_{\lambda_\perp} \sim \frac{\lambda_\perp}{\lambda_\times} \propto \lambda_\perp^{\alpha/(3+\alpha)}, \tag{5.27}$$

where the scaling relation (5.26) and the alignment approximation $\theta_{\lambda_\perp} \ll 1$ have been used (see the right panel of Fig. 5.1). From the right panel of Fig. 5.1, on the other hand, we have

$$\tilde{\theta}_{\lambda_\perp} \sim \frac{\lambda_\times}{\lambda_z} \propto \lambda_\perp^{1/(3+\alpha)}, \tag{5.28}$$

where the scaling relations (5.24) and (5.26) have been used. Therefore, the misaligned angle between velocity and field fluctuations

$$\phi_{\lambda_\perp} = \sqrt{\theta_{\lambda_\perp}^2 + \tilde{\theta}_{\lambda_\perp}^2} \propto \lambda_\perp^{\alpha/(3+\alpha)} \sqrt{1 + \lambda_\perp^\alpha}. \tag{5.29}$$

If we require further the best alignment to be reached, that is, the minimal misaligned angle $\phi_{\lambda_\perp}$, the condition $\theta_{\lambda_\perp} = \tilde{\theta}_{\lambda_\perp}$ should be satisfied, which minimizes the "uncertainty" of the misaligned angle (Boldyrev 2006). This leads to the alignment exponent $\alpha = 1$, which is corresponding to the Iroshnikov-Kraichnan spectrum in the strong field case of $\gamma \gg 1$. Perhaps this is a universal phenomenon in the small-scale AW turbulence spectra. In fact, for the small-scale fluctuations the so-called

"local external field" actually is the mean fluctuation in larger scales and the larger-scale fluctuation always is stronger relative to the smaller-scale fluctuation. In consequence, for the small-scale AW turbulence, the local external field always can satisfy the strong field condition of $\gamma > 1$.

In addition, the results of some numerical simulations show that the dissipative structures in MHD turbulence are microcurrent sheets rather than filaments (Biskamp and Müller 2000; Maron and Goldreich 2001; Biskamp 2003). This also is consistent with anisotropic structures of turbulent eddies at small scales due to the dynamic alignment effect in the driven turbulence. These small-scale eddies can be viewed as strongly anisotropic sheets or ribbons stretched along the local mean and fluctuation magnetic field lines described by Boldyrev (2006), rather than filaments along the local mean magnetic field but approximate isotropy in the plane perpendicular to the local mean field expected in the Goldreich-Sridhar theory (Goldreich and Sridhar 1995).

5.2.4 Observations of Spectral Anisotropy of AW Turbulence

The solar wind, as supersonic and super-Alfvénic plasma flows outwards from the active solar corona, is ubiquitously in the strong turbulence, in which the majority is dominated by AW turbulence (Tu and Marsch 1995). Also observations of solar wind turbulence further confirmed the theoretical expectation of the anisotropic nature of AW turbulence. For instance, by use of Ulysses satellite observations of the polar fast wind, Horbury et al. (2008) estimated quantitatively the anisotropic power and scaling of magnetic field fluctuation in inertial range MHD turbulence and found for the first time the magnetic power spectra index ~ -2 in the quasi-parallel direction and ~ -1.67 in the quasi-perpendicular direction.

Based on data of high-speed streams measured by the Stereo satellites (A and B) in the ecliptic plane, Podesta (2009) found that overall, the power-law indices resulted from high-speed streams in the ecliptic plane are qualitatively and quantitatively similar to these resulted from the polar fast solar wind by Ulysses observations. However, for high-speed streams in the ecliptic plane the scaling exponent of the perpendicular to parallel power ratio, whose precise value is important for comparisons with turbulence theories, is difficult to determine because there is not sufficient data to obtain reliable measurements at low frequencies where the record length is limited by the relatively short lifetime of high-speed streams in the ecliptic plane. By using the same Ulysses data used by Horbury et al. (2008), Podesta (2009) reproduced the similar results in the inertial range, that is, the spectral index of solar wind turbulence in the inertial range varies continuously from ~ -2 in the quasi-parallel direction to ~ -1.6 in the quasi-perpendicular direction. Meanwhile, he also found the power spectrum has an evident spectral break near $k_\perp \rho_i \sim 1$ when extended the spectrum into the kinetic scales of plasma particles, implying the transition from the inertial to dissipative range, that is, the turbulent cascade transition from AW cascade to KAW cascade process.

Figure 5.2 shows a typical example, in which the upper panel shows clearly the typical characteristic of the variation of the power-law exponent continuously from ~ -2 in the quasi-parallel direction to ~ -1.6 in the quasi-perpendicular direction. While the lower panel presents the perpendicular to parallel power ratio versus the satellite frame frequency ν, which is reversely proportional to the spatial scale, or i.e., directly proportional to the wave number. The scaling law exponent of 0.35 is well consistent with the value $1/3$ expected by the Goldreich-Sridhar theory (or i.e., the weak-field approximation of $\alpha \ll 1$ in the Boldyrev theory). In particular, an evident spectral break occurs between 0.1 and 0.2 Hz near the transition regime from the inertial to dissipative range, implying that the kinetic effects begin to play an

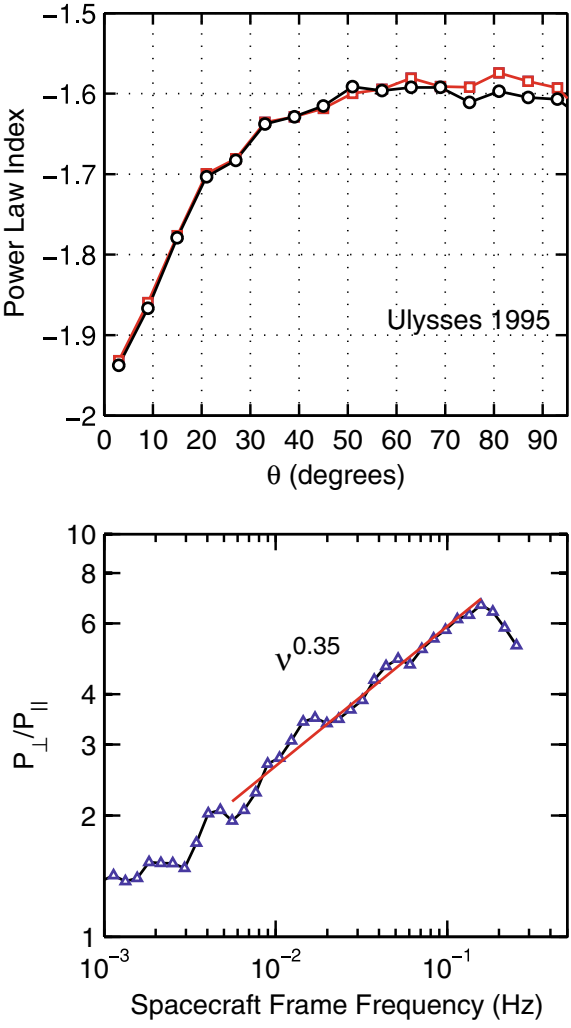

Fig. 5.2 Upper panel: Power-law exponent versus the angle θ between the local mean magnetic field and the mean flow direction (radial direction) for the Ulysses data on 1995 DOY $100 - 130$. The red and black curves are obtained by the power averaged with and without directing selection, respectively; Lower panel: The ratio of the perpendicular to parallel power versus the frequency ν in the satellite frame, in which the red line represents the linear least-squares fit with the slope 0.35 ± 0.04 (from Podesta 2009)

important role in the AW turbulent cascade and the AW turbulent cascade starts to turn into the KAW turbulent cascade.

Wicks et al. (2010) further extended the measurements of the power and spectral index anisotropy of solar wind magnetic field fluctuations from scales larger than the outer scale down to the ion gyroscale, covering the entire inertial range. Their results show that the power spectrum above the outer scale of turbulence is approximately isotropic, while at smaller scales the turbulent cascade causes the power spectral anisotropy: close to ~ -2 along and $\sim -5/3$ across the local magnetic field consistent with a critically balanced Alfvénic turbulence. In particular, they found that an enhancement of the parallel power coincident with a decrease in the perpendicular power presents at the smallest scales of the inertial range, that is, close to the ion gyroscale. They conjectured that this is most likely related to energy injection by ion kinetic modes such as the kinetic firehose instability driven by the ion temperature anisotropy and marks the beginning of the kinetic range, that is, the dissipation range of solar wind turbulence.

Introducing the scale-dependent local mean magnetic field, Luo and Wu (2010) directly calculated for the first time the scaling index of the anisotropy of solar wind turbulence based on the scale-dependent local mean field and resulted in $k_{\parallel} \propto k_{\perp}^{0.61}$ with the index $\sim$0.61 between 2/3 and 1/2, that is, the weak-field limit of $\alpha \to 0$ and the strong-field limit of $\alpha \to 1$, where α is the "depletion" index of the nonlinear interaction due to the dynamic alignment effect (Boldyrev 2005, 2006). In fact, the above observations and others (see Podesta 2013) all show that the "depletion" of the nonlinear interaction due to the dynamic alignment effect can possibly play an important role in the formation of the observed anisotropic power spectra of solar wind AW turbulence, in which the parallel power spectra have the same index ~ -2, independent from the depletion index α, and the perpendicular power spectral index ranges well between $-5/3$ and $-3/2$, that is, the weak-field limit of $\alpha \to 0$ and the strong-field limit of $\alpha \to 1$ (Boldyrev 2005, 2006).

Moreover, detailed analyses of numerical simulations show that the scale-dependent dynamic alignment also can possibly be responsible for the presence of the intermittency in solar wind AW turbulence, especially in small scales (Beresnyak and Lazarian 2006; Mason et al. 2006; Chandran et al. 2015). In more general unbalanced cases between the energy transferring rate and the nonlinear interaction driven rate, the unbalanced turbulent cascade can possibly lead to the formation of intermittent structures in the unbalanced scales, in which the depletion index of the nonlinear interaction $\alpha < 1$. Besides the dynamic alignment, the unbalance turbulent cascade can be caused by other scale-dependent processes, such as the dissipation and dispersion of plasma waves, which both sensitively depend on the wave scales in small scales approaching to the kinetic scales of plasma particles. These will greatly increase the complexity and difficulty of theoretical studies of AW turbulence in small scales. Therefore, the KAW turbulence, the kinetic-scale AW turbulence, must become the new frontier in the plasma physics and turbulence physics communities.

5.3 Gyrokinetic Description of KAWs

5.3.1 Gyrokinetic Approximations

The theories of incompressible MHD turbulence, from the early isotropic Iroshnikov-Kraichnan scenario (Iroshnikov 1963; Kraichnan 1965), to the later Goldreich-Sridhar theory with two-dimensional anisotropy (Sridhar and Goldreich 1994; Goldreich and Sridhar 1995, 1997), and recently the Boldyrev model with three-dimensional anisotropy (Boldyrev 2005, 2006), all propose an anisotropically turbulent cascade process towards small scales. The anisotropic scaling law, $k_\parallel \propto k_\perp^{2/(3+\alpha)}$ with the parameter $0 < \alpha < 1$, indicates that the energy cascades primarily by developing preferentially small scales perpendicular to the local magnetic field, i.e., with $k_\perp \gg k_z$, as schematically shown in Fig. 5.3. As the AW turbulent cascade towards smaller scales proceeds to approaching to the kinetic scales of particles, such as the ion gyroradius ρ_i or the electron inertial length λ_e, AWs inevitably

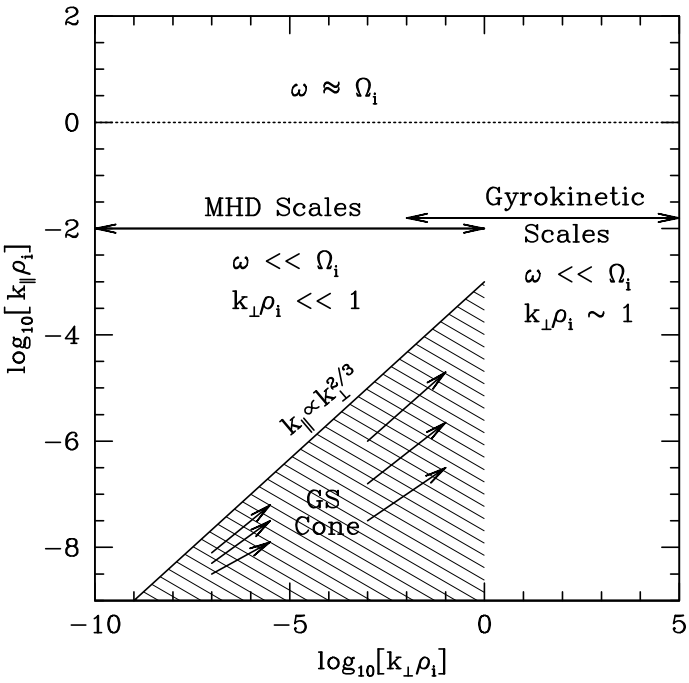

Fig. 5.3 Schematic diagram of the low-frequency, anisotropic AW cascade in wave number space. The horizontal axis is perpendicular wave number; the vertical axis is the parallel wave number, proportional to the frequency. MHD is valid only in the limit $\omega \ll \omega_{ci}$ and $k_\perp \rho_i \ll 1$; gyrokinetic theory remains valid when the perpendicular wave number is of the order of the ion gyroradius, $k_\perp \rho_i \sim 1$. Note that $\omega \to \omega_{ci}$ only when $k_\perp \rho_i \to 1$, so gyrokinetics is applicable for $k_z \ll k_\perp$ (from Howes et al. 2006)

enter the scale range of KAWs where the AW turbulent cascade becomes the KAW turbulent cascade and the MHD theory will be no longer valid.

In the solar wind the mean collision free path of particles $\lambda_c \sim 1$ AU, much larger than the parallel wavelength of AWs, this implies that the solar wind plasma typically is collisionless and the kinetic processes of particles can play an important role in the turbulent cascade of small scale AWs. In particular, due to the intrinsic anisotropy of AW turbulence, low-frequency AWs with frequencies well below the ion gyrofrequency, that is, $\omega \ll \omega_{ci}$ can have short perpendicular wavelengths comparable to the ion gyroradius (i.e., $k_\perp \rho_i \sim 1$), much less than the parallel wavelength of AWs (i.e., $k_\parallel \ll k_\perp$). The motion of individual particles in the small sacle wave fields can be separated well into the fast cyclotron motion around the local magnetic field (with the characteristic time scale $t_f \sim 1/\omega_{ci}$) and the slow drift motion of the gyrocenter (with the characteristic time scale $t_s \sim 1/\omega \gg t_f$). Gyrokinetics is a reduced kinetic theory by averaging over the fast cyclotron motion of charged particles and describes the particle as the charged ring centering at the gyrocenter and moving in the ring-averaged electromagnetic field (Rutherford and Frieman 1968; Frieman and Chen 1982; Howes et al. 2006; Schekochihin et al. 2009). The gyrokinetic approximation retains incompressible AW and the slow magnetosonic wave with the finite Larmor radius effects as KAWs and KSWs (Chen and Wu 2011a, b), the collisionless dissipation due to parallel Landau damping, as well as the Coulomb collisions (if so), but excludes the fast magnetosonic wave and the cyclotron resonance.

Gyrokinetics, a very valuable tool in the study of laboratory plasmas (Chen and Zonca 2016), is particularly suitable for describing the low-frequency, small-scale, and anisotropic AW turbulence, that is, the KAW turbulence, in the solar wind and other astrophysical plasma environments (Howes et al. 2006; Schekochihin et al. 2009). The simplifications of equations for gyrokinetics are mainly based on the low-frequency ($\omega \ll \omega_{ci}$) and small-scale ($\rho_i \ll l_0$) approximations, where l_0 is the scale length of the parallel wavelength $\lambda_\parallel$ much larger than the scale size of the perpendicular wavelength $\lambda_\perp$ (i.e., ρ_i). The former approximation allows to average all quantities over the cyclotron period of particles, and the latter approximation allows to expand all averaged quantities into the series of powers with the small parameter

$$\epsilon = \frac{\rho_i}{l_0} \ll 1. \tag{5.30}$$

Thus, there are three relative scales in the gyrokinetics: the fast gyromotion scale at ω_{ci} and $\rho_i = v_{T_i}/\omega_{ci}$ for the microscopic motions of particles; the intermediate fluctuation scale at ω and l_0 associated with the fluctuations of distribution function and electromagnetic fields in waves; and the slow equilibrium scale at T and L connected to the system macroscopic processes such as heating and inhomogeneity, that is, the outer or injection scale for the turbulence system. For their relative orders one has:

$$\frac{k_\parallel}{k_\perp} \sim \frac{\rho_i}{l_0} \sim O(\epsilon),$$
$$\frac{\omega}{\omega_{ci}} \sim \frac{k_\parallel v_A}{\omega_{ci}} \sim \frac{k_\perp \rho_i}{\sqrt{\beta_i}}\epsilon \sim O(\epsilon), \tag{5.31}$$

where $\beta_i \sim 1$ (or i.e., $v_{T_i} \sim v_A$) has been assumed for the solar wind plasma environment. Figure 5.4 depicts schematically the relative scaling relation in the gyrokinetics. The perpendicular flow velocity $\mathbf{u}_\perp$ is roughly in order of the $\mathbf{E} \times \mathbf{B}/B_0^2$ drift velocity, that is,

$$u_\perp \sim \frac{\mathbf{E} \times \mathbf{B}}{B_0^2} \sim \frac{E}{b}\frac{b}{B_0} \sim O(\epsilon) v_A \sim O(\epsilon) v_{T_i}. \tag{5.32}$$

If using the critical balance and constant energy transferring rate conditions, for the microscopic kinetic scale ρ_i and the macroscopic injected scale L we can have the scaling relation as follows:

$$\epsilon \sim \frac{u_\perp}{v_A} \sim \left(\frac{\rho_i}{L}\right)^{1/3} \Leftrightarrow \frac{l_0}{L} \sim \epsilon^2, \tag{5.33}$$

where the constant energy transferring rate condition of Eq. (5.19) have been used for the injection and kinetic scales, $\lambda \sim L$ and $\lambda \sim \rho_i$. For the case of the solar wind, we have typically $L \sim 10^8$ km and $\rho_i \sim 10^2$ km, and hence $\epsilon \sim (\rho_i/L)^{1/3} \sim 10^{-2}$ and $l_0 \sim 10^4$ km.

Gyrokinetics is most naturally described in gyrocenter coordinates as shown in Fig. 5.4, where the position of a particle $\mathbf{r}$ and velocity $\mathbf{v}$ are given by

$$\mathbf{r} = \mathbf{R}_s - \omega_{cs}^{-1}\mathbf{v} \times \hat{\mathbf{z}}$$
$$\mathbf{v} = v_z\hat{\mathbf{z}} + v_\perp\left(\cos\theta\hat{\mathbf{x}} + \sin\theta\hat{\mathbf{y}}\right), \tag{5.34}$$

where $\mathbf{R}_s$ is the position of the gyrocenter of a s-species particle, v_z and $v_\perp$ are parallel and perpendicular velocities of the particle, and θ is the gyrophase angle. Gyrokinetic averages all quantities over the gyrophase angle θ associated with particles at a fixed gyrocenter $\mathbf{R}_s$ and all quantities associated with electromagnetic fields at a fixed position $\mathbf{r}$, that is,

$$\langle A(\mathbf{r}, \mathbf{v}, t)\rangle_{\mathbf{R}_s} = \frac{1}{2\pi}\oint A(\mathbf{R}_s - \omega_{cs}^{-1}\mathbf{v} \times \hat{\mathbf{z}}, \mathbf{v}, t)d\theta,$$
$$\langle A(\mathbf{R}_s, \mathbf{v}, t)\rangle_{\mathbf{r}} = \frac{1}{2\pi}\oint A(\mathbf{r} + \omega_{cs}^{-1}\mathbf{v} \times \hat{\mathbf{z}}, \mathbf{v}, t)d\theta, \tag{5.35}$$

where the θ integration is done keeping v_z and $v_\perp$ constant.

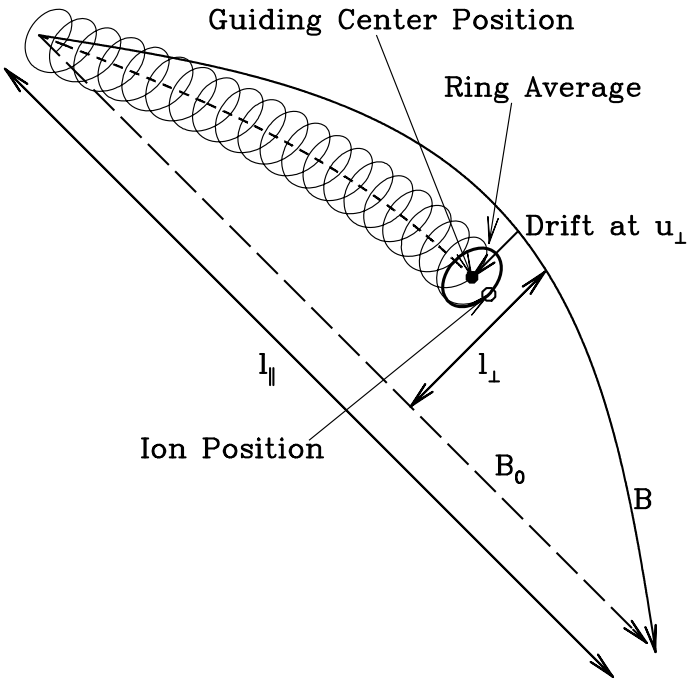

Fig. 5.4 Gyrocenter coordinates and scales in gyrokinetics. The open and filled circles are the particle and its gyrocenter positions, respectively; $l_\perp \sim \lambda_\perp \sim \rho_i$ and $\_ \parallel \sim \lambda_\parallel \sim l_0$ are the characteristic perpendicular and parallel length scales in gyrokinetics, respectively, and $\mathbf{B}_0$ (dashed line) and $\mathbf{B}$ (solid line) are the ambient and perturbed magnetic field, respectively (from Howes et al. 2006)

5.3.2 Gyrokinetic Equations

In the gyrokinetic approximations, the distribution function of the s-species particles can be expanded into power series of ϵ as follows (Howes et al. 2006):

$$f_s = F_{s0}(v,t)\exp\left(-\frac{q_s\Phi(\mathbf{r},t)}{T_{s0}}\right) + h_s(\mathbf{R}_s, v, v_\perp, t) + \delta f_{s2} + \ldots, \tag{5.36}$$

where $v = \sqrt{v_z^2 + v_\perp^2}$ and the equilibrium distribution function, i.e., the zero-order term, is assumed to be an isotropic Maxwellian distribution:

$$F_{s0}(v,t) = \frac{n_{s0}}{(2\pi)^{3/2}\, v_{T_s}^3}\exp\left(-\frac{v^2}{2v_{T_s}^2}\right). \tag{5.37}$$

The first-order distribution function consists of the Boltzmann term caused by the fluctuation electric potential Φ,

$$\left[\exp\left(-\frac{q_s\Phi(\mathbf{r},t)}{T_{s0}}\right)-1\right]F_{s0}(v,t)\simeq-\frac{q_s\Phi(\mathbf{r},t)}{T_{s0}}F_{s0}(v,t), \tag{5.38}$$

and the "charged ring" distribution $h_s(\mathbf{R}_s, v, v_\perp, t)$.

By gyroaveraging the following kinetic equation,

$$\left\langle\frac{\partial f_s}{\partial t}+\mathbf{v}\cdot\nabla f_s+\frac{q_s}{m_s}(\mathbf{E}+\mathbf{v}\times\mathbf{B})\cdot\frac{\partial f_s}{\partial\mathbf{v}}=\left(\frac{\partial f_s}{\partial t}\right)_c\right\rangle_{\mathbf{R}_s}, \tag{5.39}$$

the so-called gyrokinetic equation that governs the ring distribution function $h_s(\mathbf{R}_s, v, v_\perp, t)$ can be derived as follows (Frieman and Chen 1982; Howes et al. 2006; Chen and Zonca 2016):

$$\frac{\partial h_s}{\partial t}+\left\langle\frac{d\mathbf{R}_s}{dt}\right\rangle_{\mathbf{R}_s}\cdot\frac{\partial h_s}{\partial\mathbf{R}_s}=\left\langle\frac{d\mathcal{E}_s}{dt}\right\rangle_{\mathbf{R}_s}\frac{F_{s0}}{T_{s0}}+\left(\frac{\partial h_s}{\partial t}\right)_c, \tag{5.40}$$

where the second term on the right-hand side (i.e., $(\partial h_s/\partial t)_c$) denotes the effect of collisions on the perturbed ring distribution function, called the gyrokinetic collision operator, and the first term,

$$\left\langle\frac{d\mathcal{E}_s}{dt}\right\rangle_{\mathbf{R}_s}\frac{F_{s0}}{T_{s0}}=-\left\langle\frac{\partial f_s}{\partial\mathcal{E}_s}\frac{d\mathcal{E}_s}{dt}\right\rangle_{\mathbf{R}_s}, \tag{5.41}$$

represents the effect of collisionless work done the charged rings by the fluctuation fields, in which $\mathcal{E}_s\equiv m_sv^2/2+q_s\Phi$ is the total energy of the particle and the first adiabatic invariant condition $\langle d\mu_s/dt\rangle_{\mathbf{R}_s}=0$ with $\mu_s=m_sv_\perp^2/2B_0$ has been used.

The drift velocity of the gyrocenter in Eq. (5.40) is given by

$$\left\langle\frac{d\mathbf{R}_s}{dt}\right\rangle_{\mathbf{R}_s}=v_z\hat{\mathbf{z}}-\frac{\partial\langle\Phi\rangle_{\mathbf{R}_s}}{\partial\mathbf{R}_s}\times\frac{\hat{\mathbf{z}}}{B_0}+\frac{\partial\langle\mathbf{v}\cdot\mathbf{A}\rangle_{\mathbf{R}_s}}{\partial\mathbf{R}_s}\times\frac{\hat{\mathbf{z}}}{B_0}, \tag{5.42}$$

where the second and third terms on the right-hand side are the electric and magnetic drifts, respectively, Φ and $\mathbf{A}$ are the scalar and vector electromagnetic potentials with the Coulomb gauge condition of $\nabla\cdot\mathbf{A}=0$ and are related to the perturbed electromagnetic fields by

$$\begin{aligned}\mathbf{E}&=-\nabla\Phi-\frac{\partial\mathbf{A}}{\partial t},\\ \delta\mathbf{B}&=\nabla\times\mathbf{A}.\end{aligned} \tag{5.43}$$

Correspondingly, the fluctuation fields satisfy the Maxwell equations under the gyrokinetic approximations as follows:

$$\begin{aligned}\sum_s q_s \delta n_s &= \sum_s \left(-\frac{q_s^2 n_{s0}}{T_{s0}} \Phi + q_s \int \langle h_s \rangle_{\mathbf{r}} \, d^3\mathbf{v} \right) = 0, \\ \nabla_\perp^2 A_z &= -\mu_0 \sum_s q_s \int v_z \, \langle h_s \rangle_{\mathbf{r}} \, d^3\mathbf{v}, \\ \nabla_\perp \delta B_z &= -\mu_0 \sum_s q_s \int \left\langle \left(\mathbf{v}_\perp \times \hat{\mathbf{z}} \right) h_s \right\rangle_{\mathbf{r}} d^3\mathbf{v}, \end{aligned} \tag{5.44}$$

which are, in turn, the quasi-neutrality condition, the parallel and perpendicular components of the Ampere law, respectively.

5.3.3 Gyrokinetic Dispersion Relation of KAWs

The coupled Eqs. (5.40), (5.42), and (5.44) establish the base of gyrokinetics. Following Howes et al. (2006), the collisionless linear gyrokinetic dispersion equation can be obtained by the straightforward linearization procedure as follows:

$$\left(\frac{\chi_i}{M_z^2} A - AB + B^2 \right) \left(\frac{2A}{\beta_i} - AD + C^2 \right) = (AE + BC)^2 , \tag{5.45}$$

where

$$\begin{aligned} A &= 1 + I_0(\chi_i) e^{-\chi_i} \zeta_i Z(\zeta_i) + \tau_0 \left(1 + I_0(\chi_e) e^{-\chi_e} \zeta_e Z(\zeta_e) \right), \\ B &= 1 - I_0(\chi_i) e^{-\chi_i} + \tau_0 \left(1 - I_0(\chi_e) e^{-\chi_e} \right), \\ C &= c_{i2}(\chi_i) \zeta_i Z(\zeta_i) - c_{e2}(\chi_e) \zeta_e Z(\zeta_e), \\ D &= 2 c_{i2}(\chi_i) \zeta_i Z(\zeta_i) + 2\tau_0 c_{e2}(\chi_e) \zeta_e Z(\zeta_e), \\ E &= c_{i2}(\chi_i) - c_{e2}(\chi_e), \end{aligned} \tag{5.46}$$

where $\zeta_s \equiv \omega / \sqrt{2} k_z v_{T_s}$ and $\tau_0 = T_{i0}/T_{e0}$. From the gyrokinetic dispersion equation, the gyrokinetic dispersion relation, M_z^{GK} depends on the three parameters, the perpendicular wave number $k_\perp \rho_i$, the plasma kinetic to magnetic pressure ratio β, and the ion to electron temperature ratio τ_0.

The first and second factors on the left-hand side of the gyrokinetic dispersion equation (5.45) correspond to the KAW and KSW modes, respectively, and the factor on the right-hand side represents the coupling between KAWs and KSWs that is only important at finite ion gyroradius and high β cases. Here we discuss some limiting cases below. In the high-β limit of $\beta_i \gg 1$, by use of the approximation of the plasma

dispersion function under the small-argument expansion, $Z(\zeta_s) \simeq i\sqrt{\pi}$, Eq. (5.46) is reduced to

$$\begin{aligned} A &\simeq 1 + \tau_0 + i\sqrt{\pi}\zeta_i \left(I_0(\chi_i) e^{-\chi_i} + \sqrt{Q}\tau_0^{3/2} \right), \\ B &\simeq 1 - I_0(\chi_i) e^{-\chi_i}, \\ C &\simeq i\sqrt{\pi}\zeta_i \left(c_{i2}(\chi_i) - \sqrt{Q\tau_0} \right), \\ D &\simeq i2\sqrt{\pi}\zeta_i \left(c_{i2}(\chi_i) + \sqrt{Q/\tau_0} \right), \\ E &\simeq c_{i2}(\chi_i) - 1. \end{aligned} \tag{5.47}$$

In the limit of $\chi_i \sim 1/\sqrt{\beta_i} \ll 1$, the dispersion equation (5.45) is reduced to

$$\left(B - \frac{\chi_i}{M_z^2} \right) D = E^2 \tag{5.48}$$

with $B \simeq \chi_i$, $D \simeq i2M_z\sqrt{\pi/\beta_i}$, and $E \simeq -3\chi_i/2$. Its solution is

$$M_z = \pm \sqrt{1 - \left(\frac{9}{16}\sqrt{\frac{\beta_i}{\pi}}\chi_i \right)^2} - i\frac{9}{16}\sqrt{\frac{\beta_i}{\pi}}\chi_i. \tag{5.49}$$

In the long wavelength limit $\chi_i \ll 1/\sqrt{\beta_i}$, this leads to the ordinary AW of $M_z = \pm 1$ with weak damping of $\omega_i \ll \omega_r$. When $\chi_i > (16/9)\sqrt{\pi/\beta_i}$, the dispersion relation of Eq. (5.49) leads to a purely damped mode.

On the other hand, for the low-β case of $\beta_i \ll 1$, the gyrokinetic dispersion equation (5.45) is reduced to

$$\left(\frac{\chi_i}{M_z^2} A - AB + B^2 \right) \frac{2A}{\beta_i} = 0. \tag{5.50}$$

The second factor $A = 0$ leads to the ion acoustic wave in the long wavelength limit of $\chi_i \ll 1$, that is,

$$M_z = \pm\sqrt{\frac{\beta_e}{2}} - i\sqrt{\frac{\pi\beta_i}{16}}\tau_0^{-2} e^{-1/2\tau_0}. \tag{5.51}$$

The first factor of Eq. (5.50),

$$\frac{\chi_i}{M_z^2} A - AB + B^2 = 0, \tag{5.52}$$

corresponds to KAWs in low-β plasmas. In the kinetic regime of $Q < \beta_i \ll 1$, expanding the ion and electron dispersion functions in large and small arguments, respectively, one has

$$A \simeq 1+\tau_0 - I_0(\chi_i)e^{-\chi_i} \\ +iM_z\sqrt{\frac{\pi}{\beta_i}}\left(I_0(\chi_i)e^{-\chi_i-M_z^2/\beta_i}+\sqrt{Q}\tau_0^{3/2}I_0(\chi_e)e^{-\chi_e}\right). \tag{5.53}$$

The resulting dispersion relation may be obtained by the weakly damping approximation of $|\mathrm{Im}M_z| \ll |\mathrm{Re}M_z|$ as follows:

$$\mathrm{Re}M_z = \pm\sqrt{\frac{\left(1+\tau_0-I_0(\chi_i)e^{-\chi_i}\right)\chi_i}{\tau_0 I_0(\chi_e)e^{-\chi_e}B}}, \\ \mathrm{Im}M_z = -\frac{\chi_i e^{\chi_e}}{2I_0(\chi_e)}\sqrt{\frac{\pi}{\beta_i}}\left(\frac{I_0(\chi_i)}{\tau_0^2 I_0(\chi_e)}e^{\chi_e-\chi_i-M_z^2/\beta_i}+\sqrt{\frac{Q}{\tau_0}}\right). \tag{5.54}$$

In the inertial regime of $\beta_i < Q \ll 1$, the expansion of all plasma dispersion functions in large arguments gives approximation

$$A \simeq B - \frac{I_0(\chi_e)e^{-\chi_e}}{M_z^2}\frac{\beta_i}{2Q}+iM_z\sqrt{\frac{\pi}{\beta_i}}\times \\ \left(I_0(\chi_i)e^{-\chi_i-M_z^2/\beta_i}+\sqrt{Q}\tau_0^{3/2}I_0(\chi_e)e^{-\chi_e-Q\tau_0M_z^2/\beta_i}\right). \tag{5.55}$$

This leads to the dispersion relation,

$$\mathrm{Re}M_z = \pm\sqrt{\frac{I_0(\chi_e)e^{-\chi_e}\beta_i\chi_i}{\left(2Q\chi_i+I_0(\chi_e)e^{-\chi_e}\beta_i\right)B}}, \\ \mathrm{Im}M_z = -\frac{2Q^2I_0(\chi_e)e^{-\chi_e}\beta_i\chi_i^3}{\left(2Q\chi_i+I_0(\chi_e)e^{-\chi_e}\beta_i\right)^3B^2}\sqrt{\frac{\pi}{\beta_i}}\times \\ \left(I_0(\chi_i)e^{-\chi_i-M_z^2/\beta_i}+\sqrt{Q}\tau_0^{3/2}I_0(\chi_e)e^{-\chi_e-Q\tau_0M_z^2/\beta_i}\right). \tag{5.56}$$

For the short-wavelength case of the perpendicular wavelength between the ion and electron gyroradii, $\chi_i \gg 1 \gg \chi_e$, we have $A \simeq 1+\tau_0\left(1+i\sqrt{\pi}\zeta_e\right)$, $B \simeq -E \simeq 1$, $C \simeq -i\sqrt{\pi}\zeta_e$, and $D \simeq i2\sqrt{\pi}\zeta_e/\tau_0$. Thus, the solution of the gyrokinetic dispersion equation (5.45) becomes

$$\mathrm{Re}M_z = \pm\frac{\sqrt{2}k_\perp\rho_i}{\sqrt{\beta_i+2\tau_0/\left(1+\tau_0\right)}}, \\ \mathrm{Im}M_z = -\frac{\chi_i}{2}\sqrt{\frac{Q\pi}{\tau_0\beta_i}}\left\{1+\left[\frac{\left(1+\tau_0\right)\beta_i}{2\tau_0+\left(1+\tau_0\right)\beta_i}\right]^2\right\}. \tag{5.57}$$

This agrees with the KAW dispersion relation in the short-wavelength limit (Kingsep et al. 1990). In fact, for the short-wavelength case of $k_\perp\rho_i \gg 1$, the low-frequency

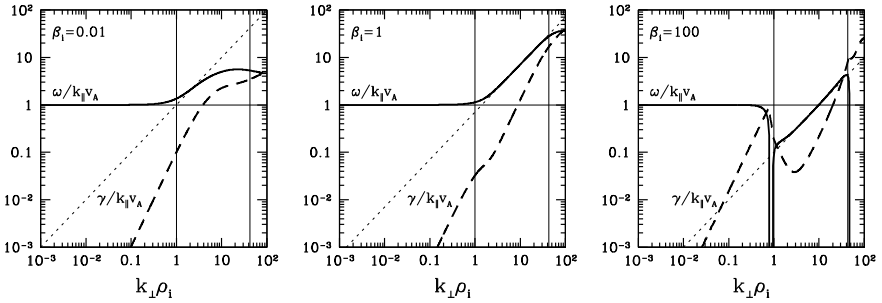

Fig. 5.5 Numerical solutions of the linear gyrokinetic dispersion relation showing the transition from AWs in the inertial range ($k_\perp\rho_i \ll 1$) to KAWs in the ion ($k_\perp\rho_i \sim 1$) and electron ($k_\perp\rho_e \sim 1$) gyrokinetic ranges: Panels, from left to right, show three cases for $\beta_i = 0.01, 1$, and 100, respectively, where bold solid and dashed lines represent the real frequency ω and the damping rate γ, respectively, and dotted lines give the asymptotic KAW solution in the short-wavelength limit case of $k_\perp\rho_i \gg 1$ by Eq. (5.56). All solutions are normalized by the Alfvén frequency $\omega_A \equiv k_z v_A$ (denoted by the horizontal line) and they are functions of $k_\perp$ only in gyrokinetics. Two vertical lines show the ion ($k_\perp\rho_i = 1$) and electron ($k_\perp\rho_e = 1$) gyroradius, respectively. Finally for the sake of simplicity the parameter $\tau_0 = 1$ has been used (from Schekochihin et al. 2009, ©AAS reproduced with permission)

dynamics is dominated by KAWs. When the AW cascade approaches to the wavelength $k_\perp\rho_i \sim 1$, some fraction of the AW energy seeps through to wavelengths smaller than the ion gyroradius and is channeled into a cascade of KAWs. This cascade can extend to smaller wavelengths until approaching the electron gyroradius, $k_\perp\rho_e \sim 1$, at which the KAWs are dissipated by the electron Landau damping.

Figure 5.5 shows the numerical solutions of the linear dispersion relations of the gyrokinetics, which illustrates how the AW becomes a dispersive KAW and the kinetic Landau damping becomes important as the wave scale approaches the ion gyroscale.

5.4 Theory and Simulation of KAWs Turbulence

5.4.1 Basic Properties of KAW Turbulence

When the AW turbulence cascades to small scales comparable to the kinetic scales of plasma particles, such as $k_\perp\rho_i \sim 1$, the AWs become dispersive, that is, KAWs. For the kinetic physics of low-frequency KAW with frequencies $\omega \ll \omega_{ci}$, the gyrokinetics presented in the last section provides a powerful tool and can well describe the low-frequency KAWs in a wide wave-number range from the ion gyroscale ($k_\perp\rho_i \ll 1$) to the electron gyroscale ($k_\perp\rho_e \sim 1$). Based on the gyrokinetics, the last section discusses analytically the basic characteristics of KAWs, including their linear dispersion relations and Landau damping. Besides these small-scale KAWs have

strongly anisotropic characteristics, the dispersion of KAWs breaks the original critical balance of the AW turbulence, the polarization of KAWs contains perturbations of plasma density and magnetic field strength, and the collisionless damping of KAWs due to the wave-particle interaction leads to the dissipation of the turbulent wave energy. These factors all can significantly influence the turbulent cascade process and the scaling law of the turbulence spectrum. Moreover, these new characteristics of KAWs all are sensitively dependent on the local plasma parameters. Meanwhile, other modes presented nearly the ion gyroscales, such as whistler, magnetosonic, and ion-Bernstein waves, also could possibly play some role in the dynamical cascading and coupling of turbulent waves. These all inevitably result in the great increase of the complexity and difficulty of KAW turbulence.

In order to simplify further the complexity, another approximation often used in the ion gyroscale range of $\sqrt{Q} \ll k_\perp \rho_i \ll 1/\sqrt{Q}$ is the small-parameter expansion of the electron gyrokinetic equation in powers of $\sqrt{Q}$. This approximation also means

$$k_\perp \rho_e \sim \sqrt{Q} k_\perp \rho_i \ll 1. \tag{5.58}$$

Thus, the gyrokinetics of electrons may be reduced further to the dynamics of a magnetized fluid with the perturbed density δn_e and field-aligned flow velocity u_{ez}, which are given by Schekochihin et al. (2009)

$$\begin{aligned} \frac{\delta n_e}{n_{e0}} &= -\frac{Ze\Phi}{T_{i0}} + \sum_{\mathbf{k}} \frac{e^{i\mathbf{k}\cdot\mathbf{r}}}{n_{i0}} \int J_0(k_\perp \rho_i') h_{i\mathbf{k}} d^3\mathbf{v}, \\ u_{ez} &= \frac{1}{\mu_0 e n_{e0}} \nabla_\perp^2 A_z + \sum_{\mathbf{k}} \frac{e^{i\mathbf{k}\cdot\mathbf{r}}}{n_{i0}} \int v_z J_0(k_\perp \rho_i') h_{i\mathbf{k}} d^3\mathbf{v}, \end{aligned} \tag{5.59}$$

where $Z = q_i/e$ is the ion charge number, $\rho_i' = v_\perp/\omega_{ci}$ and $\mathbf{R}_e \simeq \mathbf{r}$ has been used because of the smallness of the electron gyroradius ρ_e. The perturbed field equations can be written as:

$$\frac{\partial A_z}{\partial t} + \hat{\mathbf{b}} \cdot \nabla \Phi = \hat{\mathbf{b}} \cdot \nabla \left(\frac{T_{e0}}{e} \frac{\delta n_e}{n_{e0}} \right), \tag{5.60}$$

$$\frac{d}{dt} \left(\frac{\delta n_e}{n_{e0}} - \frac{\delta B_z}{B_0} \right) + \hat{\mathbf{b}} \cdot \nabla u_{ez} = -\frac{T_{e0}}{eB_0} \left\{ \frac{\delta n_e}{n_{e0}}, \frac{\delta B_z}{B_0} \right\}, \tag{5.61}$$

and

$$\begin{aligned} \frac{\delta B_z}{B_0} = \frac{\beta_i}{2} \left(1 + \frac{Z}{\tau_0} \right) \frac{Ze\Phi}{T_{i0}} - \frac{\beta_i}{2} \times \\ \sum_{\mathbf{k}} \frac{e^{i\mathbf{k}\cdot\mathbf{r}}}{n_{i0}} \int \left(\frac{Z}{\tau_0} J_0(k_\perp \rho_i') + \frac{2v_\perp^2}{v_{T_i}^2} \frac{J_1(k_\perp \rho_i')}{k_\perp \rho_i'} \right) h_{i\mathbf{k}} d^3\mathbf{v}, \end{aligned} \tag{5.62}$$

where

$$\begin{aligned}\frac{d}{dt} &\equiv \frac{\partial}{\partial t} + \mathbf{u}_E \cdot \nabla = \frac{\partial}{\partial t} + \frac{1}{B_0}\{\Phi, \cdots\},\\ \hat{\mathbf{b}} \cdot \nabla &\equiv \frac{\partial}{\partial z} + \frac{\delta \mathbf{B}_\perp}{B_0} \cdot \nabla = \frac{\partial}{\partial z} - \frac{1}{B_0}\{A_z, \cdots\},\end{aligned} \tag{5.63}$$

$\mathbf{u}_E = \hat{\mathbf{z}} \times \nabla_\perp \Phi / B_0$, and the Poisson brackets "$\{A, B\}$" are defined by

$$\{A, B\} \equiv \hat{\mathbf{z}} \cdot (\nabla A \times \nabla B)\,. \tag{5.64}$$

The above Eqs. (5.59)–(5.62), combining the ion gyrokinetic equation (5.40) for $s = i$, give the kinetic description of plasma fluctuations near the ion gyroscale.

For the long-wavelength (or weak dispersion) case of $k_\perp \rho_i \ll 1$, the expansion of the gyrokinetics in $k_\perp \rho_i$ can obtain precisely the similar results with that by the reduced MHD description, in which there is no change in the physical nature until the ion gyrokinetic range of $k_\perp \rho_i \sim 1$. The understanding of the physics of turbulent cascade processes in this transition regime is still very poor. However, on the other side of this transition regime, that is, in the short-wavelength limit of $k_\perp \rho_i \gg 1$, some further simplification is possible because this short-wavelength limit indicates that $k_\perp \rho_i' \gg 1$ and hence the all Bessel functions in Eqs. (5.59) and (5.62) are small. This results in Eqs. (5.59) and (5.62) to be reduced to

$$\begin{aligned}\frac{\delta n_i}{n_{i0}} &= -\frac{Ze\Phi}{T_{i0}} = -\sqrt{\frac{2}{\beta_i}}\frac{\phi}{\rho_i v_A},\\ u_{ez} &= \frac{1}{\mu_0 e n_{e0}} \nabla_\perp^2 A_z = -\frac{\rho_i \nabla_\perp^2 \psi}{\sqrt{\beta_i/2}},\\ \frac{\delta B_z}{B_0} &= \frac{\beta_i}{2}\left(1 + \frac{Z}{\tau_0}\right)\frac{Ze\Phi}{T_{i0}} = \sqrt{\frac{\beta_i}{2}}\left(1 + \frac{Z}{\tau_0}\right)\frac{\phi}{\rho_i v_A},\end{aligned} \tag{5.65}$$

where $\phi \equiv \Phi / B_0$ and $\psi \equiv -v_A A_z / B_0$ are the so-called scalar stream and flux functions. The first equation here indicates that the ion response is approximated by the Boltzmann distribution in the electrostatic potential field Φ, the second equation implies that the contribution of the ions on the field-aligned current is ignorable, and the third equation expresses that the magnetic pressure is balanced by the electron and ion kinetic pressures.

Substituting Eq. (5.65) into the field equations (5.60) and (5.61), a closed equation system of the scalar stream and flux functions ϕ and ψ can be obtained as follows:

$$\begin{aligned}\frac{\partial \psi}{\partial t} &= v_A\left(1 + \frac{Z}{\tau_0}\right)\hat{\mathbf{b}} \cdot \nabla \phi,\\ \frac{\partial \phi}{\partial t} &= -\frac{v_A}{1 + (1 + Z/\tau_0)\,\beta_i/2}\hat{\mathbf{b}} \cdot \nabla\left(\rho_i^2 \nabla_\perp^2 \psi\right).\end{aligned} \tag{5.66}$$

This equation system is also referred as the equations of the electron reduced MHD, in which the magnetic field is frozen into the electron flow velocity $\mathbf{v}_e$, while the ions are immobile, that is, $\mathbf{u}_i \sim 0$ (Kingsep et al. 1990). The linear dispersion relation of this electron reduced MHD equation system is given by the dispersion equation (5.57) (instead of τ_0 by τ_0/Z for $Z \neq 1$) and describes KAWs in the short-wavelength limit of $\chi_i \gg 1$. The polarization relations of its two linear eigenmodes can be expressed by

$$\varphi_{\mathbf{k}}^{\pm} = \sqrt{\frac{Z+\tau_0}{\tau_0}\left(1+\frac{Z+\tau_0}{\tau_0}\frac{\beta_i}{2}\right)}\frac{1}{\rho_i}\phi_{\mathbf{k}} \mp k_\perp \psi_{\mathbf{k}}, \tag{5.67}$$

which represent the parallel (i.e., $M_z > 0$ for a single "+") and antiparallel (i.e., $M_z < 0$ for a single "−") propagating KAWs, respectively. In particular, for the electric and magnetic field fluctuations of the KAWs we have

$$\begin{aligned}
\frac{\delta \mathbf{B}_{\mathbf{k}}}{B_0} &= \hat{\mathbf{z}}\sqrt{\frac{1+Z/\tau_0}{2+(1+Z/\tau_0)\,\beta_i}}\frac{\varphi_{\mathbf{k}}^{+}+\varphi_{\mathbf{k}}^{-}}{2v_A} - i\hat{\mathbf{z}}\times\hat{\mathbf{k}}_\perp\frac{\varphi_{\mathbf{k}}^{+}-\varphi_{\mathbf{k}}^{-}}{2v_A} \\
&= -i\hat{\mathbf{z}}\times\hat{\mathbf{k}}_\perp\frac{k_\perp\psi_{\mathbf{k}}}{v_A} + \hat{\mathbf{z}}\left(1+\frac{Z}{\tau_0}\right)\frac{\phi_{\mathbf{k}}}{\rho_i v_A} \\
\frac{\mathbf{E}_{\perp\mathbf{k}}}{B_0} &= -i\mathbf{k}_\perp\frac{\Phi_{\mathbf{k}}}{B_0} + i\omega_{\mathbf{k}}\frac{\mathbf{A}_{\perp\mathbf{k}}}{B_0} \\
&= \left(-i\mathbf{k}_\perp + \hat{\mathbf{z}}\times\mathbf{k}_\perp\frac{\omega_{\mathbf{k}}}{\omega_{ci}}\frac{\beta_i}{2}\frac{Z+\tau_0}{\tau_0\chi_i}\right)\phi_{\mathbf{k}}.
\end{aligned} \tag{5.68}$$

This indicates that the waves have an elliptically right-hand polarization with an elongated ellipse because $|\omega_{\mathbf{k}}/\omega_{ci}| \ll 1$.

Similarly to the reduced MHD equations, the electron reduced MHD equation system (5.66) with the Elsässer-like variables $\varphi^{\pm}$ in the velocity dimension also allows steady and stable nonlinear traveling wave solutions with arbitrary amplitude, which can be constructed by setting the Poisson brackets to be equal to zero that leads to

$$\begin{aligned}
\{\psi,\ \phi\} = 0 &\Rightarrow \psi = c_1\phi \\
\{\psi,\ \rho_i^2\nabla_\perp^2\psi\} = 0 &\Rightarrow \rho_i^2\nabla_\perp^2\psi = c_2\psi,
\end{aligned} \tag{5.69}$$

where c_1 and c_2 are two undetermined constants. Substituting them into the equation system (5.66), one has

$$c_1^2 = -\frac{1}{c_2}\left(1+\frac{Z}{\tau_0}\right)\left(1+\frac{Z+\tau_0}{\tau_0}\frac{\beta_i}{2}\right), \tag{5.70}$$

implying $c_2 < 0$ for real solutions. In gyrokinetics, in fact, the Poisson bracket nonlinearity vanishes for any monochromatic KAWs in the wave number $\mathbf{k}$ space because the Poisson bracket of two KAWs with wave numbers $\mathbf{k}$ and $\mathbf{k}'$ is directly propor-

tional to $\hat{\mathbf{z}} \cdot (\mathbf{k} \times \mathbf{k}')$. Therefore, any monochromatic linear KAWs can be also an exact nonlinear solution with an arbitrary amplitude and the constant $c_2 = -2k_\perp^2 \rho_i^2$.

However, different from the AW case, the nonlinear interaction of two KAWs can occur not only between counterpropagating KAWs but also between copropagating KAWs because their dispersive nature allows the fast one of the copropagating waves with different wave numbers $k_\perp$ to catch up the slow one and to interact with it.

5.4.2 *Power Spectra of KAW Turbulence*

Based on the electron reduced MHD equation system (5.66), the scaling law of KAW turbulence can be obtained by combining the constant-flux KAW cascade and the critical balance hypotheses. As the AW turbulence in the inertial range, the critical balance of turbulent cascade is set up by the hypothesis that the parallel correlation length $\lambda_z \sim k_z^{-1}$ is determined by the wave propagating distance in the nonlinear decorrelation time $\tau_{KTk_\perp} \sim k_\perp^{-1} u_E^{-1} \sim k_\perp^{-2} \phi_{k_\perp}^{-1}$, that is, the linear propagating time scale $\tau_L \sim \omega^{-1} \sim \tau_{KTk_\perp}$ (the nonlinear interaction time scale). This leads to

$$\tau_L \sim \tau_{KTk_\perp} \Rightarrow \frac{\sqrt{1+\beta_i}}{\sqrt{2} k_\perp \rho_i k_z v_A} \sim \frac{1}{k_\perp^2 \phi_{k_\perp}}, \tag{5.71}$$

where the scaling relation between the scalar flow and magnetic functions, $\psi_{k_\perp} = c_1 \phi_{k_\perp} \sim \sqrt{1+\beta_i}\phi_{k_\perp}/\rho_i k_\perp$, and $Z = \tau_0 = 1$ have been used. The constant-flux KAW cascade indicates the kinetic energy transferring rate $\varepsilon_{KTk_\perp}$ independent of $k_\perp$, that is,

$$\varepsilon_{KTk_\perp} \sim \frac{k_\perp^2 \psi_{k_\perp}^2}{\tau_{KTk_\perp}} \sim \frac{1+\beta_i}{\rho_i^2} \frac{\phi_{k_\perp}^2}{\tau_{KTk_\perp}} \sim \varepsilon_{KT} = \text{constant}. \tag{5.72}$$

The combination of Eqs. (5.71) and (5.72) leads to the the scaling relations of the scalar potential $\phi_{\mathbf{k}}$ and the anisotropy as follows:

$$\begin{aligned} \phi_{\mathbf{k}} &\sim \frac{\varepsilon_{KT}^{1/3} \rho_i^{2/3}}{(1+\beta_i)^{1/3}} k_\perp^{-2/3}; \\ k_z &\sim \frac{\varepsilon_{KT}^{1/3} (1+\beta_i)^{1/6}}{\rho_i^{1/3} v_A} k_\perp^{1/3}. \end{aligned} \tag{5.73}$$

In particular, from the polarization relations in Eq. (5.68) the energy spectral densities of magnetic and electric fields for KAWs can be obtained as follows:

$$E_{Bk_\perp} \sim \frac{d}{dk_\perp}|\phi_{\mathbf{k}}|^2 \sim k_\perp^{-7/3};$$
$$E_{Ek_\perp} \sim \frac{d}{dk_\perp}|k_\perp \phi_{\mathbf{k}}|^2 \sim k_\perp^{-1/3}. \tag{5.74}$$

The results of numerical simulations based on the electron MHD turbulence also showed similar scaling relations (Biskamp et al. 1996, 1999; Cho and Lazarian 2004).

Figure 5.6 illustrates the critical balance for the transition of the KAW turbulent cascade from the low wave number regime of $k_\perp \rho_i \ll 1$ to high wave number regime of $k_\perp \rho_i \gg 1$. The critical balance condition of $\omega = \omega_{\rm nl}$ constrains the turbulent energy flow cascading along the path in the $k_z - k_\perp$ plane, which is given by the solid line in Fig. 5.6. From Fig. 5.6, the KAW turbulent cascading process towards smaller scales has the same anisotropic scaling (i.e., $k_z \propto k_\perp^{2/3}$) with that of the AW turbulence described by the Goldreish-Sridhar theory until the transition point at $k_\perp \rho_i = 1$ is approached. Above this transition point the anisotropy becomes

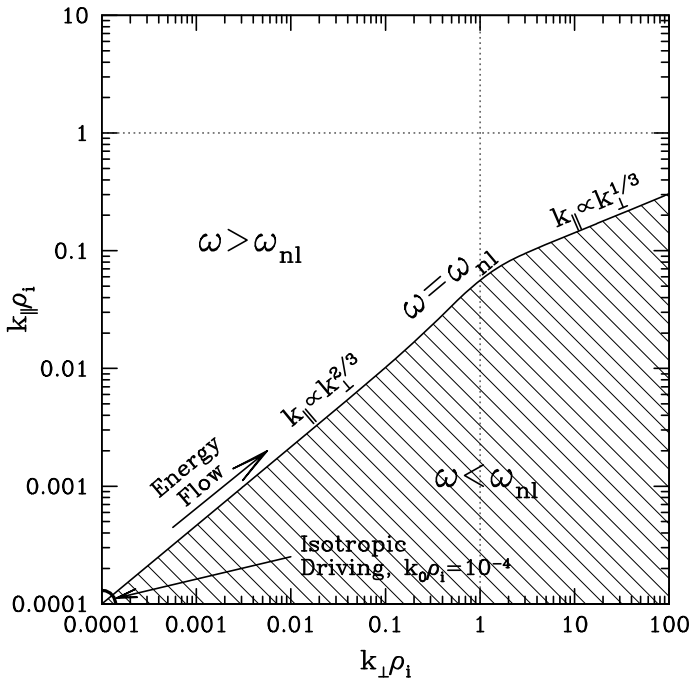

Fig. 5.6 Schematic diagram of the critical balance and anisotropy for the KAW turbulent cascade from low wave numbers of $k_\perp \rho_i \ll 1$ to high wave numbers of $k_\perp \rho_i \gg 1$. The horizontal and vertical axes are the perpendicular ($k_\perp \rho_i$) and parallel ($k_\parallel \rho_i$) wave numbers, respectively. $\omega = M_z k_z v_A$ and $\omega_{\rm nl} = k_\perp v_\perp$ are the linear wave and nonlinear interaction frequencies, respectively. The critical balance is given by $\omega = \omega_{\rm nl}$, and $\omega >$ or $< \omega_{\rm nl}$ correspond to the weak or over-strong turbulence, respectively (from Howes et al. 2008b)

stranger, that is, $k_z \propto k_\perp^{1/3}$, implying that the KAW turbulence faster develops into field-aligned filamentous structures in the kinetic scales of $k_\perp \rho_i > 1$.

5.4.3 *AstroGK Simulations of Ion-Scale KAW Turbulence*

Based on some fluid codes, the critical balance and its leading to results have been examined and verified extensively in MHD simulations for AW turbulence (Cho and Vishniac 2000; Maron and Goldreich 2001; Müller et al. 2003) and in electron MHD simulations for kinetic turbulence (Biskamp et al. 1996, 1999; Cho and Lazarian 2004). However, these fluid codes can not properly model the effect of wave-particle interactions and the kinetic dissipation in kinetic turbulence. In order to more properly take account of the kinetic effects due to wave-particle interactions in astrophysical plasmas, a kinetic simulation, called the AstroGK code, has been developed based on the gyrokinetic theory (Howes et al. 2006; Schekochihin et al. 2009; Numata et al. 2010). One of benchmarks to check the applicability of numerical simulations is to reproduce analytical results of the linear theory. The applicability of the AstroGK code has been checked extensively to agree well with the linear gyrokinetic theory in the kinetic scales of plasma particles. For example, Fig. 5.7 displays the normalized real frequency ($\omega/k_\parallel v_A$) and damping rate ($\gamma/k_\parallel v_A$)of KAWs produced by the AstroGK (squares) as the function of the normalized perpendicular wave number $k_\perp \rho_i$ and the corresponding analytic results from the linear collisionless gyrokinetic theory (lines) in the typical kinetic scale range from $k_\perp \rho_i = 0.1$ to $k_\perp \rho_i = 10$ (Howes et al. 2008a).

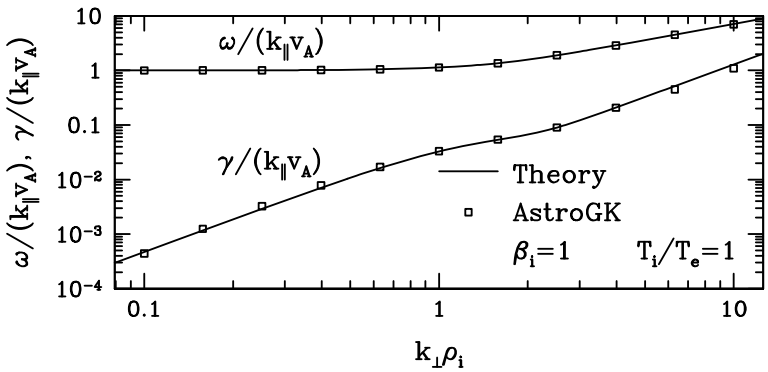

Fig. 5.7 Normalized frequencies $\omega/k_\parallel v_A$ and damping rates $\gamma/k_\parallel v_A$ versus normalized perpendicular wave number $k_\perp \rho_i$ for a plasma with $\beta_i = 1$ and $T_i = T_e$. The AstroGK code (squares) correctly reproduces the analytic results from the linear collisionless gyrokinetic dispersion relation (reprinted the figure with permission from Howes et al., Phys. Rev. Lett. 100, 065004, 2008a, copyright 2008 by the American Physical Society)

From Fig. 5.7, one can find almost exact agreement between the numerical simulation by the AstroGK code and the analytical results from the linear gyrokinetic theory, in which the ordinary AW dispersion relation ($\omega = \pm k_\parallel v_A$) with little damping ($\gamma \ll k_\parallel v_A$) is obtained again for the MHD limit of $k_\perp \rho_i \ll 1$ and for the high wave-number case of $k_\perp \rho_i \gg 1$ the KAW dispersion relation $\omega = \pm k_\parallel v_A k_\perp \rho_i / \sqrt{\beta_i/2 + \tau/(1+\tau)}$ (see Eq. 5.57) with stronger damping can be rediscovered. TenBarge and Howes (2012) further investigated the applicability of the critical balance to kinetic turbulence and found that the results of kinetic simulations can well agree with the theoretical predictions. This implies that the critical balance also is satisfied well in kinetic turbulence and a more strongly anisotropic turbulent cascade may extend into the kinetic scales.

Howes et al. (2008a, 2011) used the AstroGK code more in detail to solve numerically the gyrokinetic and Maxwell coupled equations (5.40), (5.42), and (5.44), in which the equilibrium distributions for electrons (F_{e0}) and protons (F_{i0}) both are assumed are uniform Maxwellian distributions, the real ion-electron mass ratio $m_i/m_e = Q^{-1} = 1836$ is used. The spatial coordinates (x, y) perpendicular to the mean magnetic field ($\mathbf{B}_0$) are dealt with pseudospectrally and the development along the parallel coordinate z is calculated by an upwind finite-difference scheme. Collisional effects are included by a conservative linearized collision operator of consisting of energy diffusion and pitch-angle scattering (Abel et al. 2008; Barnes et al. 2009). For the kinetic simulation of collisionless kinetic turbulence in astrophysical plasmas one of main difficulties is how to model the energy injection at the largest driving scales and how to remove the energy at the smallest dissipating scales because the kinetic scales are much less than the physical driving scale and physical processes of astrophysical plasmas in the kinetic scales have naturally collisionless characteristic.

For a kinetic system to reach a steady state in kinetic simulations, the driving injection power in large scales into the system must be dissipated into heat in small scales. In a collisionless or weak-collision kinetic system, the distributions possibly develop some non-physical small-scale structures near the grid resolution scale of the numerical simulation, which leads to falsely and strongly numerical gradients and disturbs significantly the system evolution, even no reachable steady state. Thus, numerical simulations of kinetic turbulence must include proper collisions as well as sufficient grid resolutions to guarantee the correct relationship between small-scale structures in velocity and position space. In general, it is very difficult that a physical collision operator simultaneously satisfies the grid resolution requirements for ions and electrons. Therefore, a artificially enhanced hypercollisionality (analogous to the hyperviscosity in fluid simulations) often is involved to terminate the cascade of kinetic turbulence at small scales close to the grid scale.

Using the AstroGK code and employing a hypercollisionality with the form of a pitch-angle scattering operator dependent on the collision rate $\nu_h\,(k_\perp/k_{\perp d})^8$, where $k_{\perp d}$ is the grid wave number (i.e., the maximum wave number in the kinetic system), Howes et al. (2008a) presented the first fully electromagnetic gyrokinetic simula-

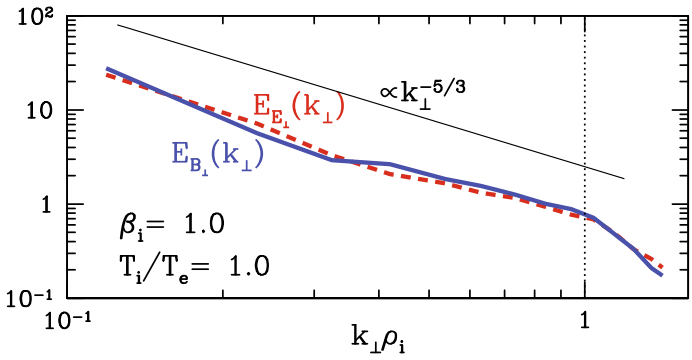

Fig. 5.8 Magnetic (solid line) and electric (dashed line) energy spectra in the MHD regime ($k_\perp \rho_i < 1$) given by the AstroGK simulation. The box size is $L_\perp = 2\pi 10\rho_i$. Electron hypercollisionality is dominant for $k_\perp \rho_i > 1$ denoted by dotted line (reprinted the figure with permission from Howes et al., Phys. Rev. Lett. 100, 065004, 2008a, copyright 2008 by the American Physical Society)

tions of magnetized turbulence in a homogeneous weak-collision plasma near the ion gyroscale (ρ_i). Figure 5.8 shows the normalized perpendicular magnetic (solid line) and electric (dashed line) energy spectra in the inertial range of $k_\perp \rho_i < 1$, where the plasma parameters $\beta_i = T_i/T_e = 1$ have been used. As expected by the Goldreich-Sridhar theory for critically balanced reduced AW turbulence in the inertial regime, these two spectra are nearly coincident and both show a scaling consistent with $\propto k_\perp^{-5/3}$. Moreover, this also, for the first time, demonstrated a MHD turbulence spectrum by a kinetic simulation and further confirmed the applicability of the AstroGK simulation.

From Fig. 5.8, a spectral break at the transition from AW to KAW turbulence can be clearly found at $k_\perp \rho_i \sim 1$. Figure 5.9 shows the perpendicular magnetic (bold solid line) and electric (bold dashed line) and parallel magnetic (bold dash-dotted line) energy spectra obtained by the AstroGK simulation around this transition (Howes et al. 2008a), where the corresponding energy spectra given by a turbulent cascade model based on the assumptions of the local nonlinear energy transfer, the critical balance between linear propagation and nonlinear interaction times, and applicability of linear dissipation rates are displayed in thin lines for comparison (Howes et al. 2008a). From Fig. 5.9, the energy spectra of kinetic turbulence given by the AstroGK simulation exhibited clearly that the evidently spectral break occurs at $k_\perp \rho_i \simeq 2$ and above this breaking point the magnetic and electric energy spectra become steepening ($\sim k_\perp^{-7/3}$) and flattening ($\sim k_\perp^{-1/3}$), respectively. Moreover, the turbulent energy spectra at scales below and above this transition are consistent with the predictions for critically balanced AW (Goldreich and Sridhar 1995) and KAW (Schekochihin et al. 2009) turbulent cascades (see Eq. 5.74), respectively.

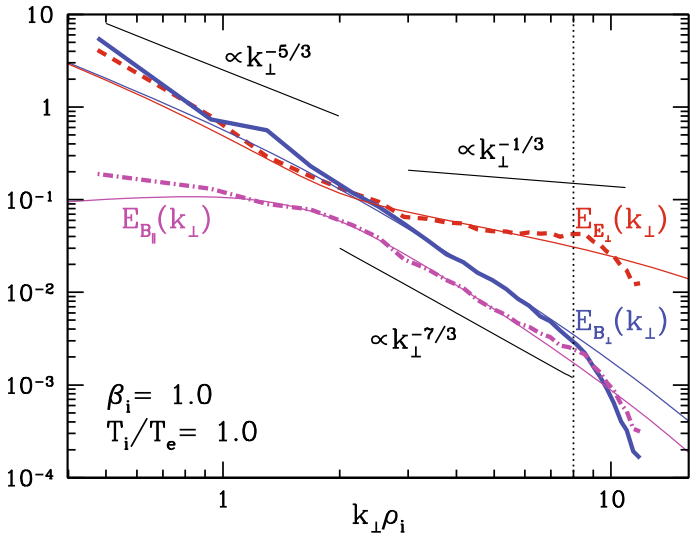

Fig. 5.9 Bold lines: normalized energy spectra for $\delta B_\perp$ (solid line), $\delta E_\perp$ (dashed line), and $\delta B_\parallel$ (dash-dotted line); Thin lines: solution of the turbulent cascade model (Howes et al. 2008b). Dimensions are $(N_x; N_y; N_z; N_\varepsilon; N_\xi; N_s) = (64; 64; 128; 8; 64; 2)$, requiring 5×10^9 computational mesh points, with box size $L_\perp = 5\pi\rho_i$. Electron hypercollisionality is dominant for $k_\perp\rho_i > 8$ denoted by dotted line (reprinted the figure with permission from Howes et al., Phys. Rev. Lett. 100, 065004, 2008a, copyright 2008 by the American Physical Society)

5.4.4 *AstroGK Simulations of Electron-Scale KAW Turbulence*

For the importance of the hypercollisionality involved in Howes et al. (2008a), the collision frequency ν_h has a marginal value for the ions, but a larger ν_h value is required for the electrons, implying that the hypercollisionality can not well model the electron heating in the electron gyroscale ρ_e. In order to extend the AstroGK simulation to the electron gyroscale range, Howes et al. (2011) focused the simulation concerning domain on the kinetic scales between the ion ($k_\perp\rho_i = 1$) and electron gyroradius ($k_\perp\rho_e = 1$), in which the nonlinear transferring of the turbulent energy at scales larger than the largest scales is modeled by six driving modes of parallel currents, $j_{z\mathbf{k}}$, with frequencies $\omega_0 = 1.14\omega_{A0}$ and wave vectors $(k_x\rho_i, k_y\rho_i, k_z L_z/2\pi) = (1, 0, \pm 1)$, $(0, 1, \pm 1)$, and $(-1, 0, \pm 1)$, where $\omega_{A0} \equiv k_{z0}v_A$. The driving amplitudes are determined by the critical balance condition at the largest scales and the energy is injected only at $k_\perp\rho_i = 1$ so that the amplitudes at all higher wave number $k_\perp\rho_i > 1$ can be attributed to the nonlinear turbulent cascade process. The simulation domain is anisotropic and has the sizes $L_\perp = 2\pi\rho_i \simeq 42.8\,(2\pi\rho_e) \ll L_z$ and the plasma parameters $\beta_i = 1$ and $\tau_0 = T_{i0}/T_{e0} = 1$ are used. In addition, a recursive expansion procedure is used to reach a statistically steady state at acceptable numerical calculation cost.

In particular, in order to prevent the non-physical small-scale velocity structures in the velocity space created numerically by wave-particle interactions due to exceeding the velocity space resolution from disturbing the physics of the kinetic damping (such as the Landau damping), they used the collision frequencies of $\nu_i = 0.04\omega_{A0}$ for ions and $\nu_e = 0.5\omega_{A0}$ for electrons, instead of the artificially enhanced hyper-collisionality, to erase these small-scale velocity structures. Thus, all dissipations come from resolved collisionless damping mechanisms and hence the steady state energy spectra at all scales, including the dissipative scales, are obtained by resolved physical processes. Therefore, the results may be more reliably compared directly to observational data.

Figure 5.10 presents the steady state energy spectra of the kinetic simulations (thick lines) for the perpendicular magnetic ($E_{B_\perp}(k_\perp)$, black solid), electric ($E_{E_\perp}(k_\perp)$, green dashed), and parallel magnetic ($E_{B_\parallel}(k_\perp)$, purple dot-dashed) field fluctuations in the kinetic scale range from the ion gyroscale extending to the electron gyroscale. From Fig. 5.10 the most salient feature of the magnetic and electric energy spectra is that they appear excellent power-law spectra over the entire scale range from the ion

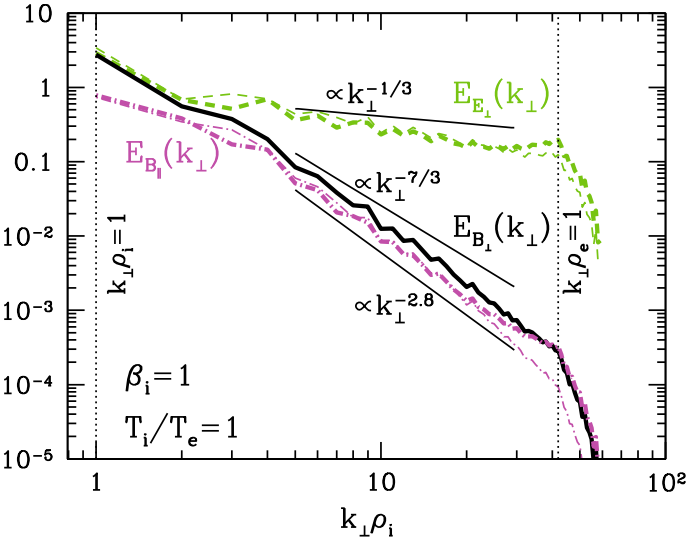

Fig. 5.10 The black thick solid, green thick dashed, and purple thick dot-dashed lines are the energy spectra of the kinetic turbulence for the perpendicular magnetic ($E_{B_\perp}(k_\perp)$), electric ($E_{E_\perp}(k_\perp)$), and parallel magnetic field fluctuations ($E_{B_\parallel}(k_\perp)$), which are given by the kinetic simulations. The green thin dashed and purple thin dot-dashed lines represent the perpendicular electric and parallel magnetic energy spectra predicted theoretically from the simulated perpendicular magnetic energy spectrum based on the polarization relations of the linear colissionless KAWs, which are excellent agreement with the simulation results. The two vertical thin dotted lines denote the positions of the ion and electron gyroradius (i.e., $k_\perp\rho_i$ and $k_\perp\rho_e$), respectively (reprinted the figure with permission from Howes et al., Phys. Rev. Lett. 107, 035004, 2011, copyright 2011 by the American Physical Society)

gyroscale at $k_\perp \rho_i = 1$ to the electron gyroscale at $k_\perp \rho_e = 1$. In general, the role of dissipations (due to collisions or collisionless kinetic damping) is removing the turbulent energy into the heating of plasma particles and a sufficiently strong dissipation at the ion gyroscale may lead to the turbulent cascade process terminating nearly the ion gyroscale. This results in that the turbulent energy spectra exhibit an exponential falloff at the ion gyroscale and can not reach the electron gyroscale (Podesta et al. 2010). However, observations of turbulent energy spectra at the kinetic scales in the solar wind (Bale et al. 2005; Alexandrova et al. 2009; Kiyani 2009; Sahraoui et al. 2009, 2010; Chen et al. 2010; Goldstein et al. 2015) show a continuation of the kinetic turbulent cascade until to the electron gyroscale that is well consistent with the AstroGK simulation results of the KAW turbulence presented in Fig. 5.10.

On the other hand, Fig. 5.10 also shows that the perpendicular electric (green thin dashed line) and parallel magnetic (purple thin dot-dashed line) energy spectra calculated directly by the perpendicular magnetic energy spectrum of the kinetic simulations based on the polarization relations of the linear colissionless KAWs both are excellent agreement with the corresponding simulation results. This indicates that the nature of the KAW turbulence is well consistent with the properties of linear KAWs although these turbulent KAWs are strongly nonlinear waves.

The effect of the Landau damping seems merely to steepen the energy spectra slightly, for instance, the magnetic energy spectrum is closer to $\propto k_\perp^{-2.8}$ rather than $\propto k_\perp^{-7/3}$ predicted by the theory of KAW turbulence without dissipation and the electric energy spectrum also is slightly steeper than the theoretically predicted spectrum $\propto k_\perp^{-1/3}$. One possible explanation for the turbulence energy spectra to extend to the electron gyroscale is that the nonlinear cascade process of the KAW turbulence can sufficiently fast transfer the energy into smaller scale waves before it is exhausted by the linear and nonlinear Landau damping if only these damping rates are lower than the linear wave frequency and hence slower than the nonlinear energy transferring rate. Observations of turbulent energy spectra at kinetic scales in the solar wind (Kiyani 2009; Alexandrova et al. 2009; Chen et al. 2010; Sahraoui et al. 2010) also show very well agreement with the slightly steepened energy spectra and further confirmed the effect of the Landau damping on the kinetic turbulent energy spectra.

Figure 5.11 shows the relative importance of various damping (or heating) processes, where panel (a) compares the nonlinear damping rate $\gamma_{nl} \sim Q_e/E_{B_\perp}$ (dashed line) to the nonlinear energy transferring frequency $\omega_{nl} \sim k_\perp v_\perp (\delta B_\perp/B_0)\sqrt{1+k_\perp^2\rho_i^2/2}$ (dotted line), panel (b) is the ion (solid line) and electron (dashed line) collisional heating rates normalized to the generalized energy (including both KAW and ion entropy cascades) transferring rate E, panel (c) presents the relative damping rates of the linear collisionless Landau damping for ions (solid line) and electrons (dashed line) in the gyrokinetic model, and two vertical dotted lines denote the positions of $k_\perp \rho_i = 1$ and $k_\perp \rho_e = 1$ (i.e., $k_\perp \rho_i = 42.8$), respectively. From Fig. 5.11a, the nonlinear energy transferring rate ω_{nl} does dominate the nonlinear damping rate γ_{nl} above the spectral breaking point at $k_\perp \rho_i \sim 1$ until $k_\perp \rho_i \sim 25$, as expected above. Comparing Fig. 5.11b and c, it can be found that there is an evident shift between the peak of the ion collisional heating rate (at the higher wave number $k_\perp \rho_i \sim 20$) and the

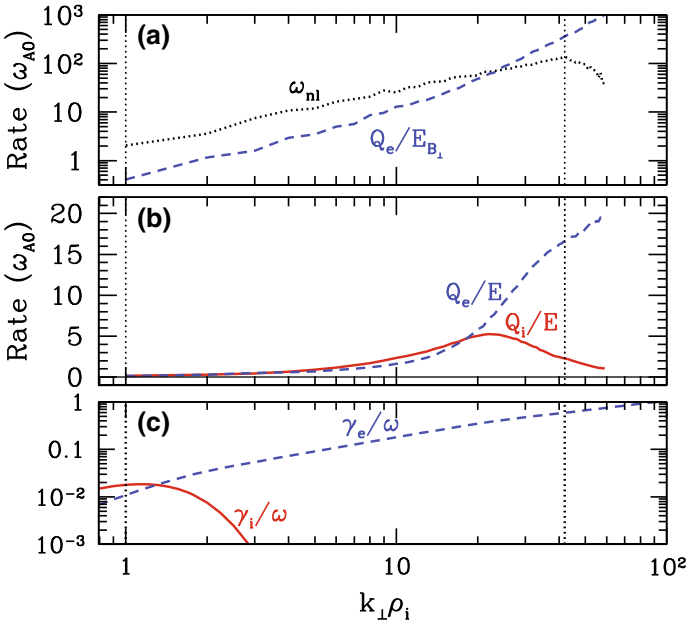

Fig. 5.11 **a** Nonlinear damping rate $Q_e/E_{B_\perp}$ and nonlinear energy transferring frequency ω_{nl}; **b** Ion (solid) and electron (dashed) collisional heating rate; **c** The linear ion (solid) and electron (dashed) Landau damping rates (reprinted the figure with permission from Howes et al., Phys. Rev. Lett. 107, 035004, 2011, copyright 2011 by the American Physical Society)

peak of the linear ion Landau damping rate (at the lower wave number $k_\perp\rho_i \sim 1$). This shift of the peak of ion collisional heating to higher wave number can be attributed to the effect of the ion entropy cascade because the ion entropy cascade can transfer energy to sub-ion gyroscales. Thus, this simulation results also provide the direct evidence of the ion entropy cascade in kinetic turbulence simulation.

In a gyrokinetic simulation covering wider scales from the tail of the MHD range to the electron gyroradius scale, Told et al. (2015) analyzed more in detail nonlinear energy transfer and dissipation in the transition from AW to KAW turbulence and further confirmed the multiscale nature of the dissipation range of the KAW turbulence. Their simulation results show that for typical solar wind parameters at 1 AU, about 30% of the nonlinear energy may be transferred by the nonlinear turbulent cascade process from the tail of the MHD inertial range to the electron gyroradius scale. Their results also indicate that the collisional dissipation could occur across the entire kinetic region and about 70% of the total dissipation is contributed from electron collisions, which exhibit a broad peak around $k_\perp\rho_i \sim 1$–5. On the other hand, the ion free energy can be cascaded to smaller scales and then is dissipated close to the electron gyroradius scale (around $k_\perp\rho_i \sim 25$). This phenomenon is possibly associated with the ion entropy cascade and the fact that $\nu_i \ll \nu_e$ (Tatsuno et al. 2009; Schekochihin et al. 2009; Howes et al. 2011).

5.4.5 *Kinetic PIC Simulations of KAW Turbulence*

In a three-dimensional particle-in-cell (PIC) simulation of plasma turbulence, resembling the plasma conditions found at kinetic scales of the solar wind, but using a reduced ion to electron mass ratio $m_i/m_e = 64$, Grošelj et al. (2018) also investigated the power spectra of electric and magnetic fluctuations and their ratios with focus on the kinetic region between $k_\perp \rho_i = 1$ and $k_\perp \rho_e = 1$. The simulation domain is a triply periodic box of size $L_\perp^2 \times L_z$ elongated along the mean magnetic field $\mathbf{B}_0 = B_0 \hat{\mathbf{z}}$, where $L_\perp = 16.97\lambda_i$, $L_z = 42.43\lambda_i$, and λ_i is the ion inertial length as usual. The initial fluctuations consist of counterpropagating AWs with different phases and wave numbers $(k_{\perp 0}, 0, \pm k_{z0})$, $(0, k_{\perp 0}, \pm k_{z0})$, and $(2k_{\perp 0}, 0, \pm k_{z0})$, where $k_{\perp 0} = 2\pi/L_\perp$ and $k_{z0} = 2\pi/L_z$. The initial turbulence amplitude is chosen such as to satisfy critical balance. Ions and electrons have an initial Maxwellian velocity distribution with equal isotropic temperature T_0 and uniform density n_0, and hence one has $v_{T_e} = 8v_{T_i} = 0.25c$, $\beta_i = 0.5$, $v_A = 2v_{T_i}$, and $\omega_{pe}/\omega_{ce} = 2.0$. Thus, the dimensionless plasma parameters and the physical setup resemble the plasma conditions inferred from solar wind measurements.

They performed the simulation using the PIC code OSIRIS (Fonseca et al. 2002, 2008) with the spatial resolution $(N_x, N_y, N_z) = (768, 768, 1536)$ and employing, on average, 74 particles per cell per species. Figure 5.12 shows the quasi-steady state power spectra of normalized magnetic (red solid line), electric (green dashed line), and density (blue dotted line) fluctuations in the kinetic region between $k_\perp \rho_i = 1$ and $k_\perp \rho_e = 1$, where the ion (electron) inertial length is denoted by $d_{i(e)}$, instead of λ_i as usual, and λ_D is the Debye length. Although well-defined power-law spectra can

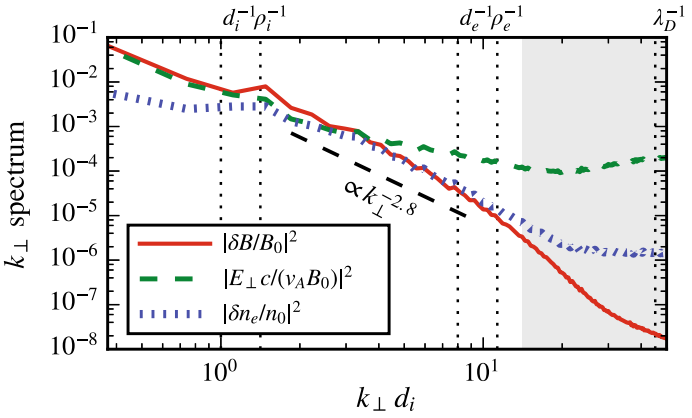

Fig. 5.12 One-dimensional $k_\perp$ spectra of magnetic, perpendicular electric, and density fluctuations at time $t_1 = 0.71t_A$, where $t_A = L_z/v_A$. The slope of -2.8 is shown for reference. Gray shading is used to indicate the range of scales dominated by particle noise (reprinted the figure with permission from Grošelj et al., Phys. Rev. Lett. 120, 105101, 2018, copyright 2018 by the American Physical Society)

not be established in the reduced kinetic region because of the limitations due to the reduced ion to electron mass ratio, the tendency of the energy spectral distribution still is relatively good agreement with a number of observations (Bale et al. 2005; Alexandrova et al. 2009; Sahraoui et al. 2010; Chen et al. 2013) as well as with the gyrokinetic simulations with the realistic ion to electron mass ratio (Howes et al. 2008a, 2011; TenBarge et al. 2013; Told et al. 2015). From Fig. 5.12, one can find that the electric field spectrum flattens in the kinetic range and separates from the magnetic energy, whereas the density spectrum converges toward a near equipartition with the magnetic spectrum in appropriately normalized units, which has features consistent with solar wind observations and the gyrokinetic simulations.

In particular, the near equipartition among density and magnetic fluctuations in the subion range is a key property of KAWs, differentiating from the weakly compressible whistler waves (i.e., $(|\delta n_e|/n_0)^2 \ll (|\delta B|/B_0)^2$; Gary and Smith 2009; Boldyrev et al. 2013; Chen et al. 2013). In the asymptotic limit of $\rho_i^{-1} \ll k_\perp \ll \rho_e^{-1}$ and $k_\parallel \ll k_\perp$, the analytical approximation of KAWs leads to Howes et al. (2006), Schekochihin et al. (2009), Gary and Smith (2009), Boldyrev et al. (2013):

$$\begin{aligned}
\frac{(|\delta n_e|/n_0)^2}{(|\delta B|/B_0)^2} &\sim \beta_i + 2\beta_i^2, \\
\frac{(|\delta n_e|/n_0)^2}{\left(|\delta B_\parallel|/B_0\right)^2} &\sim \frac{1}{\beta_i^2}, \\
\frac{|\delta B_\parallel|^2}{|\delta B|^2} &\sim \frac{\beta_i}{1+2\beta_i}, \\
\frac{|E_\perp^2|}{|\delta B_\perp|^2 v_A^2} &\sim \frac{k_\perp^2 \rho_i^2}{4+4\beta_i},
\end{aligned} \tag{5.75}$$

where the assumption $Z_i = T_i/T_e = 1$ has been used. Thus, for $\beta_i = 0.5$ the first expression leads to $(|\delta n_e|/n_0)^2 \sim (|\delta B|/B_0)^2$, as shown in Fig. 5.12. To further demonstrate the KAW nature of the measured fluctuations, Fig. 5.13 presents the turbulent spectral ratios in comparison with the above analytical predictions and all spectral ratios exhibit very good agreement between the PIC simulations and the theoretical predictions for KAWs.

Theoretical analyses (Howes et al. 2006; Schekochihin et al. 2009) and numerical simulations (Howes et al. 2008a, 2011; Grošelj et al. 2018) based on gyrokinetics and full kinetics showed that the KAW turbulence has two distinctive features. The one is that the linear physical characteristics in dispersion and polarization of KAWs still continue to exist in nonlinear turbulent KAWs, including their anisotropy of quasi-perpendicular propagation with $k_\perp \gg k_\parallel$ and their electric and magnetic polarized senses, such as $\delta E_\perp/\delta B_\perp$ and $\delta B_\parallel/\delta B_\perp$. The other one is that there are two evident transitions in the energy spectra of the KAW turbulence, which are located near at the wave numbers $k_\perp \rho_i = 1$ and $k_\perp \rho_e = 1$ and caused by the wave-number dependence of the linear Landau damping and the KAW dispersion. In physics, the Landau damping due to the wave-particle interactions for ions (near $k_\perp \rho_i = 1$) and electrons (near

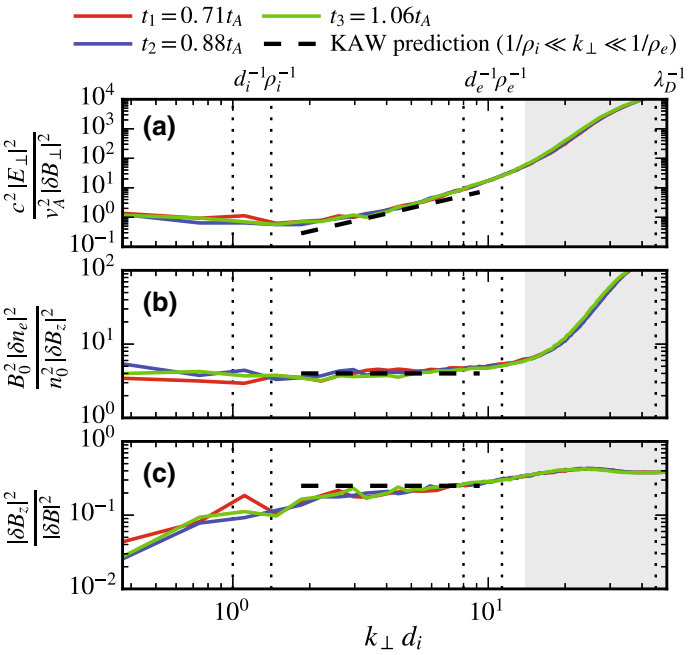

Fig. 5.13 The spectral ratios obtained from the PIC simulation: Solid lines correspond to three different times $t_1 = 0.71 t_A$, $t_2 = 0.88 t_A$, and $t_3 = 1.06 t_A$ and their good coincidence indicates a quasi-steady state. Dashed lines show the analytical predictions by Eq. (5.75) for KAWs (reprinted the figure with permission from Grošelj et al., Phys. Rev. Lett. 120, 105101, 2018, copyright 2018 by the American Physical Society)

$k_\perp \rho_e = 1$) leads to the KAW turbulent energy transferring directly into the resonant ions and electrons, respectively. On the other hand, the wave-number dependence of the KAW dispersion influences the transferring processes of the KAW turbulent energy from large to small kinetic scales. In particular, the KAW turbulence has a steeper energy spectrum $\propto k_\perp^{-7/3}$ (or $\propto k_\perp^{-8/3}$) in the kinetic region between $k_\perp \rho_i = 1$ and $k_\perp \rho_e = 1$, called the "kinetic inertial region", evidently different from the Kolmogorov spectrum $\propto k_\perp^{-5/3}$ in the MHD inertial range of $k_\perp \rho_i \ll 1$.

5.4.6 *Fluid-Like Simulations of KAW Turbulence*

Different from the gyrokinetic model of kinetic turbulence, which is valid only for the low-frequency regime of $\omega \ll \omega_{ci}$, Boldyrev et al. (2013) analyzed in detail linear modes of electromagnetic fluctuations nearly the ion gyrofrequency with special emphasis on the role and physical properties of KAWs and whistler waves. They found that KAWs exist in the low-frequency regime of $\omega \ll k_\perp v_{T_i}$ and whistler

waves occupy a different frequency regime of $k_\perp v_{T_i} \ll \omega \ll k_z v_{T_e}$. The corresponding kinetic damping rates can be given by

$$\frac{\gamma}{\omega_0} = -\sqrt{\frac{\pi}{2}} \frac{1+(1+\beta)^2}{(2+\beta)^{3/2}\,\beta^{1/2}} k_\perp \rho_e \tag{5.76}$$

for KAWs and

$$\frac{\gamma}{\omega_0} = -\sqrt{\frac{\pi}{2}} \frac{k_\perp}{k} k_\perp \rho_e - \frac{2\sqrt{\pi}|k_z|\lambda_i}{\beta_i^{3/2}} e^{-k_z^2\lambda_i^2/\beta_i} \tag{5.77}$$

for whistler waves, where $\beta = \beta_i + \beta_e$.

By use of fluid-like numerical simulations of strong KAW turbulence at subion gyroscales, based on the electron MHD equation including a driving force and small dissipation term, they also obtained similar steepened energy spectra $\propto k_\perp^{-8/3}$ for the magnetic and plasma density fluctuations of the KAW turbulence (Boldyrev and Perez 2012; Boldyrev et al. 2013). They proposed, however, that the nonlinear dynamics of KAWs has an important tendency to concentrate magnetic and density fluctuations in two-dimensional current sheet-like structures and this tendency leads to strong spatio-temporal intermittency in the field distributions. In particular, they thought that the energy spectrum steepening of the kinetic turbulence should be attributed mainly to the generation of the strong intermittency in the kinetic scales rather than the kinetic damping and the latter contributes only a small part to the spectrum steepening.

5.4.7 *Effects of Dispersion on KAW Turbulent Spectra*

Based on a phenomenalogical model of the KAW intermittency at kinetic scales, Zhao et al. (2016) further investigated the effect of the intermittency on the turbulent energy spectra of the KAW turbulence below and above the ion gyrofrequency. The generation of intermittent structures in turbulence indicates that the turbulent fluctuations occupy only a fraction of the phase-space volume (Matthaeus et al. 2015) and the occupying probability P_l is of scaling dependent in the form of $P(l) \propto l^{3-D}$, where D is the fractal dimension of the intermittent structures and is a fraction in general cases (Frisch 1995). For instance, one has $D = 0$, 1, and 2 and hence $P(k_\perp) \propto k_\perp^{-3}$, $k_\perp^{-2}$, and $k_\perp^{-1}$ for the ball-like, tube-like, and sheet-like structures, where $k_\perp \sim 2\pi/l$. As KAWs are elongated fluctuations along the local mean magnetic fields (i.e., $k_\perp \gg k_\parallel$), the isotropic ball-like structures can hardly develop. Thus a phenomenological scaling law can be given by $P(k_\perp) \propto k_\perp^{-\kappa}$ with a scaling index between 1 and 2 (i.e., $1 \le \kappa = 3 - D \le 2$) for the filling probability (or the occupying probability) of the intermittent structures of KAWs in the kinetic scales. In consequence, the steady-state energy spectra can be obtained by the combination of the scaling law of the filling probability dependent of the intermittent structures and

the critical balance condition dependent of the dispersion relation, and the resulting energy spectral index ranges between 7/3 and 3 (Zhao et al. 2016).

As noticed by Zhao et al. (2013), it is very evident that the linear dispersion relation can significantly influence the turbulent energy spectra in the kinetic scales because the critical balance condition and hence the scaling anisotropy both sensitively depend on the dispersion relation. In fact, from the dispersion relation of Eq. (1.20) for KAWs, a general scaling law for the anisotropy of the KAW turbulence can be obtained as follows (Zhao et al. 2013)

$$k_z = \frac{k_{z0}}{k_{\perp 0}^{2/3}} \frac{\left(1+\lambda_e^2 k_\perp^2\right)^{5/6}}{\left(1+\rho_{is}^2 k_\perp^2\right)^{1/6}} k_\perp^{2/3}, \tag{5.78}$$

where k_{z0} and $k_{\perp 0}$ are the driving parallel and perpendicular wave numbers. In the low-$k_\perp$ limit of both $\lambda_e k_\perp$ and $\rho_{is} k_\perp \ll 1$, the Goldreich-Sridhar anisotropic scaling law of $k_z \propto k_\perp^{2/3}$ is recovered. For the kinetic regime KAWs with $\rho_{is}^2 k_\perp^2 \gg 1 \gg \lambda_e^2 k_\perp^2$, the anisotropic scaling law of the KAW turbulence reduces to $k_z \propto k_\perp^{1/3}$ as shown in Eq. (5.73). While for the inertial regime KAWs with $\rho_{is}^2 k_\perp^2 \ll 1 \ll \lambda_e^2 k_\perp^2$ and the transition regime KAWs with $\rho_{is}^2 k_\perp^2 \sim \lambda_e^2 k_\perp^2 \gg 1$, the anisotropic scaling law of the KAW turbulence can read as $k_z \propto k_\perp^{7/3}$ and $k_z \propto k_\perp^2$, respectively, implying that field-aligned small-scale structures can develop faster than cross-field small-scale structures.

Correspondingly, the general steady-state energy spectra of the KAW turbulence with the general dispersion relation of Eq. (1.20) can be derived as follows (Zhao et al. 2013):

$$E_{B_\perp}(k_\perp) \propto \left(1+\lambda_e^2 k_\perp^2\right)^{-1/3} \left(1+\rho_{is}^2 k_\perp^2\right)^{-1/3} k_\perp^{-5/3} \tag{5.79}$$

for the perpendicular magnetic fluctuations,

$$E_{E_\perp}(k_\perp) \propto \left(1+\lambda_e^2 k_\perp^2\right)^{2/3} \left(1+\rho_{is}^2 k_\perp^2\right)^{-4/3} \left(1+\rho_i^2 k_\perp^2\right)^2 k_\perp^{-5/3} \tag{5.80}$$

for the perpendicular electric fluctuations, and

$$E_{E_z}(k_\perp) \propto \left[\alpha_e^2 - \left(1+\rho_i^2 k_\perp^2\right)\right]^2 \left(1+\lambda_e^2 k_\perp^2\right)^{1/3} \left(1+\rho_{is}^2 k_\perp^2\right)^{-5/3} k_\perp^{5/3} \tag{5.81}$$

for the parallel electric fluctuations.

In consideration of the dispersive effect, Voitenko et al. (2011) studied further the turbulent spectra and spectral pattern in the transition regime from the weakly to strongly dispersive KAWs based on the three-wave coupling dynamics (Voitenko 1998a, b). In the weakly dispersive regime of $k_\perp \rho_i < 1$, the nonlinear coupling rates are given by Voitenko (Voitenko 1998a, b)

$$\gamma_{\mathbf{k}}^{NL} \simeq 0.4 \omega_{ci} \frac{v_A}{v_{T_i}} \frac{\delta B_{\mathbf{k}}}{B_0} k_\perp^3 \rho_i^3 \tag{5.82}$$

for the interaction of co-propagating KAWs and

$$\gamma_{\mathbf{k}}^{NL} \simeq 0.3\omega_{ci}\frac{v_A}{v_{T_i}}\frac{\delta B_{\mathbf{k}}}{B_0}k_\perp^2\rho_i^2 \tag{5.83}$$

for the interaction of counter-propagating KAWs, which is larger than the coupling rate of co-propagating KAWs for weakly dispersive KAWs with $k_\perp\rho_i < 1$. On the other hand, in the strongly dispersive regime of $k_\perp\rho_i > 1$, the nonlinear coupling rates are (Voitenko 1998a, b)

$$\gamma_{\mathbf{k}}^{NL} \simeq 0.3\omega_{ci}\frac{v_A}{v_{T_i}}\frac{\delta B_{\mathbf{k}}}{B_0}k_\perp^2\rho_i^2 \tag{5.84}$$

for the interaction of co-propagating KAWs and

$$\gamma_{\mathbf{k}}^{NL} \simeq 0.2\omega_{ci}\frac{v_A}{v_{T_i}}\frac{\delta B_{\mathbf{k}}}{B_0}k_\perp^2\rho_i^2 \tag{5.85}$$

for the interaction of counter-propagating KAWs, which is close to the coupling rate of co-propagating KAWs. It is obvious that the nonlinear coupling rates of strongly dispersive KAWs are larger than that of weakly dispersive KAWs.

For sufficiently small perturbed amplitude and sufficiently high linear frequency, the turbulent cascade process can not reach the critical balance and the so-called weakly turbulent cascade process of $\gamma_{\mathbf{k}}^{NL} < \omega_{\mathbf{k}}$ can occur, in which the fluctuations have enough time to set up linear dispersion and polarization relations and conserve their dispersive energy, and hence the energy transferring rate among the fluctuations is relatively slow. Since the nonlinear coupling rate $\gamma_{\mathbf{k}}^{NL}$ is directly proportional to the relative amplitude of the fluctuations $\delta B_{\mathbf{k}}/B_0$, the strongly turbulent cascade process with the critical balance can realize for sufficiently large amplitude or sufficiently low linear frequency. For the weakly turbulent cascade, the turbulent energy spectrum can be estimated from the conservation law of the dispersive energy and the nonlinear coupling rate.

Motivated by the observed multi-kink pattern of kinetic turbulent spectra in the solar wind (Chen et al. 2010; Sahraoui et al. 2010), Voitenko et al. (2011) proposed that the entire energy spectrum from the nondispersive AW turbulence to the dispersive KAW turbulence can have two breaking points due to the variation of the dispersive property of KAWs. The first breaking point occurs at the transition region from the nondispersive AW turbulence to the weakly dispersive KAW turbulence and the second one presents at the transition region between the weakly dispersive KAW turbulence and the strongly dispersive KAW turbulence. Figure 5.14 depicts schematically the pattern of the double-kink energy spectrum. Taking account for possible effects of other dynamical phenomena on the turbulent cascade process, such as the dynamic alignment, the intermittent structure, the kinetic damping, and the turbulent intensity (i.e., the ratio of the nonlinear coupling rate to the linear frequency, $\gamma_{\mathbf{k}}^{NL}/\omega_{\mathbf{k}}$), the spectral indices of the weakly and strongly dispersive KAW

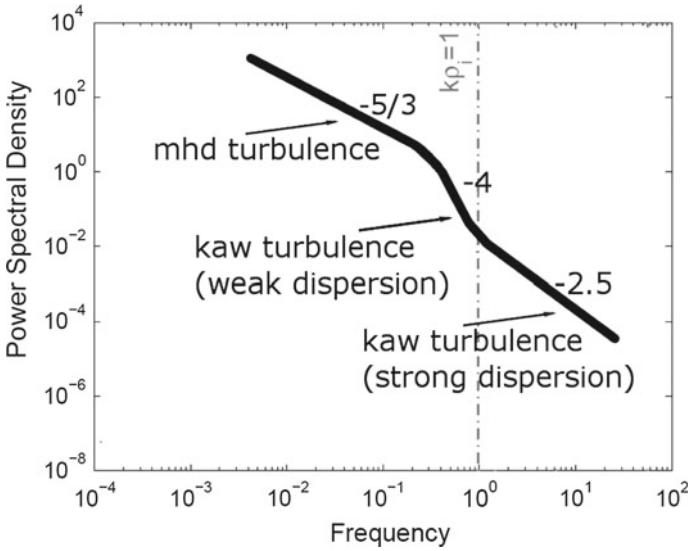

Fig. 5.14 A schematic depiction of the double-kink pattern turbulent spectrum from the nondispersive AW turbulence to weakly and strongly dispersive KAW turbulence. The spectral indices -4 and -2.5 of the weakly and strongly dispersive KAW turbulent spectra should be replaced by -3 and $-7/3$ for the strong turbulence (from Voitenko et al. 2011)

turbulence can range from -4 to -3 and from -2.5 to $-7/3$, respectively, dependent on the turbulent intensity.

5.5 Observational Identifications of KAW Turbulence

5.5.1 Initial Identifications of KAW Dispersion and Polarization

The solar wind, a supersonic and super-Alfvénic plasma flow originating from the solar high-temperature corona, develops a strong turbulence during its expanding through the whole heliosphere. The solar wind turbulence spreads a very wide range of scales from MHD scales larger than the size of the Sun to the kinetic scales of plasma particles, such as the ion gyroradius and the electron gyroradius. The dynamics of the solar wind turbulence in the MHD scale range is dominated by incompressible AWs (Coleman 1968; Tu and Marsch 1995) and well described by the Goldreich-Sridhar theory (Goldreich and Sridhar 1995, 1997), which predicts that the AW turbulence drives an energy cascade from large to small scales preferentially in the direction perpendicular to the ambient magnetic field, as shown

by simulations (Cho and Vishniac 2000; Maron and Goldreich 2001; Müller et al. 2003), so that the turbulence becomes progressively more anisotropic and the turbulent energy spectrum is concentrated in the wave-vector region of $k_\perp \gg k_\parallel$ as the energy cascade proceeds to higher wave numbers. Moreover, the observed anisotropy of solar wind turbulence in the MHD scales also exhibits an evident wave-number dependence consistent with the theoretical predictions (Horbury et al. 2008; Podesta 2009; Podesta et al. 2010; Wicks et al. 2010; Luo and Wu 2010; Luo et al. 2011; Forman et al. 2011). In consequence, when the energy cascade reaches the kinetic scales it is inevitable that the small-scale kinetic turbulence with $k_\perp \gg k_\parallel$ transfers naturally from the AW turbulence into the KAW turbulence. This implies that the KAW turbulence predominates the solar wind turbulence in the kinetic scales (Howes et al. 2008b; Boldyrev and Perez 2012; Podesta 2013).

In the kinetic scales, however, the dynamics of the KAW turbulence can become much more complicated than that of the MHD AW turbulence because intricate various factors, such as the linear dispersion and polarization relations (Zhao et al. 2013), the kinetic dissipation due to the Landau damping (Howes et al. 2008b, 2010), the dynamical alignment or the intermittency (Boldyrev 2005, 2006; Boldyrev and Perez 2012), and the coupling with other mode waves (Gary and Smith 2009; Mithaiwala et al. 2012; Boldyrev et al. 2013; López 2017; Cerri et al. 2017), interweave each other and influence the dynamics of the KAW turbulence in the kinetic scales. For instance, recent results based on the gyrokinetic simulations (Howes et al. 2011; Told et al. 2015) and the nonlinear wave-wave coupling (Voitenko et al. 2011) show that the turbulent energy spectrum from the MHD to kinetic scales and from the ion to electron gyroradius exhibits the multi-breaking feature. In this section, we present recent observations of the solar wind turbulence in the kinetic scales and discuss their physical nature of KAWs.

Theoretical analyses and numerical simulations in Sect. 5.4 showed that the KAW turbulence has two distinctive features. The one is that the linear physical characteristics in dispersion and polarization of KAWs still continue to have in nonlinear turbulent KAWs, including their anisotropy of quasi-perpendicular propagation with $k_\perp \gg k_\parallel$ and their electric and magnetic polarized senses, such as $\delta E_\perp/\delta B_\perp$ and $\delta B_\parallel/\delta B_\perp$. The other one is that there are two evident transitions in the energy spectra of the KAW turbulence, which are located near at the wave numbers $k_\perp\rho_i = 1$ and $k_\perp\rho_e = 1$ and caused by the wave-number dependence of the linear Landau damping and the KAW dispersion. In physics, the Landau damping due to the wave-particle interactions for ions and electrons leads to the KAW turbulent energy transferring directly into the resonant ions and electrons, respectively, and the dispersion influences the transferring of the KAW turbulent energy from large to small kinetic scales. In particular, the KAW turbulence has a steeper energy spectrum $\propto k_\perp^{-7/3}$ (or $\propto k_\perp^{-8/3}$) in the kinetic inertial region between $k_\perp\rho_i = 1$ and $k_\perp\rho_e = 1$, evidently different from the Kolmogorov spectrum $\propto k_\perp^{-5/3}$ in the MHD inertial range of $k_\perp\rho_i \ll 1$.

The first attempt of measuring the dispersion and polarization of solar turbulent fluctuations in the kinetic scales was made by Bale et al. (2005). Based on the data measured in situ by the four Cluster satellites during the interval 00:07:00−03:21:51 UT (∼195 min) on 19 February 2002, when the Cluster was

near the apogee ($\sim 19 R_E$) of its inclined orbit and spent several hours in the ambient solar wind, Bale et al. (2005) calculated the power, the phase velocity and the polarization of the electric and magnetic field fluctuations as well as their spectral density over the MHD inertial and kinetic dissipative wave number ranges. In order to strengthen the reliability of the calculation results they computed the power spectral density using both the Morlet wavelet and fast Fourier transform (FFT) schemes (Torrence and Compo 1998) and restricted their interpretation to the region where the two results agree.

Figure 5.15 shows their calculation results, where the panel (a) presents the power spectral densities of electric (green) and magnetic (black) field fluctuations computed using the wavelet (upper) and fast Fourier transform (lower) schemes. From the panel (a) of Fig. 5.15, the turbulent energy spectra of electric and magnetic fluctuations

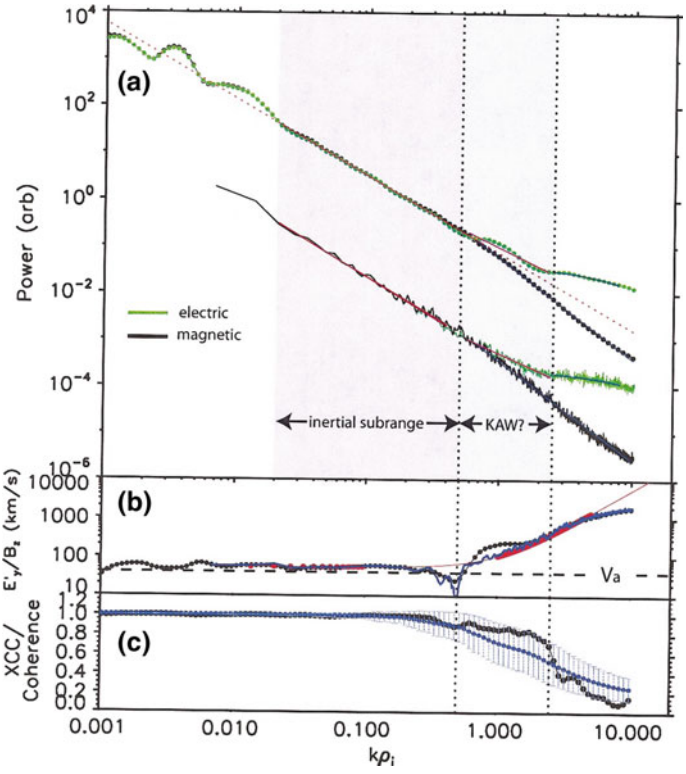

Fig. 5.15 Panel **a** shows the wavelet (upper) and FFT (lower) power spectra of E_y (green) and B_z (black) versus the normalized wave number $k\rho_i$; Panel **b** shows the ratio of the electric to magnetic spectra in the plasma frame, where the average Alfvén speed ($v_A \simeq 40$ km/s) is shown by a horizontal line and the red line is a fitted curve by the KAW linear polarization relation; Panel **c** shows both the cross coherence of E_y with B_z by blue dots with error bars and the correlation between the electric and magnetic power by black dots (reprinted the figure with permission from Bale et al., Phys. Rev. Lett. 94, 215002, 2005, copyright 2005 by the American Physical Society)

agree strikingly each other in the inertial subrange between $k\rho_i \simeq 0.015$ and 0.45 and both show power law behavior with indices of -1.7, which is consistent with the Kolmogorov spectrum of $\propto k^{-5/3}$, as expected by the Goldreich-Sridhar AW turbulence theory, where the wave number is determined by the so-called Taylor hypothesis (Taylor 1938), that is, the Doppler drift, $k = \omega/v_{sw}$, and v_{sw} is the local solar wind velocity much larger than the average Alfvén velocity v_A. At $k\rho_i \simeq 0.45$ the electric and magnetic energy spectra both show evident break and then they start to separate obviously due to the kinetic dispersion effects of KAWs, in which the electric spectrum becomes a flattened power law spectrum with an index of -1.26 and the magnetic spectrum becomes steeper with an index of -2.12.

The panel (b) in Fig. 5.15 shows the ratio of the electric to magnetic fluctuations in the plasma frame, $\delta E'_y/\delta B_z$ (the subscripts y and z denote the y and z components in the GSE (geocentric solar ecliptic) coordinate system, where the black dots and blue line are computed from the wavelet and FFT spectrum, respectively, and well agree. The horizontal line denotes the average Alfvén velocity $v_A \simeq 40$ km/s and the red line is a fitted curve by the KAW polarization relation in the panel (b). It can be found that the wavelet (the black dots) and FFT (the blue line) ratios of electric to magnetic fluctuations nearly coincide and are well consistent with the average Alfvén velocity $v_A \simeq 40$ km/s in the inertial subrange $0.015 < k\rho_i < 0.45$ and in the higher wave number range of $0.5 < k\rho_i < 5$ the FFT ratio also can be well with the fitted curve by the KAW polarization relation. The panel (c) shows both the cross coherence of the electric with magnetic fluctuations (blue dots with error bars) and the correlation between their power spectra (black dots). It is clear that the fluctuations are strongly correlated through the inertial range (with coefficient $\simeq 1$), remain well correlated in the kinetic range between the two breaking points $0.45 < k\rho_i < 2.5$, and begin to lose correlation quickly above the second breaking point at $k\rho_i \simeq 2.5$.

In this analysis, they also compared the observed dispersion to that the prediction of the whistler mode and found that the prediction of the whistler mode is much shallower than the observed dispersion at the kinetic region of $k\rho_i \sim 1$. This strongly suggested the physical nature of KAWs for the observed turbulent fluctuations and indicated that as the turbulent cascade proceeds towards smaller and smaller scales, the AW turbulence in the inertial subrange of $k\rho_i \ll 1$ progressively transfers into the KAW turbulence at $k\rho_i \sim 1$, becoming more electrostatic and eventually damping on the thermal plasma at higher wave numbers of $k\rho_i \gg 1$. In spite of the similar evidence for the KAW nature of solar wind turbulence at the kinetic scales further was confirmed later in other observations (Sahraoui et al. 2009; Kiyani 2009; Alexandrova et al. 2009), there has been a strong debate about the actual nature of the kinetic turbulence in the solar wind, that is, whether or not it is KAW (Bale et al. 2005; Sahraoui et al. 2009) or whistler wave (Gary and Smith 2009; Podesta et al. 2010) turbulence.

5.5.2 *Refined Identifications of KAW Dispersion and Spectra*

Sahraoui et al. (2010) considered that the difficulty in addressing this problem unambiguously stems from the lack of direct measurements of three-dimensional dispersion relations at the kinetic scales. Indeed, nearly all previous research has used additional assumptions, such as the Taylor frozen-in-flow approximation (i.e., the Taylor hypothesis, Taylor 1938), to infer the spatial properties of the turbulence from the measured temporal ones. The Taylor approximation is valid only if all fluctuation phase velocities are smaller than the solar wind flow velocity v_{sw}, and more importantly, it provides only the wave number spectrum in the direction parallel to the flow $\mathbf{v}_{sw}$. The absence of information on the two other directions prevents a full estimation of the dispersion relations, which compromises the chance of identifying unambiguously the nature of kinetic turbulence.

Using the k-filtering technique (Pincon 1995) on the Cluster multi-satellite data on 10 January 2004 from 06:05 to 06:55 UT, Sahraoui et al. (2010) measured the wave number $\mathbf{k}$ of solar wind fluctuations in the kinetic scales and analyzed the three-dimensional dispersion relation as well as the magnetic energy spectra. This time interval was selected because it has simultaneously several advantages suitable for the measurements of the three-dimensional wave number $\mathbf{k}$ of turbulent fluctuations at the kinetic scales by using the k-filtering technique: (i) The four satellites were located in the solar wind without connection to electron foreshock to avoid as much as possible sharp gradients in the magnetic field components; (ii) Burst mode data (with a sampling 450 Hz) were available, which allows examination of high frequency turbulence; (iii) The magnetic fluctuations had high amplitudes relative to the sensitivity floor of the Cluster search-coil magnetometer; (iv) The Cluster satellites formed a regular tetrahedron configuration, which is a necessary condition for appropriate k-spectra determination; (v) The small separation among the Cluster satellites (by ~ 200 km) is appropriate for exploring subproton scales.

They selected four time periods ($06:06-06:10$; $06:15-06:25$; $06:27-06:41$; $06:50-06:55$, see Table 1 of Sahraoui et al. (2010) for the average plasma parameters during them) and measured the full wave vectors $\mathbf{k}$ for each satellite-frame frequency f_{sc} between 0.04 and 2 Hz by applying the k-filtering technique. Figure 5.16 presents the angles between the measured wave vectors $\mathbf{k}$ and the mean magnetic field $\mathbf{B}_0$ (θ_{kB}) and the solar wind flow $\mathbf{v}_{sw}$ (θ_{kv}). For the selected four time intervals, $06:06-06:10$, $06:15-06:25$, $06:27-06:41$, and $06:50-06:55$, they obtained the propagation angles, on average, $\langle\theta_{kB}\rangle = 86^\circ \pm 6^\circ, 91^\circ \pm 6^\circ, 87^\circ \pm 4^\circ$, and $90^\circ \pm 7^\circ$, respectively. This clearly demonstrated the strongly anisotropic ($k_\perp \gg k_\parallel$) and the quasi-perpendicular propagating ($\theta_{kB} \simeq 90^\circ$) characteristics of the observed turbulent fluctuations at the kinetic scales, which are well consistent with the physical nature of KAWs.

On the other hand, the results in Fig. 5.16 also show that the wave vectors have moderate and relative spread alignment angles, on average, $\langle\theta_{kv}\rangle = 37^\circ \pm 09^\circ, 31^\circ \pm 08^\circ, 14^\circ \pm 10^\circ$, and $37^\circ \pm 11^\circ$ for the four intervals, respectively. Besides the third interval (denoted in red) shows a quasi-alignment (i.e., $\langle\theta_{kv}\rangle = 14^\circ \pm 11^\circ$ with the

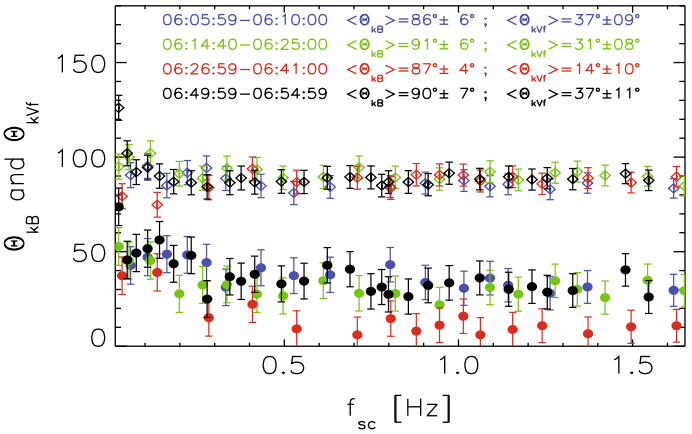

Fig. 5.16 Angles θ_{kB} (diamonds) and θ_{kv} (dots) with related error bars as estimated by using the k-filtering technique (reprinted the figure with permission from Sahraoui et al., Phys. Rev. Lett. 105, 131101, 2010, copyright 2010 by the American Physical Society)

solar wind flow, the finite alignment angles $\langle\theta_{kv}\rangle \sim 40°$ of the wave vectors $\mathbf{k}$ with respect to the solar wind flow $\mathbf{v}_{sw}$ during the other three intervals indicate that the observed turbulent fluctuations are not frozen in the solar wind flows and propagate at the wave vectors of departure from the flows by a finite angle. This breaks down the Taylor frozen-in-flow condition and hence could lead to significant distortions in the k-spectra if they were calculated by using the Taylor approximation.

On the other hand, using the measured wave vector $\mathbf{k}$, the wave frequency in the plasma frame can be given by the satellite-frame frequency and the Doppler frequency shift as follows:

$$\omega = 2\pi f_{sc} - \mathbf{k}\cdot\mathbf{v}_{sw} = 2\pi f_{sc} - kv_{sw}cos\theta_{kv}. \tag{5.86}$$

Figure 5.17 displays the measured dispersion relations compared to the theoretical predictions based on the Vlasov-Maxwellian equations for KAWs (the blue lines) and fast magnetosonic (i.e., whistler) waves (the red lines) at three quasi-perpendicular propagation angles $\theta_{kB} = 85°$, 87°, and 89°. It is very clear and evident from the displayed results in Fig. 5.17 that the measured turbulent fluctuations cascade and propagate following the dispersion relations of the KAW mode but far from those of the fast magnetosonic (or i.e., whistler) mode in the typical kinetic scale range from 0.04 to 2 $k_\perp\rho_i$, covering both the transition and the Kolmogorov inertial regions. This directly demonstrates based on the measured dispersion relation that the observed turbulent fluctuations in the kinetic scales have the physical nature of KAWs, rather than that of whistler waves.

In addition, also Fig. 5.17 shows clearly that the measured wave frequencies remarkably depart from both the proton cyclotron and electron Landau resonant frequencies, but are close to the proton Landau resonant frequency. This indicates

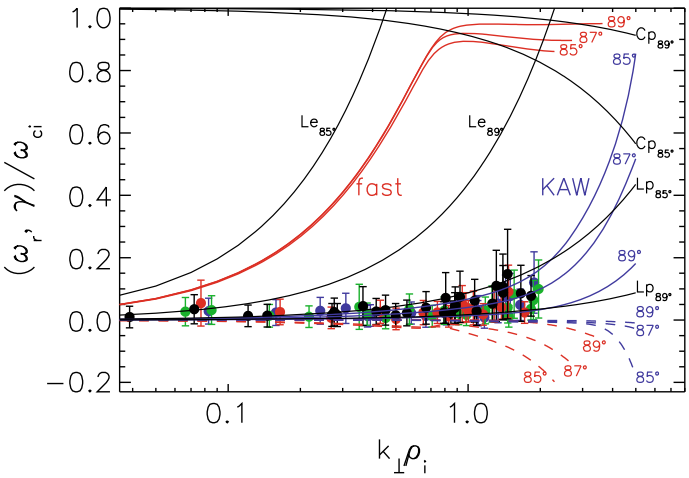

Fig. 5.17 Measured dispersion relations (dots), with estimated error bars, compared to linear solutions of the Maxwell-Vlasov equations for KAWs (the blue lines) and fast magnetosonic (i.e., whistler) waves (the red lines) at three propagation angles $\theta_{kB} = 85°$, 87°, and 89°, where the corresponding dashed lines are their damping rates. The black curves ($L_{p(e)}$) are the proton (electron) Landau resonant frequency $\omega = k_\parallel v_{T_{i(e)}}$, and the curves C_p are the proton cyclotron resonant frequency $\omega = \omega_{ci} - k_\parallel v_{T_i}$ (reprinted the figure with permission from Sahraoui et al., Phys. Rev. Lett. 105, 131101, 2010, copyright 2010 by the American Physical Society)

that the proton Landau damping dominates over the electron Landau and proton cyclotron dampings. An immediate consequence of these results is that the damping of turbulence and heating of the protons will arise most likely by the Landau damping and not cyclotron resonances.

In general, for KAWs one has the solar wind flow velocity v_{sw} much larger than the phase velocity ω/k and hence has $f_{sc} \simeq k v_{sw} cos\theta_{kv}/2\pi$ from the frequency transform relation between the plasma-frame frequency (ω) and the satellite-frame frequency $\omega_{sc} = 2\pi f_{sc}$ given by Eq. (5.86). This indicates that the Taylor hypothesis is usually valid for KAWs, that is, KAW fluctuations are approximately "frozen into" the solar wind flow ($\mathbf{v}_{sw}$). Thus, the measured power spectra in the satellite-frame frequency f_{sc} may be interpreted directly as reduced wave number k spectra.

Sahraoui et al. (2010) also calculated the perpendicular and parallel magnetic power spectra of the observed turbulent fluctuations in the satellite-frame frequency f_{sc}. Figure 5.18 shows the results for the interval of 06 : 14 : 40 − 06 : 25 : 00, which are similar to those computed from the other three time intervals, where the parallel (the black line) and perpendicular (the red line) magnetic fluctuations were measured by the flux gate magnetometer for the low-frequency part ($f < 2$ Hz) and by the search-coil magnetometer for the high-frequency part ($f > 2$ Hz) in order to avoid hitting the noise floors of the flux gate magnetometer in the high-frequency part and the search-coil magnetometer in the low-frequency part, and the black dotted line is the in-flight sensitivity floor of the search-coil magnetometer.

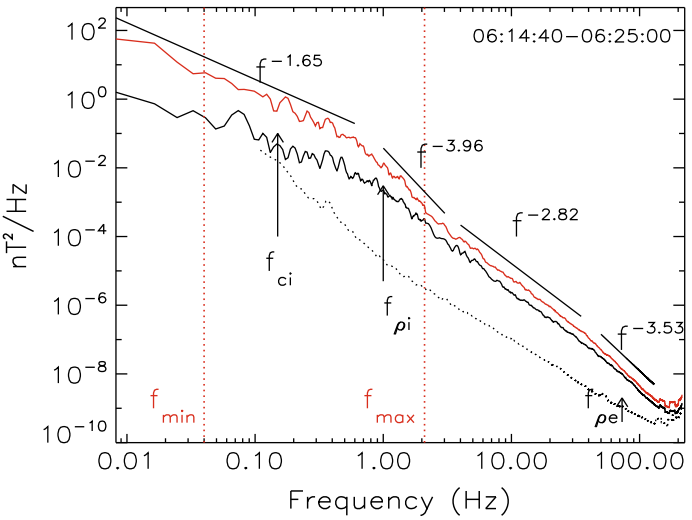

Fig. 5.18 Perpendicular (red curve) and parallel (black curve) magnetic power spectra, where the vertical arrows are the proton gyrofrequency f_{ci} and the "Doppler-shifted" proton (electron) gyroradius ($f_{\rho_{i(e)}} = v_{sw}/2\pi\rho_{i(e)}$) and the vertical dotted lines delimit the interval between f_{min} and f_{max} accessible to analysis by using the k-filtering technique (reprinted the figure with permission from Sahraoui et al., Phys. Rev. Lett. 105, 131101, 2010, copyright 2010 by the American Physical Society)

These spectra presented in Fig. 5.18 show very similar features to those observed by Sahraoui et al. (2009) and Alexandrova et al. (2009), that is, a Kolmogorov scaling law $\propto f^{-1.7}$ in the MHD inertial range of large scales, a breakpoint around the proton gyroscale ($\sim f_{\rho_i}$) (rather than the proton gyrofrequency f_{ci}), a steeper power law spectrum $\propto f^{-2.8}$ in the kinetic inertial range of subproton scales, and then a second breakpoint followed by a steepening around the electron gyroscale ($\sim f_{\rho_e}$, close to the electron inertial length λ_e for $\beta_e = 1$). By comparing these observed spectra with those predicted by the AstroGK simulations for the KAWs turbulence, as shown in Figs. 5.8, 5.9, and 5.10, one can find the striking agreement between the observed and predicted spectra. This strongly proposed that the physical nature of the observed turbulent fluctuations in the kinetic scales is the KAW mode.

Meanwhile, by a careful investigation of these spectra it can be found that the spectra actually steepen more strongly to $\propto f^{-4}$ around the first breakpoint at the proton gyroscale between $f_{sc} \sim 1$–3 Hz, where a transition to subion dispersive cascade occurs. As shown in Fig. 5.14, this stronger steepening can be attributed to the enhanced dissipation at the ion gyroscale (Voitenko et al. 2011), in which the turbulent energy is linearly or nonlinearly damped into protons, while the remaining energy undergoes a dispersive cascade towards smaller scales where it may be dissipated into electron heating.

5.5.3 Identifications of KAW Magnetic Compressibility

From Fig. 5.18, in addition, by comparing the parallel and perpendicular magnetic power spectra one can find that the parallel to perpendicular magnetic power spectral ratio increases as the frequency f (i.e., the wave number k) increases. This is consistent with the another important characteristic of KAWs, that is, the magnetic compressibility of KAWs increases with the wave number. Gary and Smith (2009) and Chen and Wu (2011b) analyzed the dependency of the magnetic compressibility parameter,

$$C_{\parallel}(\mathbf{k}) \equiv \frac{|\delta B_{\parallel}(\mathbf{k})|^2}{|\delta \mathbf{B}(\mathbf{k})|^2}, \tag{5.87}$$

on the wave number $\mathbf{k}$ and on the plasma β for different mode waves. The results show that the wave-number dependency of the magnetic compressibility for KAWs is distinctly different from that for whistler waves. In the inertial region of $k_{\perp}\lambda_i \ll 1$ the magnetic compressibility of AWs $C_{\parallel A}(\mathbf{k}) \to 0$ because of the incompressibility of AWs, and in the kinetic region of $k_{\perp}\lambda_i \sim 1$, KAWs have a magnetic compressibility, $C_{\parallel K}(\mathbf{k})$, much smaller than that of whistler waves, $C_{\parallel W}(\mathbf{k})$, that is, $C_{\parallel K}(\mathbf{k}) \ll C_{\parallel W}(\mathbf{k})$. As the perpendicular wave number $k_{\perp}\lambda_i$ increases, however, $C_{\parallel K}(\mathbf{k})$ increases evidently as shown by the middle panel of Fig. 1.3 which is obtained from Eq. (1.30), while $C_{\parallel W}(\mathbf{k})$ is approximately invariable, where the ion inertial length $\lambda_i \sim \rho_i$ for a high-β plasma with $\beta \sim 1$ such as in the solar wind. On the other hand, for a fixed wave number $k_{\perp} \gg k_{\parallel}$, the magnetic compressibility, $C_{\parallel}(\beta)$, is an increasing function of β (or i.e., α_e) for KAWs as shown in the middle panel of Fig. (1.4) given by Eq. (1.30). On the other hand, for whistler waves the magnetic compressibility $C_{\parallel}(\beta)$ nearly is a constant function of β in the kinetic region of $k_{\perp}\rho_i \sim 1$, where $\beta = \beta_i + \beta_e$. Thus, the measurement of the magnetic compressibility of the fluctuations can be used as the distinction between the two models, KAWs or whistler waves (Gary and Smith 2009).

In the observational aspect, based on a database of ACE observations at 1 AU, which was constructed by Hamilton et al. (2008) and consists of 960 intervals spanning the broadest possible range of solar wind conditions including magnetic clouds, Hamilton et al. (2008) analyzed the correlation between the anisotropy of magnetic fluctuations and β_p. Their result indicates that, on average, the magnetic compressibility $C_{\parallel}$ increases with β_p in the range of kinetic scales and that the average tendency of the solar wind fluctuations in the kinetic scales is consistent with the behavior of KAWs and inconsistent with that of quasi-perpendicular magnetosonic or whistler waves. However, a mixture of KAWs and whistler waves can not be ruled out and hence the conclusion is not conclusive one or the other. Therefore, in general, it is of more interest to compare theoretical predictions directly with solar wind observations by plotting the two modes both on the same graph so that quantitative contrasts between them may be made.

Salem et al. (2012) further investigated the physical nature of small-scale turbulent fluctuations in the solar wind using the comparison between the measured magnetic

compressibility of fluctuations to the theoretical predictions arising from the models consisting of either KAWs or whistler waves. The data of solar wind fluctuations is from the observation by the Cluster satellite during the interval 03:00:00−04:42:00 UT on 30 January 2003 when the Cluster was travelling in the solar wind. Through the Lorentz transformation, Salem et al. (2012) transform the magnetic compressibility predicted theoretically by the linear modes from the plasma frame into the satellite frame, $\left(|\delta B_\parallel|/|\delta \mathbf{B}_\perp|\right)_{sc}$, so that it may be compared directly to the observational data in situ measured in the satellite frame.

Figure 5.19 presents the predicted magnetic field fluctuation transformed to the satellite frame to predict signature of $|\delta B_\parallel/\delta \mathbf{B}|_{sc}$ for the two wave modes, whistler waves (black/blue) and KAWs (red) with different angles as shown in the figure, where the satellite-frame frequency of the fluctuations f is calculated by $2\pi f = \omega + \mathbf{k}\cdot\mathbf{v}_{sw}$, accounting for the Doppler shift arising from the relative velocity $\mathbf{v}_{sw}$ between the solar wind plasma frame and the satellite frame for a single plane wave with wave vector $\mathbf{k}$ and frequency ω. The frequency $f_b \simeq 0.4$ Hz corresponds the breaking frequency of the power spectrum at the transition between the inertial and dissipative region (Salem et al. 2012). The measured ratio of the parallel to total magnetic fluctuations in the Cluster data, $\delta B_\parallel/\delta B$, is given by the green curve.

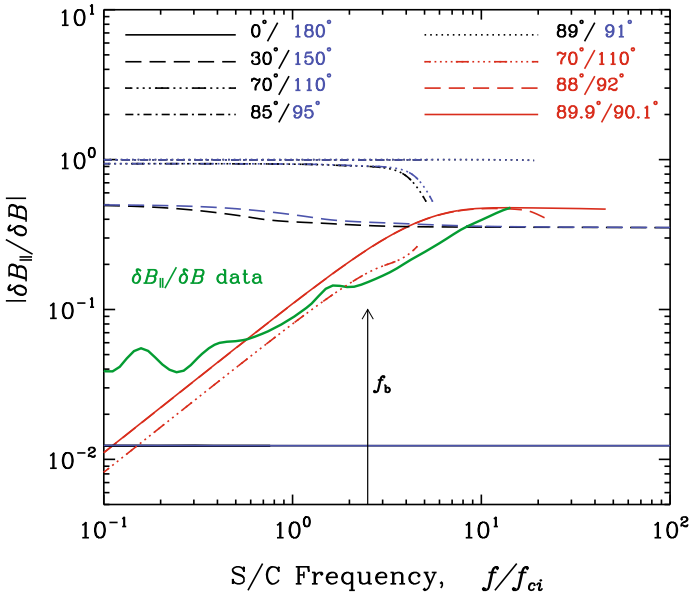

Fig. 5.19 Prediction of $|\delta B_\parallel/\delta \mathbf{B}|_{sc}$ for KAWs (red) or whistler waves (black/blue) with specified angle θ. Cluster flux gate magnetometer measurements up to 2 Hz, or 12 f_{ci}, are shown in green. (from Salem et al. 2012, ©AAS reproduced with permission)

From Fig. 5.19, it is very clear that the measured parallel to total magnetic fluctuation ratio is inconsistent with the predictions by the whistler wave for any angle of the wave vector, but is remarkably good agreement with the prediction for the KAW with a nearly perpendicular wave vector.

Another parameter related to the magnetic compressibility, the magnetic anisotropic ratio of fluctuations (i.e., the ratio of the parallel to perpendicular magnetic fluctuations),

$$\frac{\left(\delta B_{\parallel}\right)^2}{\left(\delta B_{\perp}\right)^2} = \frac{C_{\parallel}}{1 - C_{\parallel}}, \tag{5.88}$$

also has been used often as a method to identify the physical nature of solar wind turbulent fluctuations near the particle kinetic scales (such as the proton gyroscale $k_{\perp}\rho_p \sim 1$). In particular, the wave-number dependence of the magnetic anisotropic ratio of KAWs, $\left(\delta B_{\parallel}\right)^2 / \left(\delta B_{\perp}\right)^2$, has a distinctive feature in the solar wind plasmas with $\beta \sim 1$, that is, the ratio approaches zero in the small wave number limit of $k_{\perp}\rho_p \ll 1$ and increases monotonically to values of order unity when $k_{\perp}\rho_p \sim 1$ (Hollweg 1999; Gary and Smith 2009; TenBarge et al. 2012; Podesta and TenBarge 2012).

Podesta and TenBarge (2012) analyzed 20 high-speed solar wind streams observed by the dual STEREO satellites (denoted by "A" and "B", Acuña et al. 2008) in the ecliptic plane near 1 AU from 2007 through 2011 (see Table 1 of Podesta and TenBarge 2012). In order to facilitate the measurements of the ratio, $\left(\delta B_{\parallel}\right)^2 / \left(\delta B_{\perp}\right)^2$, and their comparisons to theory, these streams have been selected during times when the local mean magnetic field $\mathbf{B}_0$ is nearly perpendicular to the local flow velocity of the solar wind $\mathbf{v}_{sw}$. Thus, the quantities $\left(\delta B_{\parallel}\right)^2$ and $\left(\delta B_{\perp}\right)^2$ can be measured simply by the average magnetic powers in the $\mathbf{B}_0$ and $\mathbf{v}_{sw} \times \mathbf{B}_0$ directions, respectively.

Figure 5.20 shows a sample of them, which data are from the STEREO-A satellite for the time interval 27 July 2011, 12:00 to 30 July 18:00, 3.25 days, when $v_{sw} \simeq 621$ km/s and $\beta_i \simeq 0.7$. From Fig. 5.20, it can be found that the solar wind measurements (open circles) and the predictions based the Vlasov-Maxwell theory of KAWs (red curve) are good agreement for the high wave number of $k_{\perp}\rho_p > 1$ and both exhibit a monotonic and smooth increase at $k_{\perp}\rho_p \sim 1$ as expected theoretically. Based on the analysis by Podesta and TenBarge (2012), these 20 high-speed solar wind streams observed by the STEREO consistently yield quantitatively similar results that all show a steady increase in the magnetic anisotropic ratio, $\left(\delta B_{\parallel}\right)^2 / \left(\delta B_{\perp}\right)^2$, in the neighborhood of $k_{\perp}\rho_p \sim 1$ and are in reasonable agreement with the prediction of KAWs derived from the Vlasov-Maxwell dispersion relation. Therefore, these results can be well interpreted as evidence for the existence of quasi-perpendicular KAWs with $k_{\perp} \gg k_{\parallel}$ in the fast solar wind at the kinetic scale range near $k_{\perp}\rho_p \sim 1$, where the kinetic physics becomes more important.

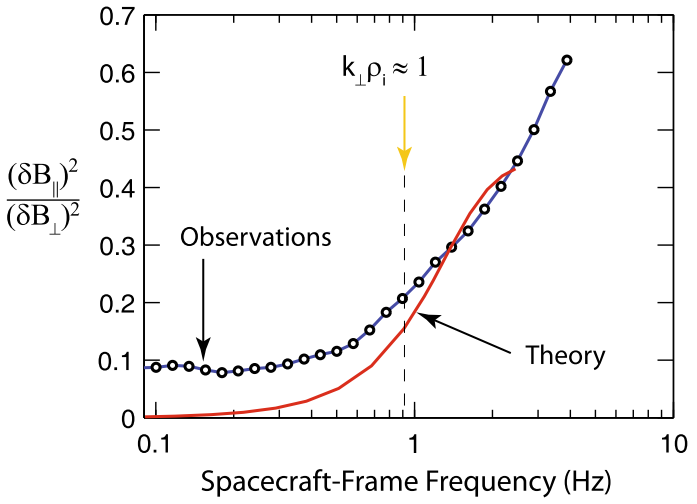

Fig. 5.20 A sample showing comparisons between the theoretical predictions for KAWs (red curve) and solar wind measurements (open circles), including only the quasi-perpendicular data with $84^\circ < \theta_{BV} < 96^\circ$, where θ_{BV} is the angle between the local mean magnetic field $\mathbf{B}_0$ and flow velocity $\mathbf{v}_{sw}$, and the vertical dashed line indicates the wave number $k_\perp \rho_p = k_\perp \rho_i = 1$ (reprinted from Podesta, Sol. Phys., 286, 529–548, 2013, copyright 2013, with permission from Springer)

5.5.4 *Identifications of KAW Magnetic Helicity*

Besides the magnetic compressibility, the magnetic helicity also is used often to distinctly identify the physical nature of the kinetic-scale fluctuations in solar wind turbulence. In the inertial range the normalized magnetic helicity spectrum σ_m is zero, on average, in the solar wind at 1 AU, while in the kinetic scale range has a distinctive peak near $k\lambda_i = 1$. Figure 5.21 shows a typical sample measured by the STEREO-A during an interval of 4 days from February 13 2008, 08:00 UT to February 17 08:00 UT for an unusually long-lived high-speed stream with the mean flow velocity $v_{sw} \simeq 655$ km/s, proton density $n_p \simeq 2.2\,\mathrm{cm}^{-3}$, temperature $T_p \simeq 1.6 \times 10^5$ K, and the plasma $\beta_p \simeq 0.7$. By use of the Taylor hypothesis, $\omega \simeq k v_{sw}$, the wave number $k\lambda_i = 1$ occurs at 0.7 Hz denoted by the vertical arrow in Fig. 5.21, implying the typical scale of the kinetic turbulence.

From Fig. 5.21, the trace spectrum (upper panel) of the magnetic fluctuations can be fitted well by a power-low spectrum with an index of 1.57 in the inertial range over the satellite-frame frequency from 1 to 100 mHz. When approaching the kinetic scales the trace spectrum breaks evidently and becomes steeper in the kinetic scale range, as expected by the kinetic turbulence theory. On the other hand, from Fig. 5.21, it can be found that the normalized magnetic helicity spectrum σ_m (lower panel) exhibits strong fluctuations with an average value near zero in the inertial range. While in the kinetic scale range immediately after the spectral break the magnetic helicity spectrum remarkably departs from zero and has a clear peak near 1 Hz, a typical

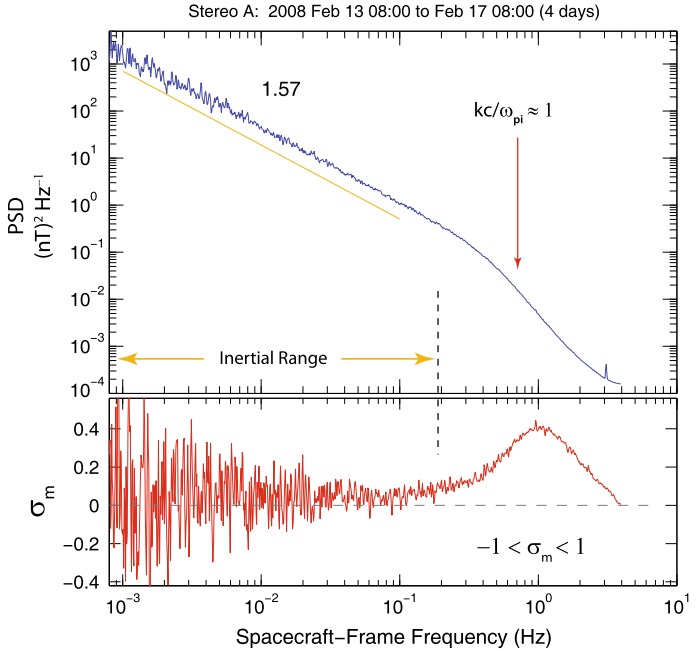

Fig. 5.21 A sample of the trace spectrum (upper panel) and the normalized magnetic helicity spectrum (lower panel) of solar wind magnetic fluctuations near 1 AU, which were measured by the STEREO-A on February 13 2008, 08:00 UT to February 17 08:00 UT (4 days) for an unusually long-lived high-speed stream with the mean parameters $v_{sw} \simeq 655$ km/s, $n_p \simeq 2.2\,\mathrm{cm}^{-3}$, $T_p \simeq 1.6 \times 10^5$ K, and $\beta_p \simeq 0.7$. The spectral slope in the inertial range over the satellite-frame frequency from 1 to 100 mHz is 1.57. By use of the Taylor hypothesis, the wave number $k\lambda_i = 1$ occurs at 0.7 Hz as denoted by the vertical arrow. The normalized magnetic helicity spectrum σ_m exhibits clearly a peak in the kinetic scale range immediately after the spectral break (reprinted from Podesta, Sol. Phys., 286, 529–548, 2013, copyright 2013, with permission from Springer)

kinetic scale. In addition, the fluctuation of the magnetic helicity spectrum also is strongly depressed in the kinetic scale range. Usually this may be explained by waves with a predominantly right-hand sense of polarization propagating away from the Sun (Goldstein et al. 1994; Leamon et al. 1998a). This peak is formed possibly by the ion-cyclotron damping of a cascade of predominantly outward-propagating quasi-parallel Alfvénic ion-cyclotron waves near the spectral breaking point. In consequence, only right-hand polarized quasi-parallel magnetosonic whistler waves cascade through the spectral breaking point into higher wave numbers (Goldstein et al. 1994; Leamon et al. 1998a; Leamon 1998b).

However, the theory and simulation of the plasma turbulence both show that the turbulent energy cascade towards small scales proceeds preferentially in the direction perpendicular to the local mean magnetic field (Goldreich and Sridhar 1995, 1997; Biskamp et al. 1996, 1999; Cho and Vishniac 2000; Maron and Goldreich 2001;

Müller et al. 2003; Cho and Lazarian 2004; Boldyrev 2005, 2006; Howes et al. 2006, 2008a, b; 2011; Schekochihin et al. 2009; Boldyrev and Perez 2012; Boldyrev et al. 2013). This results in that in the kinetic scale range the turbulent energy in quasi-parallel fluctuations would be much less than that in quasi-perpendicular fluctuations, implying that the plasma turbulence in the kinetic scales most likely consists of a cascade of quasi-perpendicular KAWs rather than quasi-parallel whistler waves. Therefore, the ion-cyclotron damping scenario of the formation of the kinetic magnetic helicity spectrum in the kinetic scale range seems unlikely. Howes and Quataert (2010) proposed an alternative interpretation, in which the observed peak in the kinetic magnetic helicity spectrum $\sigma_m(\mathbf{k})$ is caused by quasi-perpendicular KAWs with $k_\perp \gg k_\parallel$. They showed that an anisotropic spectrum of predominantly outward-propagating quasi-perpendicular KAWs, which are also right-hand polarized like the quasi-parallel whistler waves, can produce a magnetic helicity spectrum $\sigma_m(\mathbf{k})$ with a peak in the kinetic scales, which is in reasonable agreement with the observations (Howes and Quataert 2010).

In order to determine further the wave vector direction of the observed magnetic helicity spectrum $\sigma_m(\mathbf{k})$, He et al. (2011, 2012a) and Podesta and Gary (2011) analyzed the look-angle distribution of the observed magnetic helicity spectrum, $\sigma_m(\mathbf{k})$, with respect to the local mean magnetic field. Using the same STEREO-A data as used in Fig. 5.21, two distinct populations of the electromagnetic fluctuations are found at the typical kinetic scales near $k_\perp \rho_i = 1$ as shown in the right panel of Fig. 5.22. One has a left-hand polarization sense with $\sigma_m < 0$ in the satellite frame, denoted by the blue spot near $\theta_{BV} \sim 0$ (i.e., quasi-parallel propagating fluctuations) and the other one has a right-hand polarization sense with $\sigma_m > 0$ in the satellite frame, denoted by the orange and yellow spots located near $\theta_{BV} = 90°$ (i.e., quasi-perpendicular propagating fluctuations). Tentatively, the quasi-parallel fluctuations may be identified as electromagnetic ion-cyclotron waves propagating away from the Sun or magnetosonic whistler waves propagating toward the Sun along the local mean magnetic field, while the quasi-perpendicular waves could be identified as KAWs or oblique whistler waves.

He et al. (2012a) analyzed in detail the hodographs in the local RTN coordinate system (where R points toward the satellite from the Sun center, T is the cross product of the solar rotation axis and R, N completes the right-handed triad) for the fluctuations presented in Fig. 5.22. Figure 5.23 shows two examples of them, which represent the left-hand polarization with $\sigma_m < 0$ (b) and the right-hand polarization with $\sigma_m > 0$ (c). In particular, they found that the major axis of the right-hand polarization ellipses is perpendicular to the local mean magnetic field $\mathbf{B}_0$, implying $\delta B_\perp > \delta B_\parallel$ (He et al. 2012a). This is the typical property of quasi-perpendicular KAWs rather than quasi-perpendicular whistler waves. In fact, for a quasi-perpendicular whistler wave, the major axis of its magnetic polarization ellipse is expected to be aligned with the local $\mathbf{B}_0$, implying significant magnetic compressibility, and the polarization sense turns from right to left handedness as the wave propagation angle (θ_{BV}) increases toward 90°. Therefore, they concluded that, in the kinetic scale range near the break of solar wind turbulence spectra occurring around the proton inertial length (or i.e., the proton gyroradius), the observed right-hand polarization ellipse with orientation

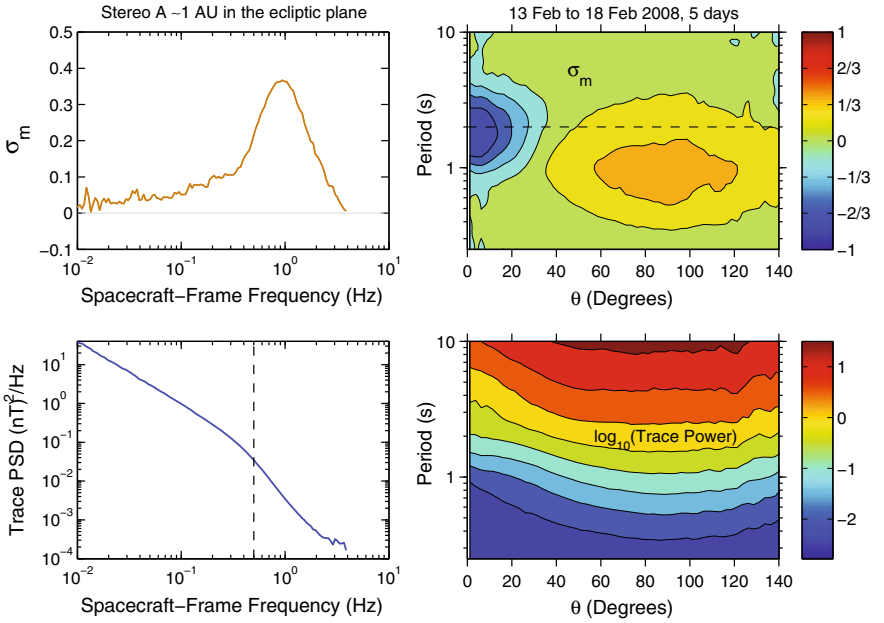

Fig. 5.22 Analysis of a five-day interval of high-speed wind observed in the ecliptic plane near 1 AU by the STEREO-A satellite: Left panel is the magnetic helicity spectrum (upper) and the trace power spectrum (lower) same as that presented in Fig. 5.21 but focus on the kinetic scale range. Right panel shows the look-angle distribution of the magnetic helicity spectrum, where the look angle $\theta = \theta_{BV}$ is the angle between the flow velocity $\mathbf{v}_{sw}$ and the local mean magnetic field $\mathbf{B}_0$ of the solar wind. The vertical (left-lower panel) and horizontal (right-upper panel) dashed lines denote the typical kinetic scale of $k_\perp \rho_i = 1$ (from Podesta and Gary 2011)

perpendicular to the local $\mathbf{B}_0$ represents quasi-perpendicular KAWs (i.e., oblique Alfvénic ion-cyclotron waves) rather than quasi-perpendicular magnetosonic whistler waves, as expected by the theory and simulation of the kinetic turbulence.

In order to further understand the physical nature of the population of the quasi-parallel fluctuations in above the observations (He et al. 2011, 2012a; Podesta and Gary 2011), He et al. (2012b) modeled the measured angular distribution of σ_m by assuming a possible distribution formed by Alfvénic fluctuations in wave vector space and then looked for the best fitting for the observations by adjusting the spectral distributions of the assumed fluctuations. In consequence, a very good agreement between the theoretical model and the observations can be found as shown in Fig. 5.24. Their model shows that the observed two-component angular distribution of the magnetic helicity spectrum ($\sigma_m(k, \theta_{BV})$) can be reproduced well by the superposition of two-component Alfvénic fluctuations, which consists of quasi-perpendicular KAWs as a major component close to $k_\perp$ (i.e., $\theta_{BV} \sim 90°$) and quasi-parallel electromagnetic ion-cyclotron waves as a minor component close to $k_\parallel$ (i.e., $\theta_{BV} \sim 0$).

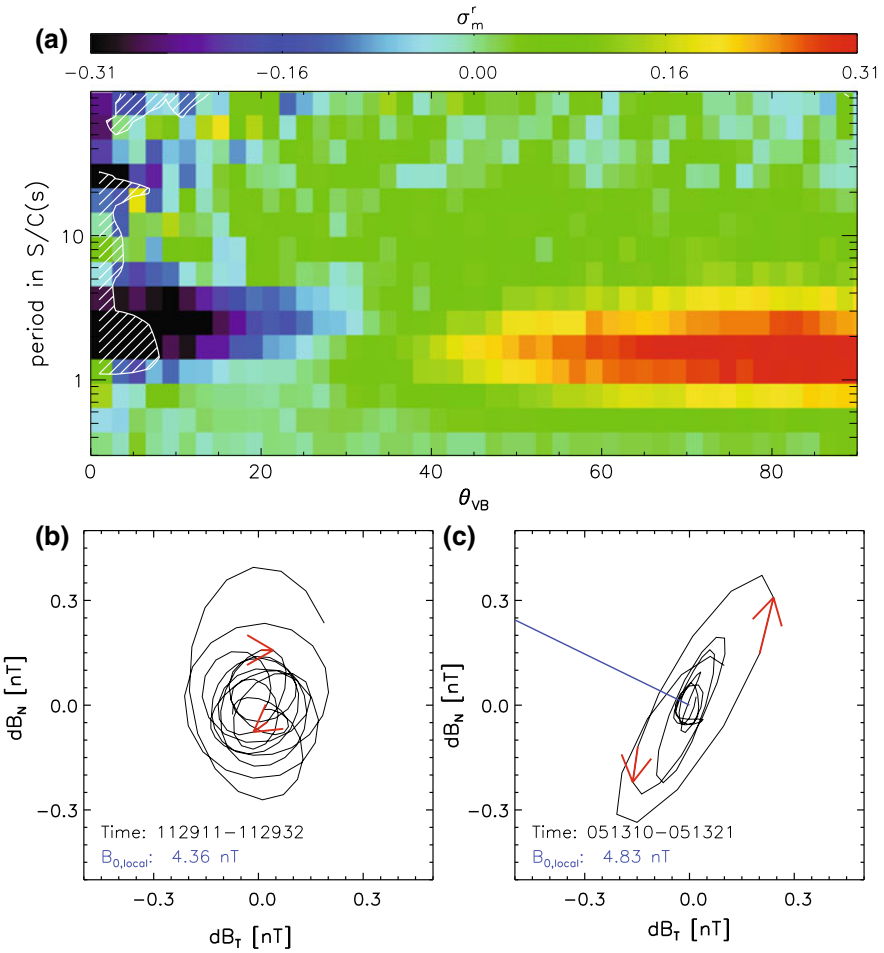

Fig. 5.23 **a** Look-angle (θ_{BV}) distribution of magnetic helicity spectrum (σ_m) derived from the STEREO-A measurements on 13 February 2008 (the same as that in Fig. 5.21, but a shorter interval); **b** An example of the $dB_T - dB_N$ hodograph for negative σ_m in (**a**), which is extracted from a small interval from 11:29:11 to 11:29:32 UT during which the local $\mathbf{B}_0$ is quasi-parallel to the R-direction with $\theta_{BV} < 10°$. Red arrows denote a circle-like left-hand polarization of $dB_T - dB_N$ around the R-direction; **c** One case of the $dB_T - dB_N$ hodograph, which is extracted from an interval from 05:13:10 to 05:13:21 UT when $80° < \theta_{BV} < 90°$. Red arrows denote an ellipse-like right-hand polarization of $dB_T - dB_N$ around the R-direction. Blue line represents the local $\mathbf{B}_0$, which is perpendicular to the major axis of the ellipse, implying $dB_\perp > dB_\parallel$ (from He et al. 2012a, ©AAS reproduced with permission)

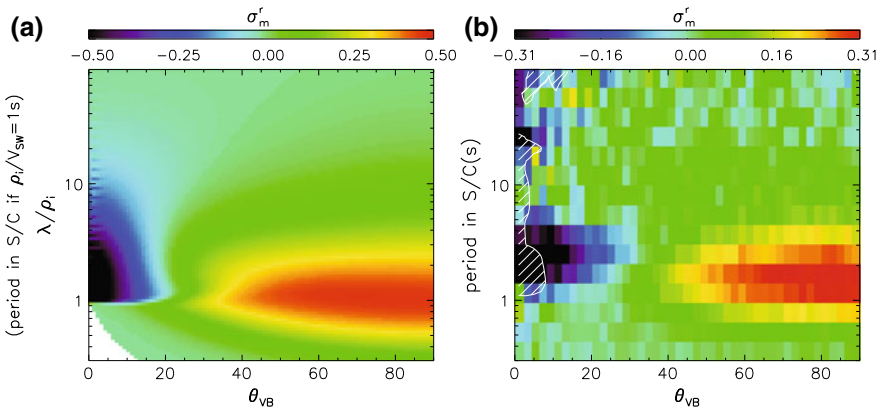

Fig. 5.24 **a** Modeling result of the angular distribution of σ_m based on gradually balanced two-component AWs; **b** Observation of the angular distribution of the two-component σ_m (from He et al. 2012b, ©AAS reproduced with permission)

In an independent but similar modelling study, Klein et al. (2014) obtained similar results. They showed that the observed two-component angular distribution of the magnetic helicity spectrum σ_m can be reproduced by a perpendicular cascade of KAWs and a local parallel non-turbulent ion-cyclotron or whistler waves generated by temperature anisotropy instabilities. By constraining the model free parameters through comparison to in situ data, it is found that, on average, ∼95% of the power near the kinetic scales is contained in a perpendicular KAW cascade and that the parallel non-turbulent waves are propagating nearly unidirectionally.

In addition, they also noticed that in order to reproduce the observed diminishing of the magnetic helicity spectrum σ_m at shorter scales of $k_\perp \rho_i > 1$ the balance between outward and inward wave-energy fluxes needs to be reached gradually as the spatial scale decreases. In the observations, however, the diminishing of σ_m occurs at frequencies close to the Nyquist frequency (i.e., the data sampling frequency, He et al. 2011, 2012a; Podesta and Gary 2011; Klein et al. 2014). Also this possibly could influence the diminishing of σ_m in the short scales.

From these observations and modelling investigations of the magnetic helicity spectra, we can include two definite results, one is that in the kinetic scale range of solar wind turbulence the quasi-perpendicular cascade component dominates the magnetic helicity spectrum and contains ∼95% of the spectral power, and the other is that the physical nature of the quasi-perpendicular cascade component is KAWs. These results both can be well consistent with the predictions of the theories and simulations of the kinetic turbulence (Boldyrev 2005, 2006; Howes et al. 2006, 2008a, b; 2011; Schekochihin et al. 2009; Boldyrev and Perez 2012; Boldyrev et al. 2013; Grošelj et al. 2018).

References

Abel, I. G., Barnes, M., Cowley, S. C., et al. (2008). Linearized model fokker-planck collision operators for gyrokinetic simulations. I. theory. *Physics of Plasmas*, *15*, 122509.

Acuña, M. H., Curtis, D., Scheifele, J. L., et al. (2008). The STEREO/IMPACT magnetic field experiment. *Space Science Reviews*, *136*, 203–226.

Alexandrova, O., Saur, J., Lacombe, C., et al. (2009). Universality of solar-wind turbulent spectrum from MHD to electron scales. *Physical Review Letters*, *103*, 165003.

Bale, S. D., Kellogg, P. J., Mozer, F. S., et al. (2005). Measurement of the electric fluctuation spectrum of magnetohydrodynamic turbulence. *Physical Review Letters*, *94*, 215002.

Barnes, M., Abel, I. G., Dorland, W., et al. (2009). Linearized model fokker-planck collision operators for gyrokinetic simulations. II. numerical implementation and tests. *Physics of Plasmas*, *16*, 128.

Beresnyak, A., & Lazarian, A. (2006). Polarization intermittency and its influence on MHD turbulence. *The Astrophysical Journal*, *640*, L175–L178.

Biskamp, D. (2003). *Magnetohydrodynamic turbulence*. Cambridge: Cambridge University Press.

Biskamp, D., & Müller, W. C. (2000). Scaling properties of three-dimensional isotropic magnetohydrodynamic turbulence. *Physical Review Letters*, *7*, 4889–4900.

Biskamp, D., Schwarz, E., & Drake, J. F. (1996). Two-dimensional electron magnetohydrodynamic turbulence. *Physical Review Letters*, *76*, 1264–1267.

Biskamp, D., Schwarz, E., Zeiler, A., et al. (1999). Electron magnetohydrodynamic turbulence. *Physics of Plasmas*, *6*, 751–758.

Boldyrev, S. (2005). On the spectrum of magnetohydrodynamic turbulence. *The Astrophysical Journal*, *626*, L37.

Boldyrev, S. (2006). Spectrum of magnetohydrodynamic turbulence. *Physical Review Letters*, *96*, 115002.

Boldyrev, S., & Perez, J. C. (2012). Spectrum of kinetic-Alfvén turbulence. *The Astrophysical Journal Letters*, *758*, L44.

Boldyrev, S., Horaites, K., Xia, Q., & Perez, J. C. (2013). Toward a theory of astrophysical plasma turbulence at subproton scales. *The Astrophysical Journal*, *777*, 41.

Bruno, R., & Carbone, V. (2005). The solar wind as a turbulence laboratory. *Living Reviews in Solar Physics*, *2*, 4.

Bruno, R., & Carbone, V. (2013). The solar wind as a turbulence laboratory. *Living Reviews in Solar Physics*, *10*, 2.

Cerri, S. S., Servidio, S., & Califano, F. (2017). Kinetic cascade in solar-wind turbulence: 3D3V hybrid-kinetic simulations with electron inertia. *The Astrophysical Journal Letters*, *846*, L18.

Chandran, B. D. G., Schekochihin, A. A., & Mallet, A. (2015). Intermittency and alignment in strong RMHD turbulence. *The Astrophysical Journal*, *807*, 39.

Chen, C. H. K., Boldyrev, S., Xia, Q., & Perez, J. C. (2013). Nature of subproton scale turbulence in the solar wind. *Physical Review Letters*, *110*, 225002.

Chen, C. H. K., Horbury, T. S., Schekochihin, A. A., et al. (2010). Anisotropy of solar wind turbulence between ion and electron scales. *Physical Review Letters*, *104*, 255002.

Chen, L., & Wu, D. J. (2011a). Exact solutions of dispersion equation for MHD waves with short-wavelength modification. *Chinese Science Bulletin*, *56*, 955–961.

Chen, L., & Wu, D. J. (2011b). Polarizations of coupling kinetic Alfvén and slow waves. *Physics of Plasmas*, *18*, 072110.

Chen, L., & Zonca, F. (2016). Physics of Alfvén waves and energetic particles in burning plasmas. *Reviews of Modern Physics*, *88*, 015008.

Cho, J., & Lazarian, A. (2004). The anisotropy of electron magnetohydrodynamic turbulence. *The Astrophysical Journal*, *615*, L41–L44.

Cho, J., & Vishniac, E. T. (2000). The anisotropy of MHD Alfvénic turbulence. *The Astrophysical Journal*, *539*, 273–282.

Coleman, P. J, Jr. (1968). Turbulence, viscosity, and dissipation in the solar-wind plasma. *The Astrophysical Journal*, *153*, 371–388.

Dobrowolny, M., Mangeney, A., & Veltri, P. (1980). Properties of magnetohydrodynamic turbulence in the solar wind. *Astronomy & Astrophysics*, *83*, 26–32.

Fonseca, R. A., Martins, S. F., Silva, L. O., et al. (2008). One-to-one direct modeling of experiments and astrophysical scenario: Pushing the envelope on kinetic plasma simulations. *Plasma Physics and Controlled Fusion*, *50*, 124034.

Fonseca, R. A., Silva, L. O., Tsung, F. S., et al. (2002). OSIRIS: A Three-Dimensional, fully relativistic particle in cell code for modeling plasma based accelerators. *Lecture Notes in Computer Science*, *2331*, 342–351.

Forman, M. A., Wicks, R. T., & Horbury, T. S. (2011). Detailed fit of critical balance theory to solar wind turbulence measurements. *The Astrophysical Journal*, *733*, 76.

Frieman, E. A., & Chen, L. (1982). Nonlinear gyrokinetic equations for low-frequency electromagnetic waves in general plasma equilibria. *Physics of Fluids*, *25*, 502.

Frisch, U. (1995). *Turbulence: The legacy of A. N. Kolmogorov*. Cambridge: Cambridge University Press.

Gary, S. P., & Smith, C. W. (2009). Short-wavelength turbulence in the solar wind: Linear theory of whistler and kinetic Alfvén fluctuations. *Journal of Geophysical Research*, *114*, A12105.

Goldreich, P., & Sridhar, S. (1995). Toward a theory of interstellar turbulence. 2: Strong Alfvénic turbulence. *The Astrophysical Journal*, *438*, 763–775.

Goldreich, P., & Sridhar, S. (1997). Magnetohydrodynamic turbulence revisited. *The Astrophysical Journal*, *485*, 680–688.

Goldstein, M. L., Roberts, D. A., & Fitch, C. A. (1994). Properties of the fluctuating magnetic helicity in the inertial and dissipation ranges of solar wind turbulence. *Journal of Geophysical Research*, *99*, 11519–11538.

Goldstein, M. L., Wicks, R. T., Perri, S., & Sahraoui, F. (2015). Kinetic scale turbulence and dissipation in the solar wind: Key observational results and future outlook. *Philosophical Transactions of the Royal Society A*, *373*, 20140147.

Gollub, J. P., & Swinney, H. L. (1975). Onset of turbulence in a rotating fluid. *Physical Review Letters*, *35*, 927–930.

Grappin, R., Frisch, U., Pouquet, A., & Leorat, J. (1982). Alfvénic fluctuations as asymptotic states of MHD turbulence. *Astronomy & Astrophysics*, *105*, 6–14.

Grošelj, D., Mallet, A., Loureiro, N. F., & Jenko, F. (2018). Fully kinetic simulation of 3D kinetic Klfvén turbulence. *Physical Review Letters*, *120*, 105101.

Hamilton, K., Smith, C. W., Vasquez, B. J., & Leamon, R. J. (2008). Anisotropies and helicities in the solar wind inertial and dissipation ranges at 1 AU. *Journal of Geophysical Research*, *113*, A01106.

He, J., Marsch, E., Tu, C., et al. (2011). Possible evidence of Alfvén-cyclotron waves in the angle distribution of magnetic helicity of solar wind turbulence. *The Astrophysical Journal*, *731*, 85.

He, J., Tu, C., Marsch, E., & Yao, S. (2012a). Do oblique Alfvén/ion-cyclotron or fast-mode/whistler waves dominant the dissipation of solar wind turbulence near the proton inertial length? *The Astrophysical Journal Letters*, *745*, L8.

He, J., Tu, C., Marsch, E., & Yao, S. (2012b). Reproduction of the observed two-component magnetic helicity in solar wind turbulence by a superposition of parallel and oblique Alfvén waves. *The Astrophysical Journal*, *749*, 86.

Hollweg, J. V. (1999). Kinetic Alfvén wave revisited. *Journal of Geophysical Research*, *104*, 14811–14820.

Hopf, E. (1948). A mathematical example displaying features of turbulence. *Communications on Pure and Applied Mathematics*, *1*, 303–322.

Horbury, T. S., Forman, M., & Oughton, S. (2008). Anisotropic scaling of magnetohydrodynamic turbulence. *Physical Review Letters*, *101*, 175005.

Howes, G. G., & Quataert, E. (2010). On the interpretation of magnetic helicity signatures in the dissipation range of solar wind turbulence. *The Astrophysical Journal Letters*, *709*, L49–L52.

Howes, G. G., Cowley, S. C., Dorland, W., et al. (2006). Astrophysical gyrokinetics: Basic equations and linear theory. *The Astrophysical Journal*, *651*, 590–614.

Howes, G. G., Cowley, S. C., Dorland, W., et al. (2008b). A model of turbulence in magnetized plasmas: Implications for the dissipation range in the solar wind. *Journal of Geophysical Research*, *113*, A05103.

Howes, G. G., Dorland, W., Cowley, S. C., et al. (2008a). Kinetic simulations of magnetized turbulence in astrophysical plasmas. *Physical Review Letters*, *100*, 065004.

Howes, G. G., Tenbarge, J. M., Dorland, W., et al. (2011). Gyrokinetic simulations of solar wind turbulence from ion to electron scales. *Physical Review Letters*, *107*, 035004.

Howes, G., Dorland, W., Schekochihin, A., et al. (2010). A weakened cascade model for solar wind turbulence. In *52nd Annual Meeting of the APS Division of Plasma Physics*, 8–12 Nov, APS.

Iroshnikov, R. S. (1963), The turbulence of a conducting fluid in a strong magnetic field, *Astron. Zh. 40*, 742–750. (English Translation: Sov. Astron. 1964, 7, 566).

Kingsep, A. S., Chukbar, K. V., & Yan'kov, V. V. (1990). Electron magnetohydrodynamics. In B. B. Kadomtsev (Ed.), *Reviews of plasma physics* (pp. 243–291). NY: Consultants Bureau.

Kiyani, K. H., Chapman, S. C., Khotyaintsev, Yu V., et al. (2009). Global scale-invariant dissipation in collisionless plasma turbulence. *Physical Review Letters*, *103*, 075006.

Klein, K. G., Howes, G. G., TenBarge, J. M., & Podesta, J. J. (2014). Physical interpretation of the angle-dependent magnetic helicity spectrum in the solar wind: The nature of turbulent fluctuations near the proton gyroradius scale. *The Astrophysical Journal*, *785*, 138.

Kolmogorov, A. N. (1941). The local structure turbulence in incompressible viscous fluids for very large Reynolds numbers, Dokl. Akad. Nauk. SSSR 30, 301–305. Reprinted in 1991. *Proceedings of the Royal Society of London Series A*, *434*, 9–13.

Kraichnan, R. H. (1965). Inertial range spectrum of hyromagnetic turbulence. *Physics of Fluids*, *8*, 1385–1387.

López, R. A., Viñas, A. F., Araneda, J. A., & Yoon, P. H. (2017). Kinetic scale structure of low-frequency waves and fluctuations. *The Astrophysical Journal*, *845*, 60.

Landau, L. (1944). Stability of tangential discontinuities in compressible fluid. In *Proceedings of the USSR Academy of Sciences* (Vol. 44, pp. 139–141).

Leamon, R. J., Matthaeus, W. H., Smith, C. W., & Wong, H. K. (1998b). Contribution of cyclotron-resonant damping to kinetic dissipation of interplanetary turbulence. *The Astrophysical Journal*, *507*, L181–L184.

Leamon, R. J., Smith, C. W., Ness, N. F., et al. (1998a). Observational constraints on the dynamics of the interplanetary magnetic field dissipation range. *Journal of Geophysical Research*, *103*, 4775–4787.

Lumley, J. L., & Yaglom, A. M. (2001). A century of turbulence. *Flow, Turbulence and Combustion*, *66*, 241–286.

Luo, Q. Y., & Wu, D. J. (2010). Observations of anisotropic scaling of solar wind turbulence. *The Astrophysical Journal Letters*, *714*, L138–L141.

Luo, Q. Y., Wu, D. J., & Yang, L. (2011). Measurement of intermittency of anisotropic magnetohydrodynamic turbulence in high-speed solar wind. *The Astrophysical Journal Letters*, *733*, L22.

Müller, W. C., Biskamp, D., & Grappin, R. (2003). Statistical anisotropy of magnetohydrodynamic turbulence. *Physical Review E*, *67*, 066302.

Maron, J., & Goldreich, P. (2001). Simulations of incompressible magnetohydrodynamic turbulence. *The Astrophysical Journal*, *554*, 1175–1196.

Mason, J., Cattaneo, F., & Boldyrev, S. (2006). Dynamic alignment in driven magnetohydrodynamic turbulence. *Physical Review Letters*, *97*, 255002.

Matthaeus, W. H., Wan, M., Servidio, S., et al. (2015). Intermittency, nonlinear dynamics and dissipation in the solar wind and astrophysical plasmas. *Philosophical Transactions of the Royal Society A*, *373*, 20140154.

Mithaiwala, M., Rudakov, L., Crabtree, C., & Ganguli, G. (2012). Co-existence of whistler waves with kinetic Alfvén wave turbulence for the high-beta solar wind plasma. *Physics of Plasmas*, *19*, 102902.

Ng, C. S., & Bhattacharjee, A. (1996). Interaction of shear-Alfvén wave packets: Implication for weak magnetohydrodynamic turbulence in astrophysical plasmas. *The Astrophysical Journal*, *465*, 845.

Numata, R., Howes, G. G., Tatsuno, T., et al. (2010). AstroGK: Astrophysical gyrokinetics code. *Journal of Computational Physics*, *229*, 9347–9372.

Parker, E. N. (1979). *Cosmical magnetic fields: Their origin and their activity*. New York: Oxford University Press.

Pincon, J. L. (1995). Cluster and the K-filtering. In K.-H. Glassmeier, U. Motschmann, & R. Schmidt (Eds.), *Proceedings of the Cluster Workshops, Data Analysis Tools and Physical Measurements and Mission-Oriented Theory* (p. 87). European Space Agency.

Podesta, J. J. (2009). Dependence of solar-wind power spectra on the direction of the local mean magnetic field. *The Astrophysical Journal*, *698*, 986–999.

Podesta, J. J. (2013). Evidence of kinetic Alfvén waves in the solar wind at 1 AU. *Solar Physics*, *286*, 529–548.

Podesta, J. J., & Gary, S. P. (2011). Magnetic helicity spectrum of solar wind fluctuations as a function of the angle with respect to the local mean magnetic field. *The Astrophysical Journal*, *734*, 15.

Podesta, J. J., & TenBarge, J. M. (2012). Scale dependence of the variance anisotropy near the proton gyroradius scale: Additional evidence for kinetic Alfvén waves in the solar wind at 1 AU. *Journal of Geophysical Research*, *117*, A10106.

Podesta, J. J., Borovsky, J. E., & Gary, S. P. (2010). A kinetic Alfvén wave cascade subject to collisionless damping cannot reach electron scales in the solar wind at 1 AU. *The Astrophysical Journal*, *712*, 685–691.

Pouquet, A., Meneguzzi, M., & Frisch, U. (1986). Growth of correlations in magnetohydrodynamic turbulence. *Physical Review A*, *33*, 4266–4276.

Reynolds, O. (1883). An experimental investigation of the circumstances which determine whether the motion of water shall he direct or sinuous, and of the law of resistance in parallel channels. *Proceedings of the Royal Society*, *35*, 84–99.

Ruelle, D., & Takens, F. (1971). On the nature of turbulence. *Communications in Mathematical Physics*, *23*, 343–344.

Rutherford, P. H., & Frieman, E. A. (1968). Drift instabilities in general magnetic field configurations. *Physics of Fluids*, *11*, 569.

Sahraoui, F., Goldstein, M. L., Belmont, G., et al. (2010). Three dimensional anisotropic k spectra of turbulence at subproton scales in the solar wind. *Physical Review Letters*, *105*, 131101.

Sahraoui, F., Goldstein, M. L., Robert, P., & Khotyaintsev, Yu V. (2009). Evidence of a cascade and dissipation of solar-wind turbulence at the electron gyroscale. *Physical Review Letters*, *102*, 231102.

Salem, C. S., Howes, G. G., Sundkvist, D., et al. (2012). Identification of kinetic Alfvén wave turbulence in the solar wind. *The Astrophysical Journal Letters*, *745*, L9.

Schekochihin, A. A., Cowley, S. C., Dorland, W., et al. (2009). Astrophysical gyrokinetics: Kinetic and fluid turbulent cascades in magnetized weakly collisional plasmas. *The Astrophysical Journal Supplement Series*, *182*, 310–377.

Smale, S. (1967). Differentiable dynamical systems. *Bulletin of the American Mathematical Society*, *73*, 747–817.

Sridhar, S., & Goldreich, P. (1994). Toward a theory of interstellar turbulence 1: Weak Alfvénic turbulence. *The Astrophysical Journal*, *432*, 612–621.

Tatsuno, T., Dorland, W., Schekochihin, A. A., et al. (2009). Nonlinear phase mixing and phase-space cascade of entropy in gyrokinetic plasma turbulence. *Physical Review Letters*, *103*, 015003.

Taylor, G. I. (1938). Production and dissipation of vorticity in a turbulent fluid. *Proceedings of the Royal Society of London Series A*, *164*, 15–23.

TenBarge, J. M., & Howes, G. G. (2012). Evidence of critical balance in kinetic Alfvén wave turbulence simulations. *Physics of Plasmas*, *19*, 419–763.

TenBarge, J. M., Howes, G. G., & Dorland, W. (2013). Collisionless damping at electron scales in solar wind turbulence. *The Astrophysical Journal*, *774*, 1201–1205.

TenBarge, J. M., Podesta, J. J., Klein, K. G., & Howes, G. G. (2012). Interpreting magnetic variance anisotropy measurements in the solar wind. *The Astrophysical Journal*, *753*, 107.

Told, D., Jenko, F., TenBarge, J. M., et al. (2015). Multiscale nature of the dissipation range in gyrokinetic simulations of Alfvénic turbulence. *Physical Review Letters*, *115*, 025003.

Torrence, C., & Compo, G. P. (1998). A practical guide to wavelet analysis. *Bulletin of the American Meteorological Society*, *79*, 61–78.

Tu, C. Y., & Marsch, E. (1995). MHD structures, waves and turbulence in the solar wind: Observations and theories. *Space Science Reviews*, *73*, 1–210.

Voitenko, Yu M, & Keyser, J. D. (2011). Turbulent spectra and spectral kinks in the transition range from MHD to kinetic Alfvén turbulence. *Nonlinear Processes in Geophysics*, *18*, 587–597.

Voitenko, Yu M. (1998a). Three-wave coupling and parametric decay of kinetic Alfvén waves. *Journal of Plasma Physics*, *60*, 497–514.

Voitenko, Yu M. (1998b). Three-wave coupling and weak turbulence of kinetic Alfvén waves. *Journal of Plasma Physics*, *60*, 515–527.

Wicks, R. T., Horbury, T. S., Chen, C. H. K., & Schekochihin, A. A. (2010). Power and spectral index anisotropy of the entire inertial range of turbulence in the fast solar wind. *Monthly Notices of the Royal Astronomical Society*, *407*, L31–L35.

Zhao, J. S., Voitenko, Y. M., Wu, D. J., & Yu, M. Y. (2016). Kinetic Alfvén turbulence below and above ion cyclotron frequency. *Journal of Geophysical Research*, *121*, 5–18.

Zhao, J. S., Wu, D. J., & Lu, J. Y. (2013). Kinetic Alfvén turbulence and parallel electric fields in flare loops. *The Astrophysical Journal*, *767*, 109.